CARBONATE CAPROCK SEALING CAPABILITIES:

CCUS APPLICATIONS IN THE MICHIGAN BASIN

By

MARY K TKACH

Bachelor of Science in Geology

University of Pittsburgh

Pittsburgh, Pennsylvania

2016

Submitted to the Faculty of the
Graduate College of the
Oklahoma State University
in partial fulfillment of
the requirements for
the Degree of
MASTER OF SCIENCE
December, 2020

CARBONATE CAPROCK SEALING CAPABILITIES:

CCUS APPLICATIONS IN THE MICHIGAN BASIN

Thesis Approved:

Dr James H Knapp

Thesis Adviser

Mr. Sean Sanguinito, MS

Dr G Michael Grammer

ACKNOWLEDGEMENTS

I am forever grateful for the opportunity to grow as a geologist at the Boone Pickens School of Geology. My time spent in the NRC is considered some of my most cherished moments in my life thus far. Thank you to all my friends, students, and professors for making Geology so great.

I would like to acknowledge and thank my adviser, Jim Knapp, for the caring support and giving me the ability to pursue my research.

I would also like to thank Sean Sanguinito for all his dedicated help, support, and mentorship throughout the project. In addition, thank you Barbara Kutchko and Angela Goodman for all the guidance and instilling my love of research.

I dedicate my thesis to my loving parents who have always supported me in all my pursuits.

Name: MARY K TKACH

Date of Degree: DECEMBER, 2020

Title of Study: CARBONATE CAPROCK SEALING CAPABILITIES: CCUS APPLICATIONS IN THE MICHIGAN BASIN

Major Field: GEOLOGY

Abstract: Identifying the viability of rock formations to successfully limit the upward migration of carbon dioxide (CO_2) is vital for carbon storage permanence. As an attempt to address increasing atmospheric concentrations of CO_2, CO_2 is captured in industrial settings, compressed to a supercritical state (at least 31 °C, 88 °F and 7.38 MPa, 1070 psi), and is eventually injected deep beneath the surface between 0.8 to 1.0 kilometers (2,625 to 3,280 feet), often in saline reservoirs where CO_2 will remain in a dense and stable plume. However, carbon dioxide is a buoyant fluid and will migrate upward through the subsurface until it reaches an impermeable seal which the CO_2 may react with. Typical seals in geologic reservoirs are shales due to their low porosities and permeabilities, however limestones can exhibit similar measurements. This work examines the effect supercritical CO_2 has on potential sealing rock layers within the Michigan Basin, namely the early Devonian Amherstberg limestone formation, which may be largely responsible for sealing sequestered carbon dioxide within underlying rock units. In this study, core samples retrieved from an experimental injection well located in Otsego County, Michigan were exposed to supercritical CO_2 and synthetic formation brine at reservoir pressure and temperature conditions. Scanning Electron Microscopy (SEM) analyses were performed on core samples exposed to dry CO_2 and CO_2-saturated brine to compare surface alterations before and after fluid-rock reactions. X-ray diffraction (XRD) and Energy Dispersive X-ray Spectroscopy (EDS) aided SEM analyses to characterize geochemical changes within the rock sample. Fresh and reacted synthetic brine samples were analyzed using ICP-OES to determine changes in elemental concentration. Findings indicate that calcium carbonate phases are more sensitive to CO_2-saturated brine interactions rather than CO_2 interactions alone, and surface mesoporosity visibly enlarged in regions where such phases reside. In addition, salt and calcium carbonate minerals precipitated out of solution during reactions onto etched rock surfaces resulting in regions of decreased porosity. These findings suggest that CO_2-brine interactions with the Amherstberg Limestone may not reach geochemical equilibrium, shedding light on the potential instability of CO_2 storage within carbonate caprock reservoir systems.

TABLE OF CONTENTS

Chapter Page

LIST OF TABLES

Table Page

LIST OF FIGURES

Figure Page

CHAPTER I

INTRODUCTION

The Midwest Region Carbon Sequestration Partnership (MRCSP) is an amalgamated team comprised of universities, state geological surveys, nongovernmental organizations and private companies formed in 2003. Since its formation 10 states have joined the partnership; Delaware, Indiana, Kentucky, Maryland, Michigan, New Jersey, New York, Ohio, Pennsylvania, and West Virginia. The partnership focus is based on assessing the technical storage potential, economic viability, and public acceptability of carbon storage in the region. The Midwest region contains 82.7 million people (26% U.S population) and a gross regional product of $4.62 trillion (27% of the U.S. economy). Additionally, the region is responsible for 24% of all electricity generated in the United States where over half of the electricity in the region is generated by coal (MRCSP, 2015). The Midwest Region is estimated to contain over 1,300 CO_2 stationary sources, emitting 604 million metric tons of carbon dioxide per year (US Department of Energy and NETL, 2015). Carbon dioxide, produced by the production and combustion of fossil fuels, is the largest contributor to the anthropogenic emissions of greenhouse gases since the industrial revolution (Raupach et al., 2007). Scientists (Raupach et al., 2007; Fang et

al., 2010; Davis et al., 2011; Matter et al., 2011) agree that CO_2 emissions are likely to increase due to population and industrial growth despite increases in energy efficiency. Global efforts have been taken to mitigate CO_2-based climate change effects quickly and directly through the process of Carbon Capture and Storage (CCS) (U.S. Geological Survey, 2013).

The U.S. Department of Energy – National Energy Technology Laboratory (DOE-NETL) defines CCS as the separation and capture of CO_2 from the emissions of industrial processes prior to release into the atmosphere and storage of the CO_2 in deep underground geologic formations (US Department of Energy and NETL, 2015). The CCS process is intended to enable industry to continue to operate while emitting smaller amounts of greenhouse gases in the atmosphere. Because little is known about the large scale reaction of subsurface reservoirs with stored CO_2, the Department of Energy supports the research and development carried out by regional carbon storage partnerships such as the MRCSP to develop technologies to advance the safe, cost-effective, capture and permanent geologic storage and/or use of CO_2 (US Department of Energy and NETL, 2015).

Since 2003, the MRCSP program has implemented three separate, and incremental phases. Phase I developed a clear picture of CO_2 sources and storage potential within the region. Based on the findings of Phase I, the Phase II efforts of the MRCSP involves storing CO_2 as part of geologic field tests across the Midwest Region. One field test set the State Charlton well #4-30 in the Michigan Basin, Otsego County, Michigan, as the target well for experimental injection of CO_2 into the Bass Island Dolomite (Barnes et al., 2009) (Figure 1). Significant carbon sequestration potential is

recognized within the Bass Islands formation and is estimated to store 6.7 billion metric tons of carbon dioxide within the study area (Barnes et al., 2009). Overall, the Michigan Basin is estimated to be able to store nearly 60 billion metric tons of carbon dioxide (USGS, 2013). Phase III aims to inject over 1 million metric tons of CO_2 over the 5-year

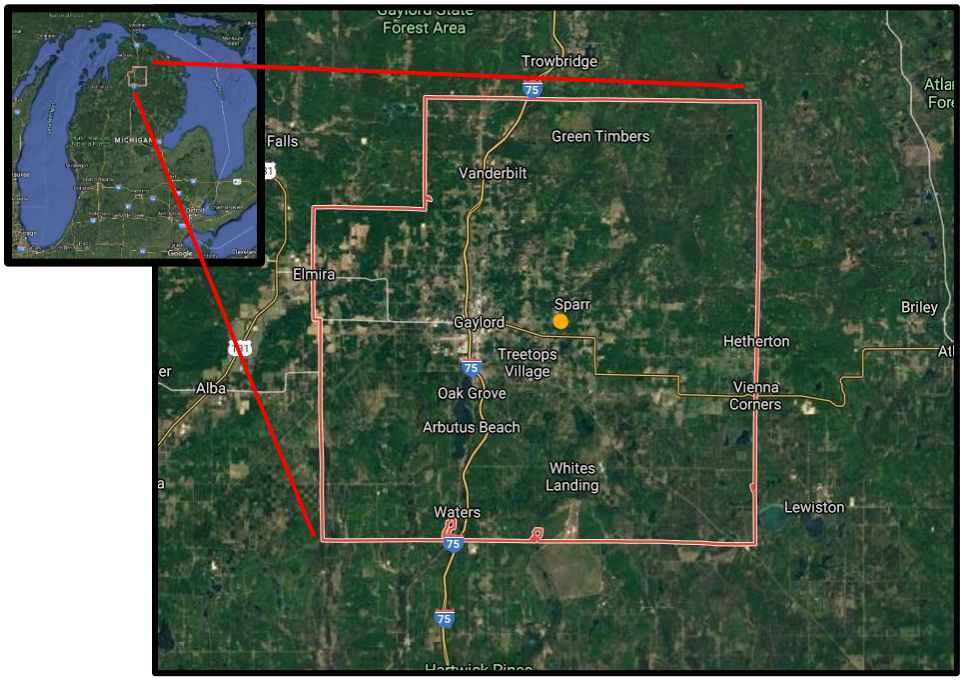

Figure 1) A map of the study area with a red line indicating Otsego Co, Michigan. The yellow dot indicates the approximate location of State Charlton well #4-30.

duration of a large-scale project to demonstrate the potential for commercial-scale geologic carbon storage (MRCSP, 2015).

The process of CO_2 storage involves the separation of CO_2 from industrial emission sources and transporting it to a storage location, usually via pipeline. Once the CO_2 is transported to the storage site, it is injected into deep subsurface reservoirs, these are often abandoned hydrocarbon reservoirs or within saline aquifers. To successfully sequester and maintain carbon dioxide in its supercritical state, potential storage reservoirs should be at sufficient depths at or below 0.8 to 1.0 km (2624.67 to 3280.84 ft)

with temperatures at or above 31°C (87.8 °F), and pressures above 7.38 MPa (1070.38 psi) (Bachu, 2000) (Figure 2). Reservoirs at proper depths also require adequate storage capacity, impermeable top seals, and proper reservoir properties to contain injected fluids (Xu et al., 2009). Top seals are typically assured in prior hydrocarbon reservoirs because they served as seals over geologic time, however saline aquifers do not guarantee that same assurance. Carbon dioxide tends to migrate upward once injected because it is less

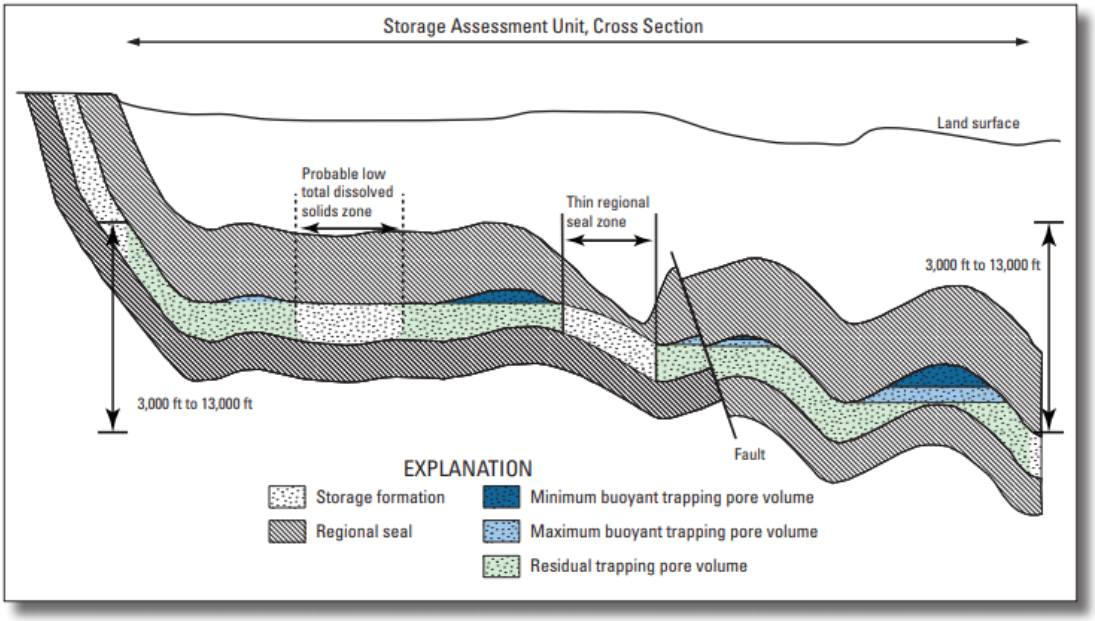

Figure 2) An idealized cross section of a saline aquifer used to store CO_2, modified from USGS 2013

dense than the surrounding formation fluids, but the CO_2 plume may migrate laterally when a seal is encountered (Bowen et al., 2011).

Previous studies identified Michigan Basin strata existing at and below the required depth with appropriate thicknesses, low permeability, and proper effective porosity to potentially store commercial amounts of sequestered carbon dioxide (Harrison et al., 2009). Proper reservoir porosity, averaging 13% in the Bass Islands formation,

from retrieved well core in the Core Energy State Charlton #4-30 well, Otsego County, Michigan, indicates a potential reservoir to sequester commercial amounts of carbon dioxide. Overlying Amherstberg limestone from the test well has low porosity (2-5%) and permeability (approximately 0 mD) (Sminchak et al., 2009). The widespread nature of the Amherstberg coupled with its mechanical properties encourage investigations into its caprock capabilities.

There are four main long-term CO_2 storage processes which include (1) structural trapping, (2) residual trapping, (3) dissolution trapping, and (4) mineral trapping. Structural trapping is the main process during the injection period, and vertical permeability of the reservoir system is important to this stage to control the newly injected plume of CO_2 (Xu et al., 2009). Residual trapping occurs when capillary pressure entraps CO_2 within the pore throats and is often successful when net effective pressure is high (~6,500 psi, 44.8 MPa) (Saeedi et al., 2012). Dissolution trapping refers to the entrapment of carbon dioxide in the aqueous phase when dissolving within reservoir fluids such as saline aquifer brines and solutions (Johnson et al., 2001). Mineral trapping is important to long-term sites where carbonate precipitation is present because CO_2 will dissolve in formation fluids forming weak carbonic acids and consume CO_2 irreversibly by mineralizing within the rock for perpetuity (Gaus et al., 2008). Equations 1-5 outline a likely mineral precipitation reaction occurring within the brine-rock interface to produce a carbonate-like species (Goodman et al., 2019).

$$CO_{2\,(g)} \leftrightarrow CO_{2\,(aq)} \quad (1)$$

$$CO_{2\,(aq)} + H_2O_{(aq)} \leftrightarrow H_2CO_{3\,(aq)} \quad (2)$$

$$H_2CO_{3\,(aq)} \leftrightarrow HCO^-_{3\,(aq)} + H^+_{(aq)} \quad (3)$$

$$HCO^-_{3\,(aq)} \leftrightarrow CO^{2-}_{3\,(aq)} + H^+_{(aq)} \quad (4)$$

$$HCO^-_{3\,(aq)} + Ca^{2+}_{(aq)} \leftrightarrow CaCO_{3\,(s)} + H^+_{(aq)} \quad (5)$$

The interaction of brine and injected CO_2 will cause the pH of the brine to decrease, becoming corrosive to the surrounding materials. This may induce geochemical reactions within the reservoir system such as increasing iron concentrations from leaching ions from reservoir clays. Additionally, carbonate minerals may precipitate from dissociated carbonic acid ions (Gaus et al., 2008). Permeability is likely to increase in carbonate rich CO_2 reservoirs because CO_2 induced precipitation reactions occur within cap rock fractures, however, the precipitation of calcium carbonate minerals within cracks and fractures may decrease permeability. (Gaus et al., 2008). The major geochemical precipitation reaction occurring within the saline aquifer mineral trapping scenario is usually the formation of Dawsonite ($NaAlCO_3$), receiving its aluminum ions from clays, and sodium ions from formation brines. Chemical equilibrium may never be reached within injected CO_2 storage reservoirs during the whole storage period over the course of hundreds to thousands of years.

The goal of this thesis experimental evaluation of the Michigan Basin late Silurian/middle Devonian strata is to gain insight into geochemical interactions between the Amherstberg formation, *in situ* formation brines, and supercritical CO_2 in order to make inferences about the cap rock's ability to act as a geologic carbon dioxide storage (GCS) reservoir seal. Geological and petrophysical characterization, CO_2-formation fluid-cap rock reactions, and geochemical analyses will determine the ability of the cap rock to effectively seal CO_2. The objectives of the study are:

1) Provide a literature review of previous CCS investigations to understand Michigan Basin strata and global geochemical storage reservoir behaviors.
2) Characterize potential cap rocks to understand mineralogical and petrological properties by studying CO_2-formation fluid-cap rock reactions.
3) Identify the geochemical alterations taking place at the fluid-rock interface.

CHAPTER II

REVIEW OF LITERATURE

GEOLOGY

The Michigan Basin is an intracratonic sag basin focused within the lower peninsula of Michigan extending more than 200,000 km^2 (~125,000 mi^2) containing more than 4800 m (16,000 ft) of strata ranging from Precambrian to Pennsylvanian aged rocks (Barnes et al., 2009). The bowl-shaped basin has a slight ovate geometry trending NNW with concentric beds producing a bullseye pattern at the surface beneath approximately 60-90 m (200-300 ft) of Pleistocene glacial drift sediments (Pirtle, 2003). Sedimentary units gently dip and thicken towards the center of the basin. Sediments in the Michigan Basin range from Cambrian to Pennsylvanian, with Jurassic aged units near the center of the basin (Stanford, 1967). Early estimates indicate nearly half of the strata in the Michigan Basin are thought to be carbonate, while a quarter of the sediments are sublitharenites (Figure 3). The remaining portion is represented by almost equal amounts of shale and evaporites, including salt and anhydrite (Gardner, 1974). The present-day location of the Michigan Basin (Figure 4) encountered early onset rifting, post-depositional rifting, sea level transgressions and regressions; all contributing to the basin's structural geometry (Howell et al., 1990) . Its present structure formed during the Ordovician due to

transgression of an inland sea and resultant sediment influx causing sediment loading and downward compressional forces (Sloss, 1982). Maximum subsidence formed during the Silurian and Devonian due to the uplifting of arches surrounding the Michigan Basin. Landes notes that deposition during Lucas time within the Devonian is where most sagging occurred. As a result of 500 m to 1000 m of sediment loading and deposition, minor folds and faults formed leading to uplift within the basin which occurred during the

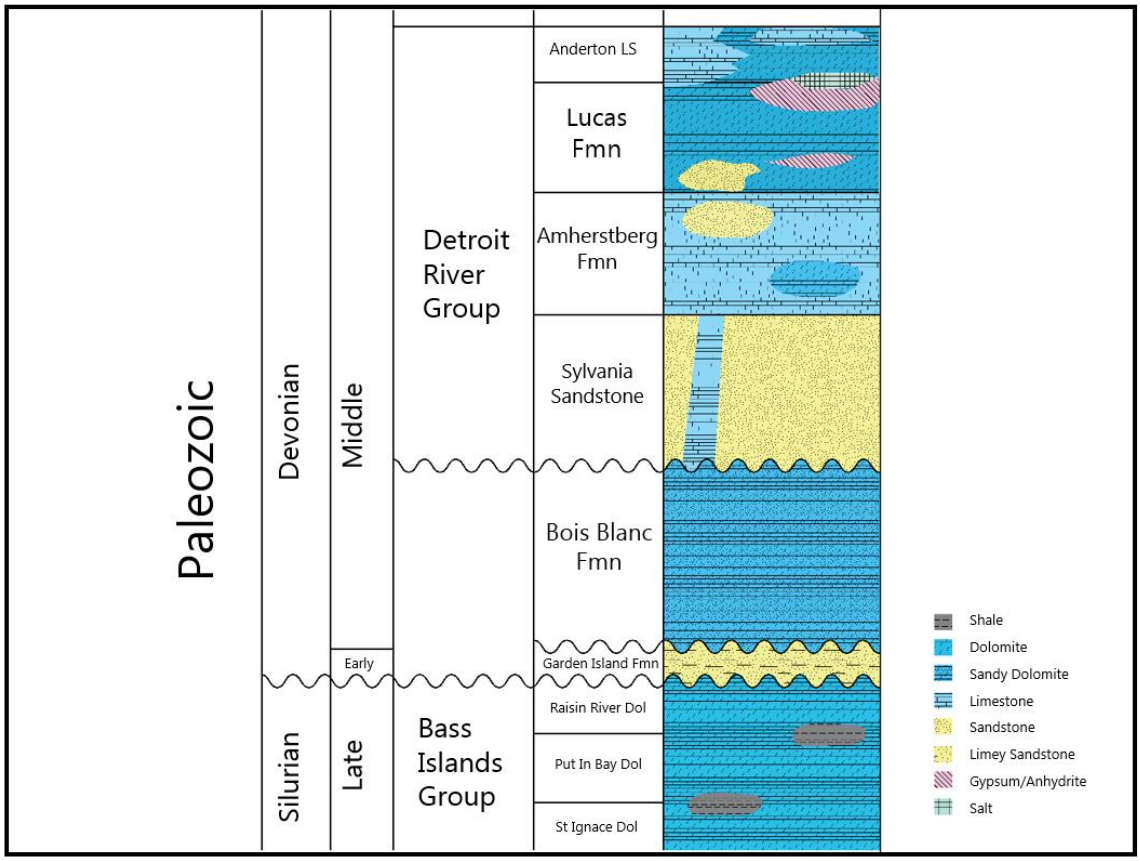

Figure 3) Simplified stratigraphic column of the late Silurian, middle Devonian strata to show their relationship in the subsurface of the Michigan Basin, based on the stratigraphic column from Michigan Basin Geologic Society 2000.

Mississippian and the termination of inland seas during the Pennsylvanian caused erosion and deposition (Landes, 1951, Pirtle, 2003). Ultimately subsidence is dominated by overburdening sediment loading leading to flexure rather than faulting of strata, although both tectonic forces and subsidence of sediments influence the basin (Sloss, 1982).

Multiple arches border the Michigan Basin and they are considered important structural features which isolated the basin during sea level increase contributing to the basin's structural geometry and robust bed thickness. The Cincinnati and Findlay arches border the Michigan basin to the east and south. The Wisconsin arch borders the basin to the west and trends at approximately N20W, and transitions to the La Salle anticline. The Kankakee arch borders the basin to the southwest and trends N45W and connects the Cincinnati and Wisconsin arches (Newcombe, 1932).

The rock units studied within this study are from the Tippecanoe-Kaskaskia cusp, late Silurian to early Devonian eras (Sloss, 1962) (Figure 3). Bass Island formation rocks represent the top of the Tippecanoe sequence which typically represents widespread regional dolomitized carbonates seen in Silurian reef belts across the northern and southern portions of the lower panhandle (Sloss, 1982). The interior sea dominated the basin contributing to the thick carbonate beds. The top of the Tippecanoe sequence is marked by a sharp, erosional unconformity with lithologies dating Early Devonian (Wood and Harrison, 2002). Uppermost rocks of the Tippecanoe sequence represent a substantial depositional hiatus through the distinct weathered appearance of late Silurian rocks including fractured and brecciated blocks, mineralized jointing, and cherty and porous dolomitic rocks. These features extend tens of feet 17 meters beneath the unconformity surface. The erosional surface increases to a higher degree further away from the basin center suggesting less erosional damage within the reservoir units near the study area (Barnes et al., 2009).

Middle Devonian units discussed in this paper, including the Bois Blanc formation, Sylvania Sandstone, and the Amherstberg formation, are part of the basal Kaskaskia

sequence residing superadjacent to the pre-Kaskaskia unconformity of the Tippecanoe sequence (Barnes et al., 2009). Basal Kaskaskia rocks are widespread and typically identifiable due to the sharp interregional unconformity (Gardner, 1974). Such units are lithologically variable where early strata depends on the local erosional processes prior to the Kaskaskia sequence and timing of resubmergence of the unconformity surface below sea level (Gardner, 1974). Lithology generalizations are not possible to describe early Kaskaskia sediments, but carbonates and evaporites are dominant over siliciclastic detrital sediments in the Michigan Basin during this sequence (Sloss, 1982).

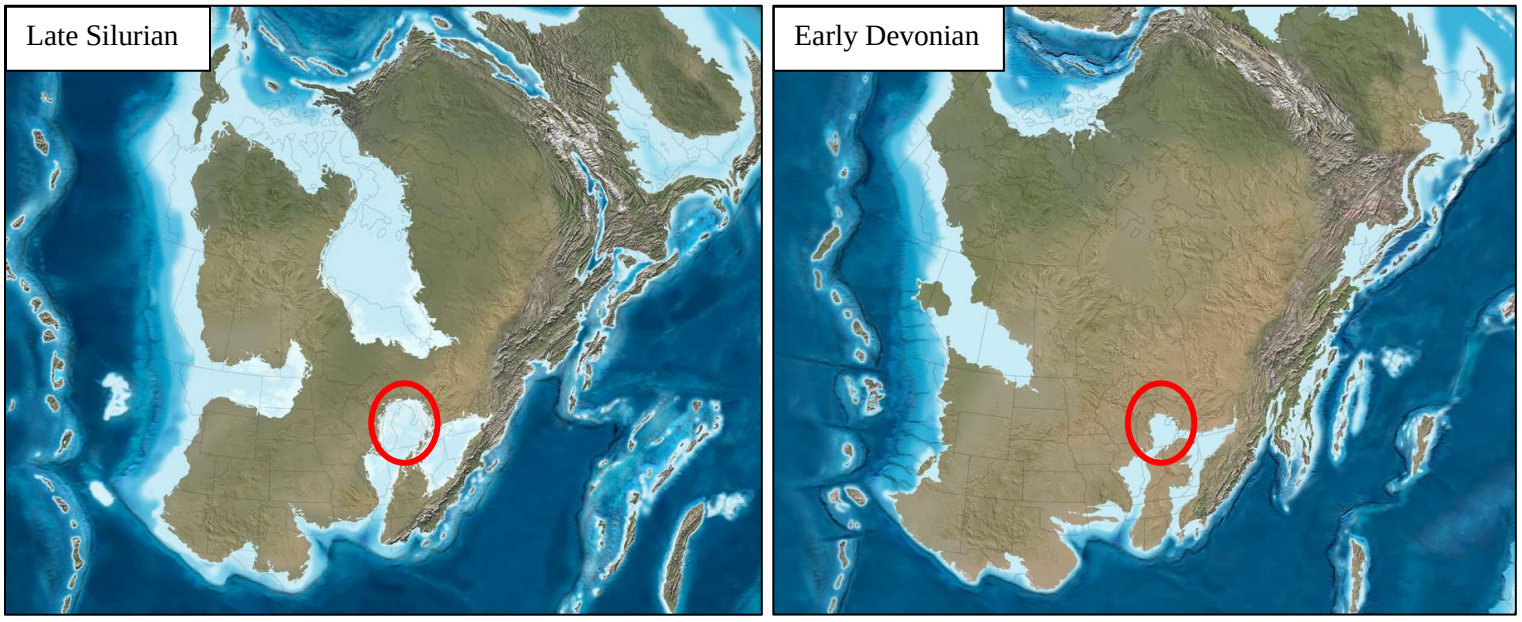

Figure 4) **Left**: Late Silurian land and oceanic water coverage of the Michigan Basin encircled in red. **Right**: Early Devonian land and water coverage of the Michigan Basin encircled in red. Both appear as suggested by Blakey, 2013.

DESCRIPTION OF LITHOLOGICAL UNITS

Bass Islands Formation

The Bass Islands Formation (Figure 5A, 5B) is the uppermost layer of both the Silurian unit and the Tippecanoe sequence (Sloss, 1962). This unit unconformably underlies Devonian strata (Figure 3). Widespread sediments of the Bass Islands cover most of the Michigan Basin where units are thickest in the center (180 m, 590.5 ft) and thin at the basin margin (90 m, 295.3 ft). Strata are mostly light brown to buff dolomite (Sminchak et al., 2009). The rest of the unit contains argillaceous dolostone, anhydrite lenses, and minor shale (Harrison et al., 2009). Samples from the #4-30 State Charlton well reveal blue-grey anhydrite nodules, gray dolomite cement underneath regions of buff dolostone with dark brown laminae. Erosional processes affecting the top of the pre-Kaskaskia unconformity caused breccia-filled sinkholes. This formation displays high porosity (5-37% in Bass Islands Dolomite) from test well cores and is typically identifiable by its low gamma ray signature in well logs (Sminchak et al., 2009). Depositionally, the Bass Islands represents a tidal flat sequence

Bois Blanc Formation

The Bois Blanc Formation (Figure 5C, 5D) is considered the lowest bed of the Kaskaskia sequence. This unit reaches a thickness of 250-300 m (820-985 ft) in the center of the basin and tapers off to 0 m (0 ft) in southwestern Michigan (Gardner, 1974). Its basal rocks consist of clastic and conglomeratic beds that sit atop the Kaskaskia unconformity throughout the Michigan Basin (Stanford, 1967). These middle Devonian rocks vary in lithology in both outcrop and subsurface, but do not have distinct members.

Bois Blanc lithologies include dolomite interbedded with chert, gray limestones, dolomitic limestones, and dolomite (Gardner, 1974). Cherty beds contain brachiopod fossils and some buff limestones contain corals such as *Cladophora*, stromatoporoids, and bistromal interbeds (Gardner, 1974). In counties such as Otsego and Presque Isle, cherty limestone and dolomite containing stromatoporoids dominate the Bois Blanc lithology and is very similar to the Amherstberg limestone (Stanford, 1967). It is thought in this region that the Bois Blanc may grade into the Amherstberg (Quinlan, 1990). Samples from the #4-30 State Charlton well reveal cherty limestone and dolomite with black laminations approximately .05-2 mm thick. The Bois Blanc grades upward into the Sylvania Sandstone in the central to southeastern portion of the lower peninsula of Michigan. The mixed lithology and abundance of fossil species in part suggest a depositional setting such as a transgressive carbonate blanket in a restricted marine environment during a period of relatively passive tectonism (Harrison et al., 2009). The mixed lithology also promotes fair porosity and permeability, especially in sandstone-based regions (Gardner, 1974).

Sylvania Sandstone

The Sylvania Sandstone is a Middle Devonian sublitharenite sandstone that is considered a basal sand of the Kaskaskia Sequence (Gardner, 1974) and of the Detroit River Group (Gardner, 1974). Average grain sizes range between 0.18 to 0.4 mm and are typically rounded (Gardner, 1974). Quartz overgrowth cements exist between most sublitharenite sandstone grains, and secondary enlargement of grains denoted by doubly terminated quartz crystals indicate possible silica-saturated waters moving through the

sand deposits (Gardner, 1974). In southeastern Michigan the Sylvania sandstone is a dolomitic to cherty-quartzose sandstone (Barnes et al., 2009). The maturity and sorting of grains indicate eolian origin (Gardner, 1974) reworked in a marine setting (Carmen, 1936). The distribution of grains and temporary sea regression deposited Sylvania sediments in a bar-beach setting trending northwest (Rodwan, 1986). The lack of widespread distribution results in the absence of Sylvania rocks in much of the basin. Grains are smallest (fine-grained sand) in the central-southeastern portion of the basin and increase in size to medium-grained toward the southeast into Ohio (Stanford, 1967). Grain size and crossbedding pattern correspond to regional dip and thickening of the basin, likely originating from the Findlay Arch acting as the main distribution center of the sandstone sediments (Newcombe, 1932). Fossil species found in the upper portions of the Sylvania can also be found in the lower parts of the Amherstberg in the southeastern region of the Michigan Basin where upper Sylvania sandstones tend to grade into and interbed with overlying carbonates likely due to sea transgression (Gardner, 1974).

Amherstberg Formation

The Amherstberg Formation (Figure 5E) is a regional carbonate unit that covers most of the Michigan Basin (Barnes et al., 2009). It is middle Devonian in age and overlies and intertongues with the Sylvania Sandstone (Stanford, 1967). This formation was deposited in a shallow, restricted ocean basin evident by the many evaporative and unstable minerals found within the unit such as anhydrite and calcium carbonate (Dunham 1962). The Amherstberg may also directly overlie the Bois Blanc where Sylvania strata is absent (Gardner, 1974). The base of the Amherstberg is typically

defined by its lowermost anhydrite layer and contains two common members; the Meldrum Member and the Filer Sandstone (Barnes et al., 2009).

The Meldrum member is characteristically dark gray to dark brown and black and considered a microcrystalline wackestone (Dunham 1962). This member is often referred to as the Black Lime due to its dark color (Gardner, 1974). The Meldrum lacks apparent bedding laminations but is highly coralline and abundant in crinoids and brachiopod and bryozoan fragments. Samples from the #4-30 State Charlton well reveal dark gray limestone with black shale laminations (0.05-1.0 mm) and coral fragments ranging 6-15mm in size. Beds reach a maximum thickness of 91 m near the center of the Michigan Basin, near Saginaw Bay, and reach a taper away in regions where Sylvania beach sands dominate in the southwest region of the basin (Stanford, 1967). Northern and Western basal chert of the Meldrum is often confused with Bois Blanc sediments due to the high levels of dolomitization (Barnes et al., 2009). Dolomitization of sediments likely occurred through the downward flow of basinal brines enriched in Ca^{2+} and Mg^{2+} (Bohnhoff et al., 2010). The overlying Amherstberg member, the Filer Sandstone, likely served as a temporary aquifer for such waters which infiltrated the Meldrum member, casting dolomitic cements in underlying strata (Gardner, 1974).

The Filer Sandstone is mostly arkosic beach sand which directly overlies the Meldrum member in the western margins of the Michigan basin (Gardner, 1974). The well sorting of the sand indicates a temporary regression in the western portion of the basin causing a facies change (Stanford, 1967). The Filer exists as lenticular sandstones and is highly discontinuous where found in the stratigraphic column (Barnes et al., 2009).

A

B

Figures 5A, 5B) Bass Island specimen from St Charlton Well #4-30, 3451'6"; (A) Buff to brown dolomite with small chert nodules. (B) Anhydrite and dark gray dolomite.

C

D

Figures 5C, 5D) Bois Blanc specimen from St Charlton Well #4-30, 3410'8"; (A) Buff carbonate with thin dark dolomitic laminations, and shale laminations. (B) dark cherty dolomite with fractures.

E

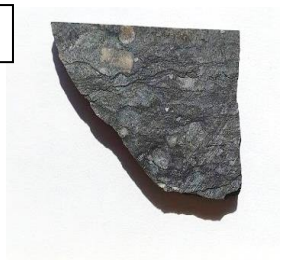

Figure 5E) Amherstberg specimen from St Charlton Well #4-30, 3037'6"; Dark gray fossiliferous dolomitic limestone featuring thin shale interbeds.

CARBON DIOXIDE IN GEOLOGIC MEDIA

Understanding how long and to what extent mobile CO_2 will remain in the subsurface is important to CCS implementation. Several types of sedimentary storage reservoirs are considered when computer modelling, laboratory, and field experimentation including depleted oil and gas reservoirs and deep saline aquifers (Barnes et al., 2009; Mehnert et al., 2014; Sanguinito et al., 2018, etc.). The following review section intends to highlight CO_2-brine interactions with different storage media to identify geochemical trends resulting from carbon dioxide storage activities.

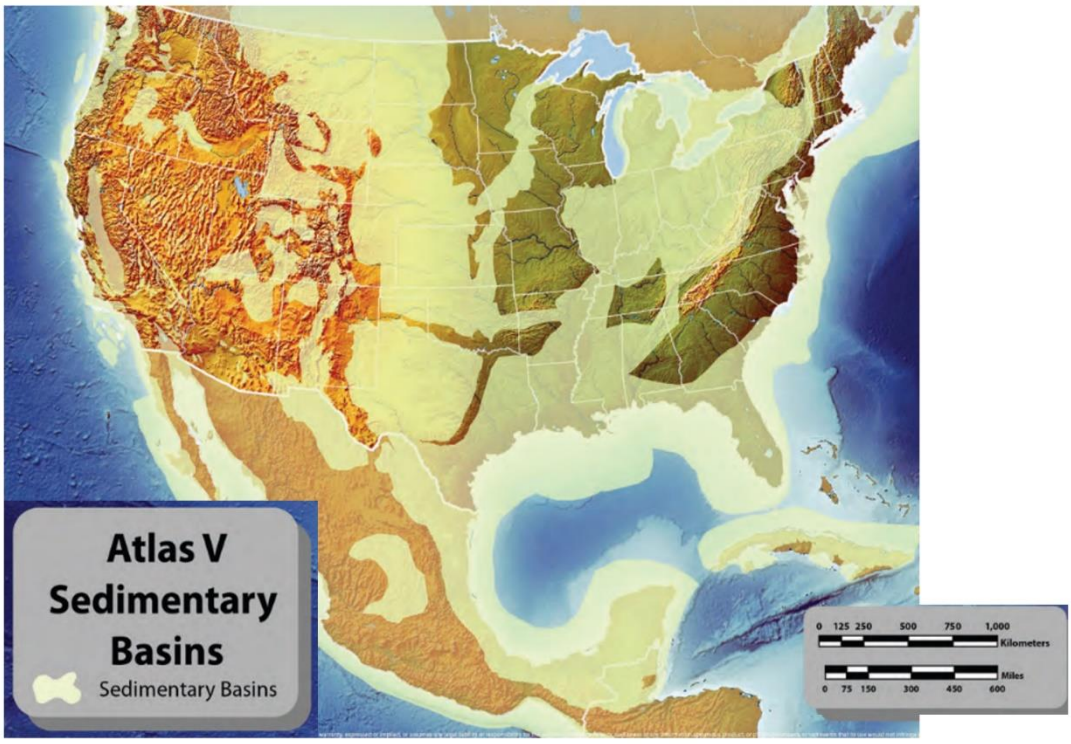

Figure 6) Department of Energy-identified locations of sedimentary basins across North America which contain CO_2 storage potential. Modified from US Department of Energy and NETL, 2015.

Globally, regionally extensive sandstones (i.e. saline formations) have been identified as potential CO_2 storage reservoirs (Wigand et al., 2008; Lu et al., 2011; Mehnert et al., 2014, US Department of Energy and NETL, 2015) (Figure 6). These sandstone units vary in composition; however, they all contain major amounts of quartz (66-90%), minor feldspars and clays, and have high Total Dissolved Solids (>10,000 ppm) formation fluids. If the sandstones are porous and permeable, it could be a target for CO_2 storage, but if the formation contains impermeable lithologies, it could act as a confining zone to prevent the migration of CO_2 (US Department of Energy and NETL, 2015).

Mehnert et al., determined, when modelling and experimental conditions mimic that of reservoir conditions of the Mt. Simon Sandstone (24.4-44°C (76-11°1F), 0.5-13.7 MPa (72.5-1987 psi)) that a 5,000 million ton CO_2 plume persists 5,000 years after initial injection. The modelled injection featured 500 million tons per year over a 10-year period. Over half of injected CO_2 became trapped residually, while nearly a third of the plume remained mobile. The remaining CO_2 (15%) dissolved within the brine. Mineral trapping remained as a negligent sink for the injected CO_2 plume.

Wigand et al., replicated reservoir conditions of the Bunter Sandstone formation, one of the largest saline aquifer-bearing formations in Europe by reacting CO_2 and formation brine with rock samples at 60°C (140°F) and 30 MPa (4350 psi) for 1496 hours. The lithic arkose with major quartz, K-felspar, and albite, dolomitic and clay cement, and trace illite and kaolinite released several major and trace elements from the sandstone. Major elements included Ca, Mg, Fe, and Mn. Trace elements included Sr, Ba, and Pb. Quartz grains and the dominant illite cement was not affected while dolomite

cement dissolved. Equilibrium speciation calculations using PHREEQC highlighted that pH levels never stabilized at a defined value. Their results confirm that initial pH spike within the fluid concentration was controlled by mineral dissolution, which, in turn, was followed by a subsequent decrease in pH as carbonate mineral precipitation occurred. The authors believe that the dissolution of iron (III) and manganese (IV) hydroxides released Sr, Pb, Bi and REEs, and Co, Cd, Zn, and Cu, respectively, from the sandstone into the formation brine.

Lu et al., 2011, carried out high heat laboratory experiments with acidified brine (4.1 pH) and the Navajo sandstone – a regionally extensive saline aquifer in the Western United States in order to expedite reactions within their samples (200°C (392°F) , 30 MPa (4350 psi)). Like Wigand's results, this study also determined that Ca and Mg were primary cations released from the sandstone into the brine, including similar "toxic" trace elements such as Cu, Zn, and Ba. Clay coatings contributed to a severe decrease in permeability, and trace amounts of carbonate minerals precipitated out of solution. Mineral trapping was also determined to not be very significant, like the findings of Mehnert, and most CO_2 was trapped by dissolution into the brine.

Geologic formations are considered targets for CO_2 storage if they are highly porous and permeable, allowing for the injection and flow of fluids within pore networks. The successful containment of CO_2 typically relies on an impermeable top cap rock (seal) to prevent the upward flow of the injected CO_2 plume. Traditionally, shales have been identified as caprocks, however in recent years, shales have been investigated as potential reservoirs too. Because shales, like the Marcellus and Utica Shales, have proven hydrocarbon reserves, studies have investigated shales as storage reservoirs for CO_2,

applying CO_2 as an enhanced oil recovery agent, and examining CO_2-shale interactions for cap rock alterations (Johnson et al., 2001; Sanguinito et al., 2017, 2018; Zhou et al., 2018; Goodman et al., 2019, 2020; Kutchko et al., 2020).

Johnson et al. modelled CO_2 - aquifer systems with internal shale permeability structures to identify CO_2 migration path changes with inclusion of a shale barrier as well as determining changes within the shale geochemistry. The modelled system included a 200 m (656 ft) aquifer with a 25 m (82 ft) shale barrier, topped by another 25m confined aquifer. Over the course of 10 years, 100,000 tons were injected into the "sea water type" aquifer. After 5 years 15% of CO_2 is trapped by dissolution, and after 10 years increases to 32%. The saline aquifer pH was found to fluctuate between 4.5-7.1 over 20 years. Only the basal 5m (16ft) of the carbonate shale was found to be affected by the formation fluid. Precipitation by mineral trapping indicated that Dawsonite, Magnesite, and Siderite are the most likely carbonate minerals to form on the shale barrier and porosity decreased from 0.05% to 0.046% over 20 years. Johnson argues that precipitation of carbonate minerals within shale fractures and pitted surfaces would serve the shale well to increase the integrity of the shale as a cap rock.

A suite of experiments performed by Sanguinito et al. 2017, 2018, Goodman et al. 2019, 2020, and Kutchko et al. 2020 investigated Marcellus and Utica shales for their CO_2 storage potential, and investigated CO_2 as an enhanced oil recovery agent. The studies determined that CO_2 (alone) and CO_2-saturated interactions with a carbonate mud Utica shale produce significant pitting and etching. Reactions taking place at reservoir conditions (40°C (104°F) and 10.3 MPa (1494 psi) for 35 days also cause a decrease in micropore surface area and volume and an increase in mesopore volume from carbonate

dissolution. FTIR results indicated a “buffering behavior” within carbonate species’ intensities over a 5-week period. The buffering behavior was likely due to carbonate dissolution and precipitation reactions. This is consistent with Johnson’s findings above. FTIR results also indicated dissolution of silicates, however SEM results revealed quartz and pyrite remained largely unaffected after exposure. The increased pore space may be more effective for storage or may assist with hydrocarbon recovery.

Zhou et al. studied 4 types of shale and their reaction with supercritical CO_2 ($SCCO_2$) and brine during FTIR adsorption experiments. Carbonaceous, silty, calcareous, and clay-rich shales were powdered and sieved to 150um and exposed to $SCCO_2$ at 8, 12, and 16 MPa (1160, 1740, 2321 psi) and 35°C (95°F) for 7 days. All experiments showed decreases in silicate and carbonate minerals as well as aromatic hydrocarbons. The authors concluded that CO_2 and brine may serve better as “environmentally friendly fracking fluid” within shales like the findings of Goodman et al., 2019.

CHAPTER III

METHODOLOGY

MATERIALS

Rock Samples

Rock samples (Figures 5A-5E) from State Charlton #4-30 Well from Otsego County, Michigan from 3 “library slabbed” drill cores, drilled by Core Energy, LLC were used to aid in the characterization of late Silurian – middle Devonian reservoir and cap rocks. Core 1 spans from 3,030-3,063 feet (923.5-933.6 m), core 2 spans from 3,063-3,090 feet (933.6-941.8 m), and core 3 spans from 3,400-3,520.5 feet (1036.3-1073 m). All depths of the cores represent actual subsurface depth from the top of the well. The Vornlocher et al. NETL technical report includes computerized tomography analysis that identified that the Amherstberg formation solely exists within cores 1 and 2. Core 3 contains the Bois Blanc and Bass Islands anhydrite formations. For the purposes of this study, core 1 and 2 were chosen for further analysis (Figures 7A-7D). One sample from 3,037 feet (926.5 m) was used for geochemical testing.

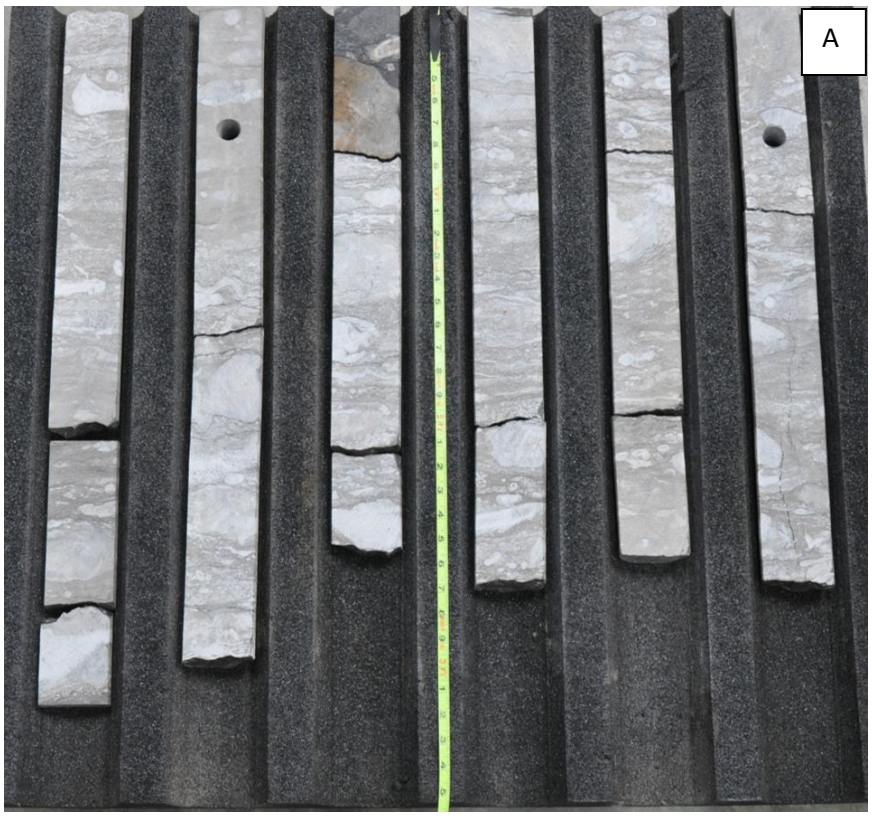

Figure 7A) Amherstberg Core photos from State Charlton Well #4-30, depths 3,030-3,046 feet. Images courtesy of NETL.

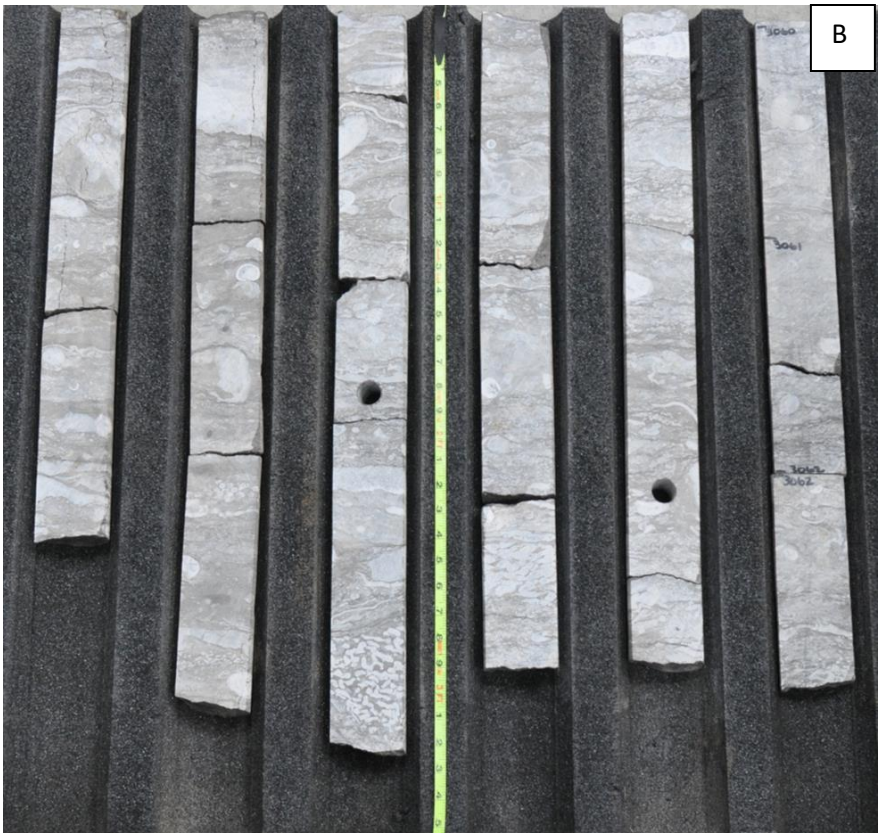

Figure 7B) Amherstberg Core photos from State Charlton Well #4-30, depths 3,046-3,060 feet. Images courtesy of NETL.

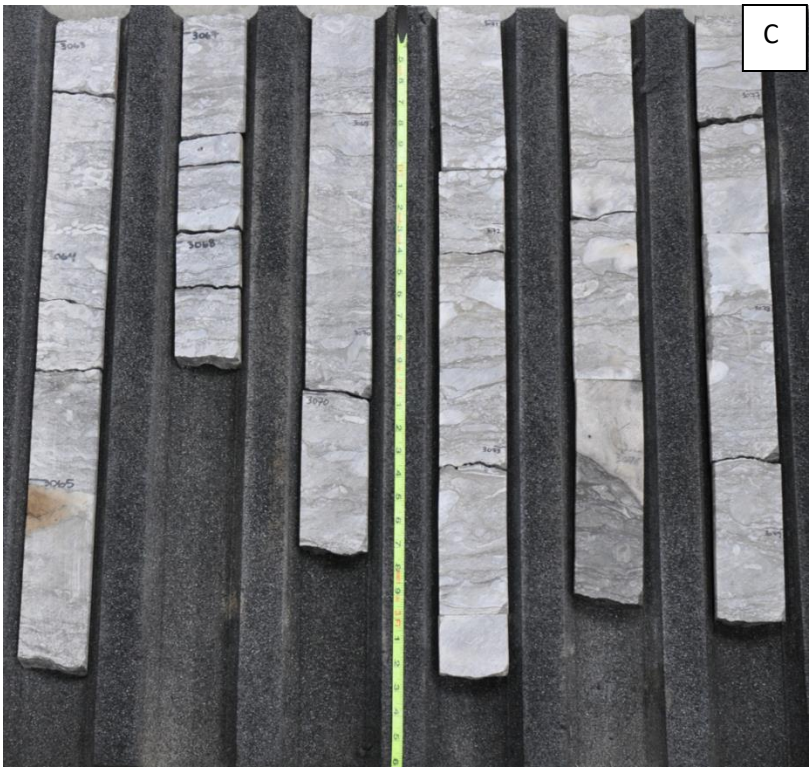

Figure 7C) Amherstberg Core photos from State Charlton Well #4-30, depths 3060-3079 feet. Images courtesy of NETL.

Figure 7D) Amherstberg Core photos from State Charlton Well #4-30, depths 3079-3090 feet. Images courtesy of NETL.

Brine

The brine used in sample reactions was based on sampled water from the Sylvania sandstone, the underlying sandstone layer of the Amherstberg, from the findings in Wilson and Long, 1992. The brine recipe is from Well 5019 – Mecosta, County Michigan and its components are in Table 1. The Sylvania sandstone brine was selected based on its stratigraphic position above the Bass Islands injection formation and beneath the Amherstberg limestone (Figure 3). Buoyant CO_2 will rise upward through the Sylvania sandstone and interact with the formation fluid before interacting with the Amherstberg formation.

Table 1 Concentration of Synthetic Brine* used in Static Autoclave Reactions

Reagent	Concentration (g/L)
$CaCl_2 \cdot 2H_2O$	265.575
$MgCl_2 \cdot 6H2O$	86.97
NaCl	54.18
KCl	17.675
$SrCl_2 \cdot 6H2O$	7.12
NaBr	3.94
$NaHCO_3$	0.45
Na_2SO_4	0.003

*Approximate Total Dissolved Solids of 298,760 mg/L and pH of ~4.9; Based on Wilson Long 1993 paper, sample ID 5019, from Detroit River Group.

STATIC AUTOCLAVE REACTIONS

Samples to be reacted were placed in a 500 mL Teflon container within a Parr 1L static autoclave. The vessel was purged with nitrogen after it was closed and sealed. CO_2 was flowed into the vessel and pressure was increased to 13.8 MPa (2001.5 psi) and temperature maintained at 31.5°C (89°F) for 2 weeks to mimic reservoir conditions (Harrison et al., 2009). This method was repeated and completed a second time with the inclusion of 250 mL of synthetic Sylvania Sandstone brine submerging the sample within the Teflon container. After 2 weeks of reaction time, pressure and temperature was released within the vessel over the course of 24 hours.

SCANNING ELECTRON MICROSCOPY AND FEATURE RELOCATION

An FEI Quanta 600 scanning electron microscope (SEM) equipped with energy dispersive X-ray spectroscopy (EDS) was used to characterize the surface morphology and geochemistry of the Amherstberg samples (Figure 8). SEM images of the samples were used to visualize micro-, meso-, and macropore surfaces and resulting alteration from exposure testing. Mineral precipitation and dissolution were also observed through SEM imagery. EDS data were used to characterize the relative abundance of minerals present. The elements and their abundance provided insight into which were minerals present at each sample location. To characterize the samples, initial images were taken of the sample's surface. Limestone features were recorded within samples by their specific X, Y, and Z coordinates, and these specific sites were relocated and reimaged after each exposure experiment (first CO_2 and the sample, then CO_2, brine and the sample) to

characterize and quantify localized geochemical changes (See Appendix A for site locations. See Appendix B for all SEM images). Images were taken in sequential magnification (100, 200, 500, 1000, 2500, and 5000x) at each site to aid in feature relocations. Backscattered electron images were collected at a working distance of approximately 10mm and bean voltages ranging from 10-20kV to accommodate for surficial charging effects (Figure 9).

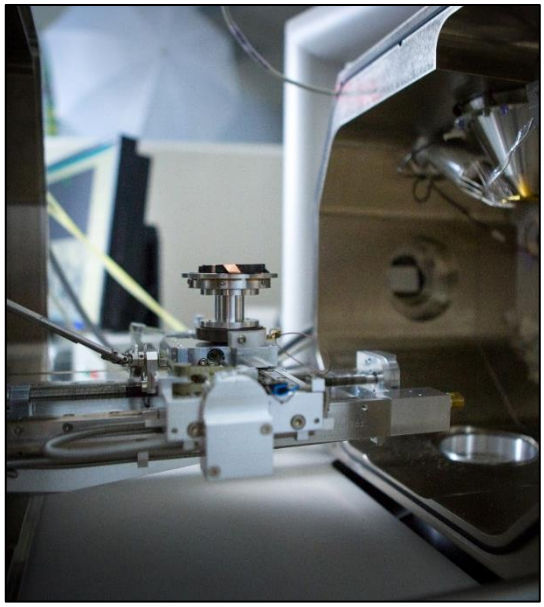

Figure 8) FEI Quanta SEM with chamber open to show sample on stage. Image appears courtesy of NETL

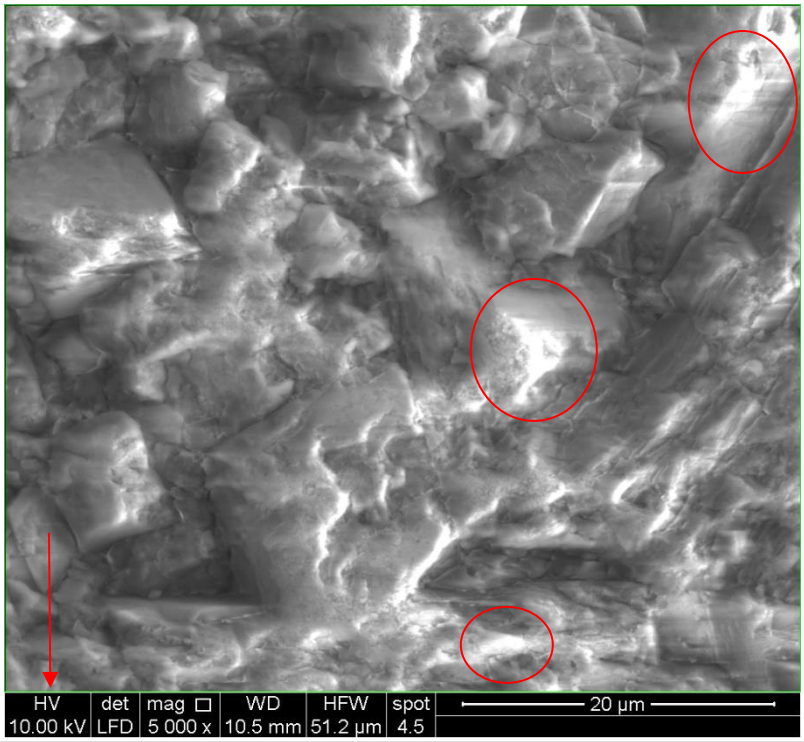

Figure 9) SEM image of Amherstberg limestone with surficial charging effects caused by a rough, unpolished surface (indicated by a red circle). The leftmost box in the measurement bar (indicated by an arrow) displays the beam voltage.

X-RAY DIFFRACTION SPECTROSCOPY (XRD)

Unexposed powdered Amherstberg Limestone samples were taken from experimental rock chips for qualitative mineral analysis by x-ray diffraction. The XRD spectra produced data to determine the relative mineral abundances within the limestone. XRD data supplements data received from EDS analyses to aid in verifying geochemical changes within the Amherstberg.

INDUCTIVELY COUPLED PLASMA OPTICAL EMISSION SPECTROSCOPY (ICP-OES)

Sylvania sandstone brine was analyzed before and after exposure to Amherstberg samples through ICP-OES and ion chromatography experiments at NETL-Pittsburgh. The ICP and IC tested for over 40 ions within pre and post exposure brine. pH values were also collected to further characterize the geochemical alterations and observed visual changes within the SEM imagery.

IMAGE ANALYSIS OF SURFICIAL POROSITY

The following procedure was based off of the image analysis developments using ImageJ listed in detail within Kutchko et al., 2013. In this study, porosimetry was unable to be performed due to the nature of the core which was unable to be cored further. In attempt to identify localized porosity, image analysis was utilized to quantify changes to porosity in the Amherstberg sample. Because of the direct comparison made possible by feature relocated SEM images, pre- and post-exposure images from each sample site were analyzed. In backscattered SEM images, grayscale values are based on the tendency of the element on the sample surface to deflect incidental electrons from the SEM's electron beam. Heavy elements tend to deflect these electrons easier than lightweight elements, thus, heavy elements appear brighter with white and near white values and lighter elements appear darker.

In practice, variations may occur from scan to scan and can be affected by environmental variables such as surface roughness, or if a sample is coated or not. From time to time surficial defects may cause shadowing or electrical charging which is not always representative of the sample surface chemistry.

To determine the percentage of porosity on a sample's surface, an image was separated into two classes: rock matrix and pore space (Figure 10A). Amherstberg samples have many materials such as carbonate matrix, dense fossil fragments, pyrite minerals, and shale inclusions. Because of varying grayscale values from site to site, it was most efficient to perform the analysis by hand. At each site, nearly 100 samples were taken to collect histogram data and determine threshold values for average gray colors and average pore representatives. Once the two classes are differentiated, the image was converted to a binary image and pore areas can be measured to produce a percentage representing their surface area within a site (Figure 10B). This method was applied to 200x and 5,000x magnification pre-exposure, dry-exposure, and wet-exposure images.

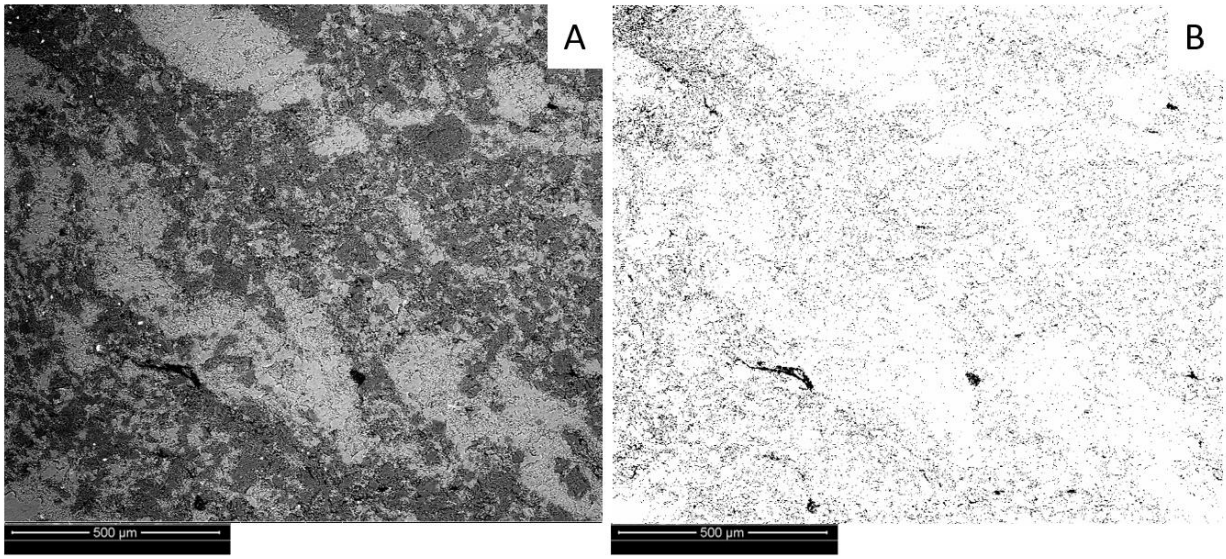

Figures 10A, 10B) BSED SEM images of non-reacted Amherstberg limestone before(A) and after (B) image analysis techniques were applied. Black pixels represent porosity and white pixels indicate rock material. 200x magnification.

CHAPTER IV

RESULTS

SEM-EDS

High-resolution field-emission scanning electron microscopy (FE-SEM) was used to examine the Amherstberg limestone solid samples before and after reactions with dry CO_2 and CO_2 saturated synthetic Sylvania sandstone brine. As described in the methods section above, feature relocation techniques were applied to ensure that the same region could be analyzed and compared before and after reactions. In these images, before reaction refers to non-reacted samples, dry reaction refers to CO_2 and limestone reaction, and wet reaction refers to the reaction of limestone sample and CO_2-saturated brine. In Figures 14A-14D and 16A-16D, white regions represent pyrite, light grey regions represent limestone and dolomitic regions. Dark gray to nearly black regions represent organic, carbon rich areas such as shale and void spaces are black. Not all minerals have been labeled in 14A-14D and 16A-16D.

Unaltered Amherstberg samples revealed the Amherstberg is a dolomitic limestone with both calcium and magnesium phases present with the sample matrix (Figures 12A, 12B). Calcium phases represent 30% of the map area and magnesium phases represent about 10% of the map area (Figures 11A, 11B). Some grains and regions

of matrix were either distinctly calcium-rich, distinctly dolomitic, or had mineralogical transition zones on the same grain (Figure 11A). The Amherstberg also contained pyrite as both framboids and single euhedral grains (Figures 14A, 14B). Secondary electron images revealed that porosity appeared very low, visually, even at high magnifications (Figure 11B).

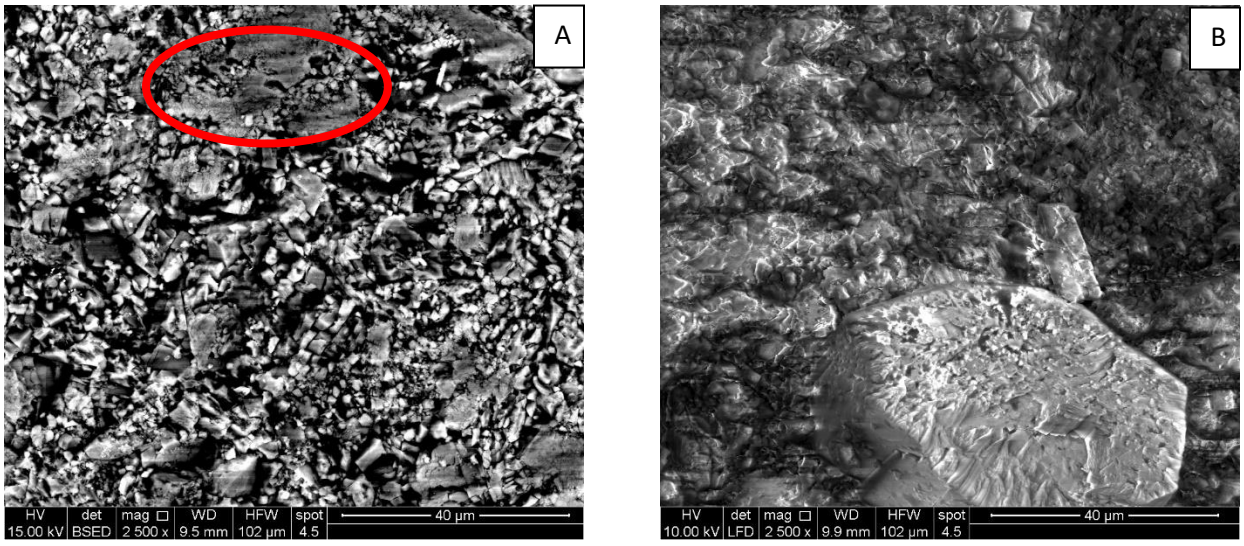

Figures 11A, 11B) (A) Backscatter SEM image of the Amherstberg sample with a grain that has a calcite-rich to magnesium-rich transition zone, magnification: 2500x. (B) Secondary electron image of the Amherstberg sample showing almost no visible porosity at 2,500x magnification.

The Amherstberg sample showed little variation when exposed to supercritical CO_2 alone. Mineralogically, there were no reportable changes (Figures 13A, 13B). Samples were physically altered displaying an etched surface after exposure to CO_2. Pore spaces, surface pitting and surface erosion became visible in some regions (Figure 14D).

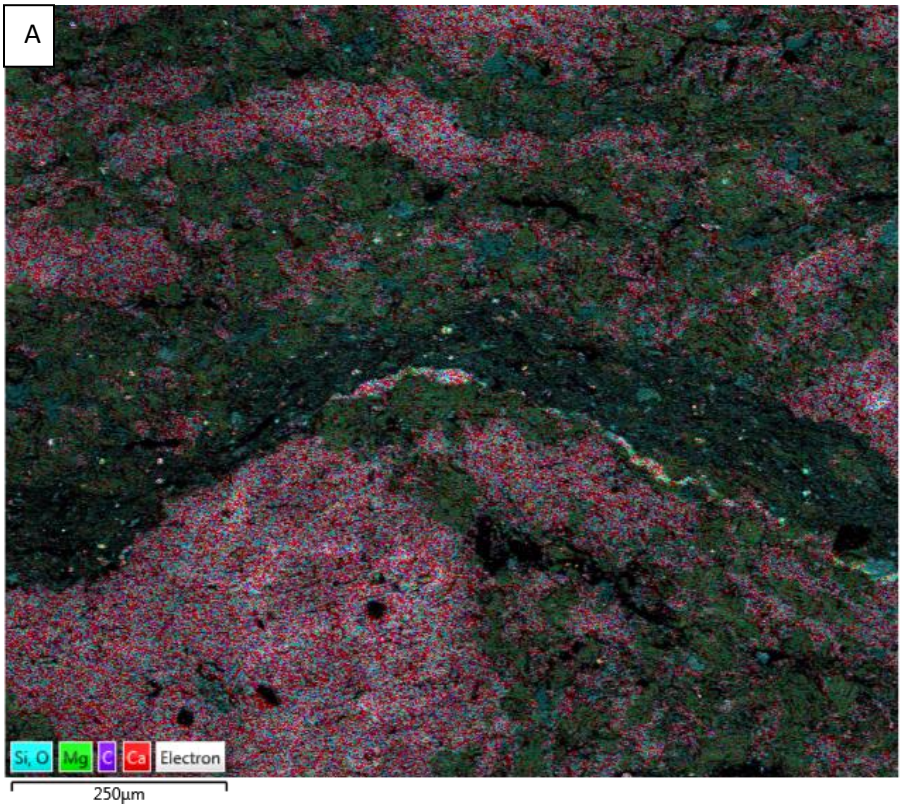

Figure 12A) EDS map of the unaltered Amherstberg sample. Red regions highlight calcium-rich phases and green regions highlight magnesium-rich phases.

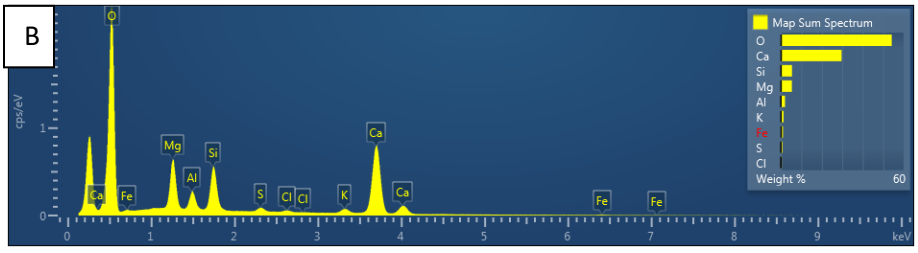

Figure 12B) An overall map spectrum showing the elemental distributions over the entire map.

Before

After

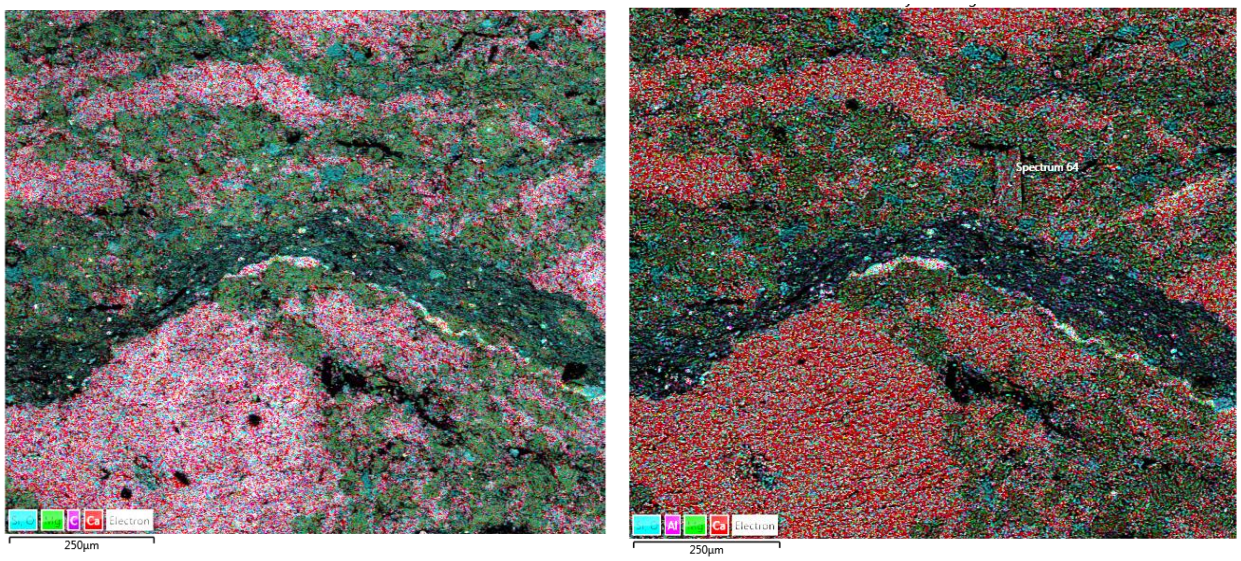

Figure 13A) Similar elemental maps before and after exposure to dry CO_2. Removal of surficial carbon occurred after exposure.

Before

After

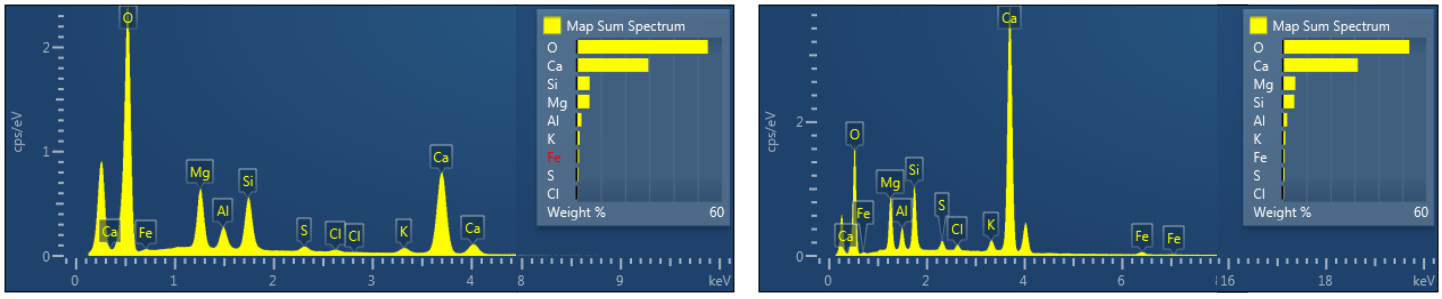

Figure 13B) Map sum spectra of before and after exposure to CO_2 shows virtually no difference in maps of the same location. The spectrum on the right shows a strong calcium peak but weight percentages are nearly the same.

Unreacted vs. Dry CO_2

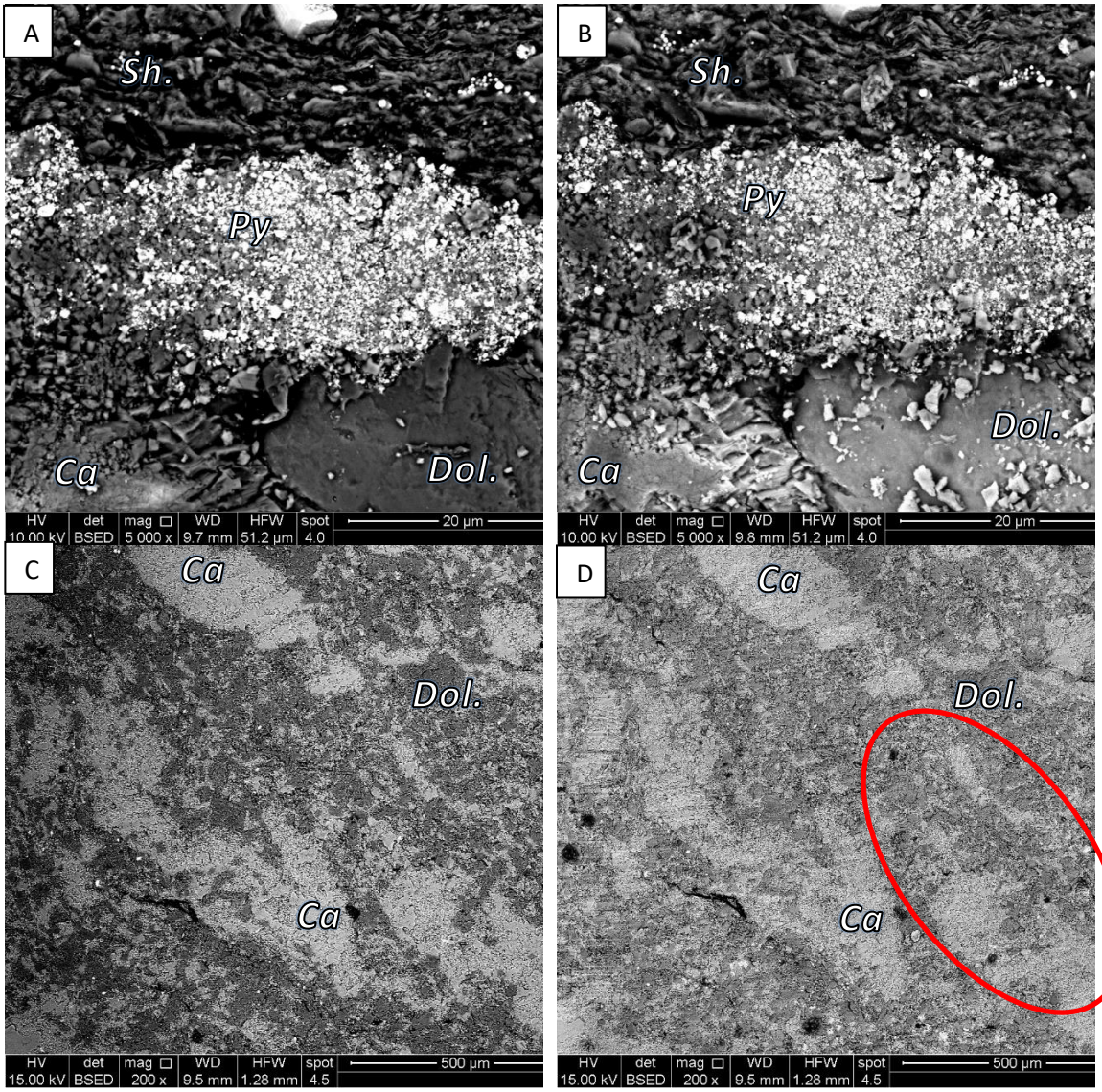

Figures 14 A-D) SEM images of the Amherstberg limestone sample. (A) Framboidal pyrite, shale, calcite and dolomite, 5000x magnification. (B) Dry-CO2 reacted limestone shows little change, 5000x magnification. (C) Unreacted sample displaying calcite (light gray matrix), and Mg-rich dolomite (dark grey matrix), 200x magnification. (D) Dry-CO2 reacted limestone shows surface pitting and pore spaces as circled, 200x magnification.

The Amherstberg sample showed significant alteration when exposed to supercritical CO_2 and Sylvania Brine. Salt precipitated out of the solution and formed large (20-250µm) euhedral salt crystals (Figures 15A & 16B). Precipitated salt crystals include NaCl, KCl, $MgCl_2$, and $CaCl_2$. Calcium phases represent under 25% of the map area, magnesium phases still represent about 10% of the map area, Chlorine phases increased from nearly 1% to over 10% of the map area composition (Figures 12B, 15B). Mg-rich and pyritic regions appeared much more resistant to CO_2-saturated brine.

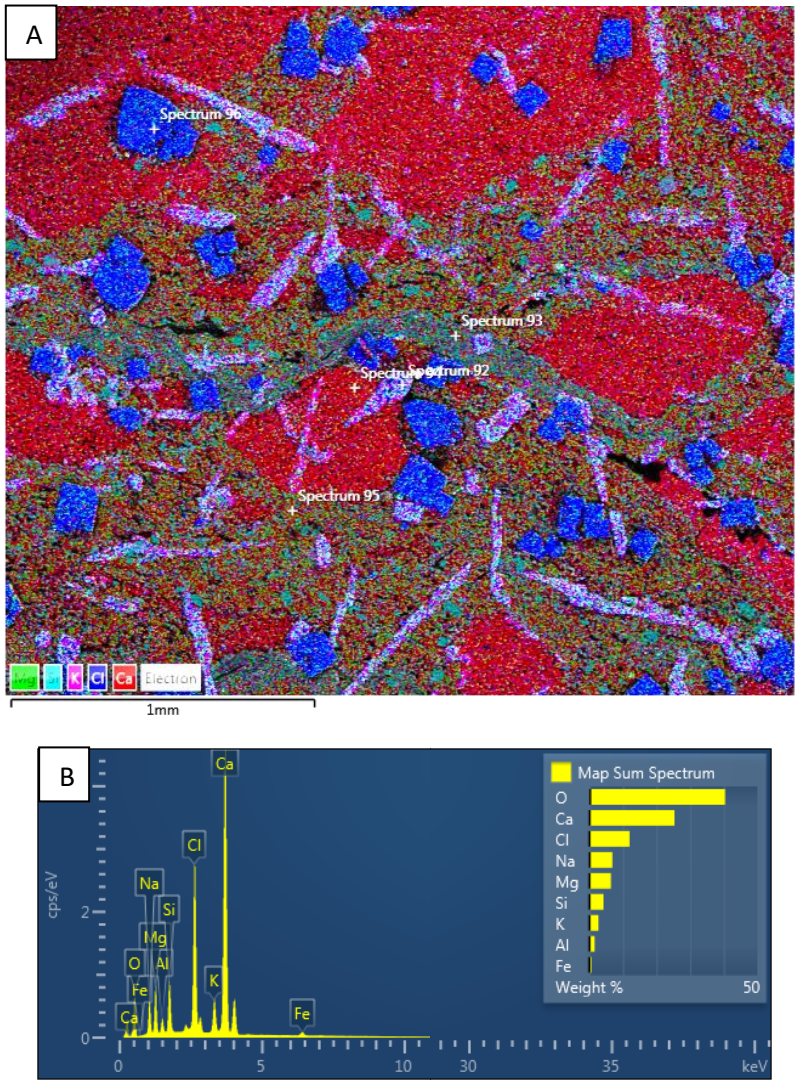

Figures 15A, 15B) (A) EDS map of the Amherstberg sample post CO_2-brine reaction. Red and green regions represent calcium and magnesium phases. Blue and purple regions are salt crystals. (B) Spectrum totals reveal an increase of elements in salt phases, and a decrease in calcium. There appears to be no change in magnesium.

Samples were physically altered displaying an etched surface after exposure to CO_2-saturated brine. Pore spaces, surface pitting and surface erosion increased in many regions of the sample, visible on all magnifications (Figures 16A-D).

Unreacted vs. CO_2-Brine reaction

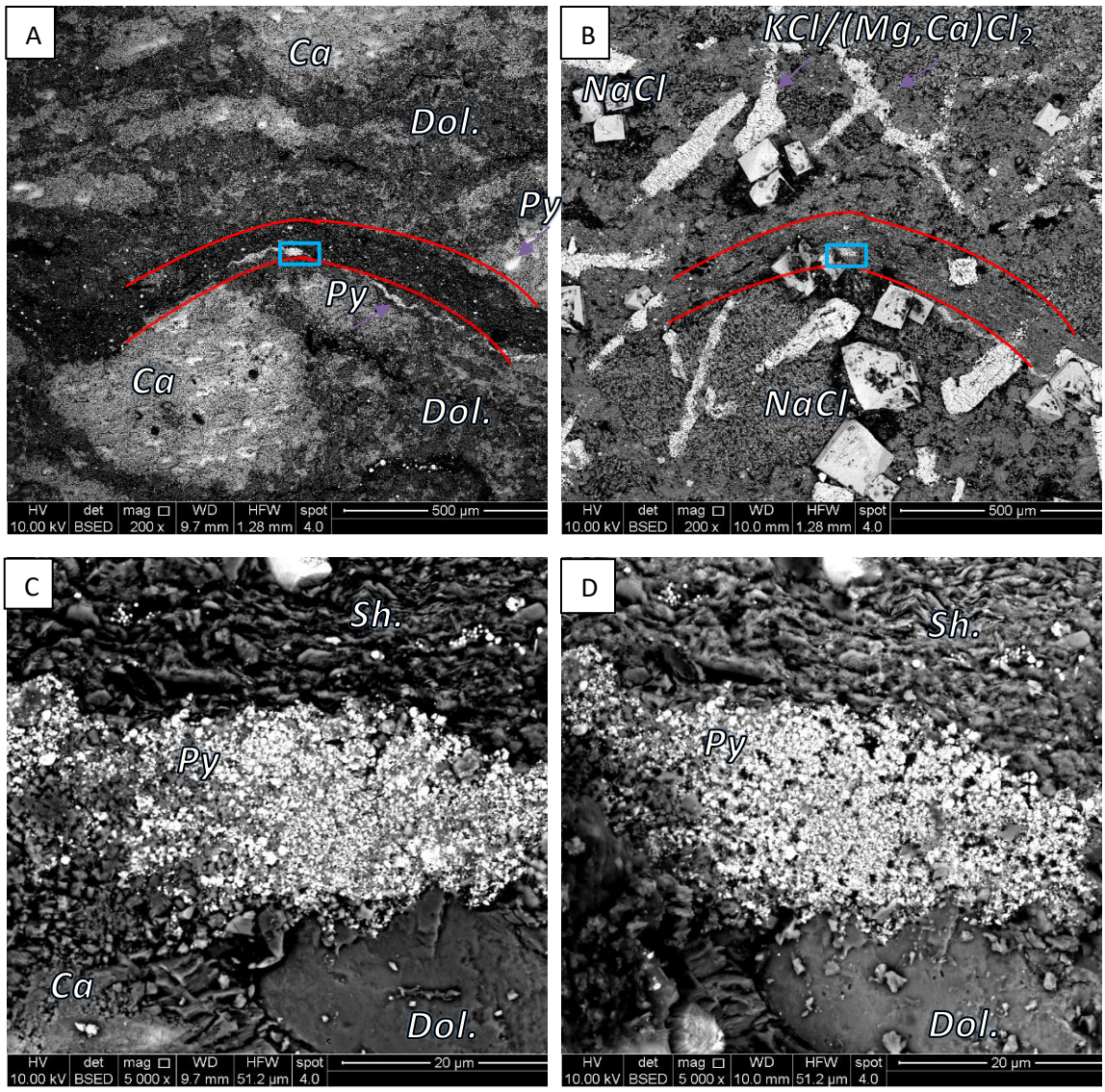

Figures 16 A-D) SEM images of the same Amherstberg limestone sample. (A) Unreacted sample displaying calcite (light gray matrix), dolomite (dark grey matrix) and shale interbed outlined in red, and pyrite is labelled, 200x magnification. (B) Brine-CO_2 reacted limestone featuring euhedral NaCl crystals and bands of various salt crystals, including $CaCl_2$, $MgCl_2$, and KCl, covering and forming within the sample surface; Calcium-rich species are no longer present in the image, 200x magnification . (C) 5000x zoomed in image of blue box in A showing framboidal pyrite, shale, calcite and dolomite. (D) 5000x zoomed in image of blue box in B, post-reaction, where Ca-rich species are no longer present creating pore spaces.

Figure 17 shows a site of the Amherstberg after wet reaction, imaged at 5,000 times magnification that is entirely composed of euhedral $CaCO_3$ minerals in a region of calcium-rich matrix. The unweathered and euhedral nature of the grains suggest that the crystals formed out of a calcium-rich solution. A Ca^{2+}-bearing solution is possible from the absent calcium phases post reaction and may suggest "dynamic" porosity where carbonate species dissolve and re-precipitate based on the surrounding solution's composition. Longer term reactions and studies may ultimately lend insight to porosity and permeability changes over time.

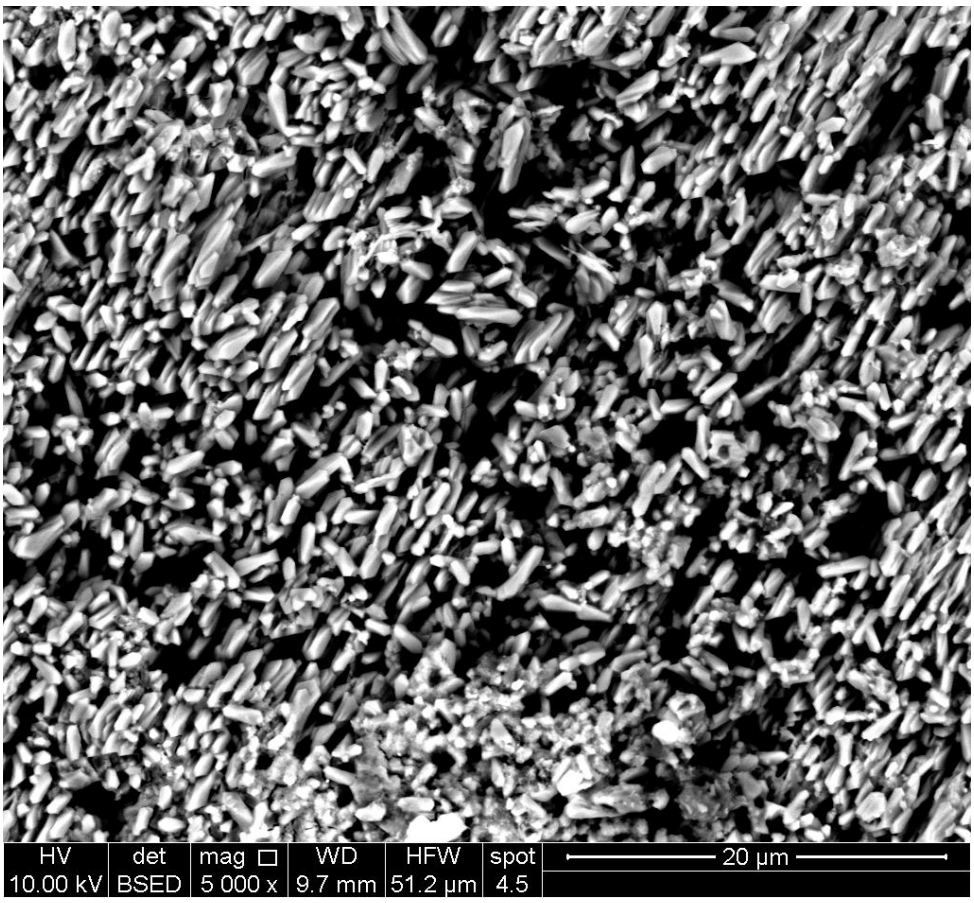

Figure 17) SEM image of euhedral calcium carbonate minerals within a partially dissolved region of calcium-rich matrix within the Amherstberg sample. 5,000x magnification.

X-RAY DIFFRACTION

XRD results listed in Table 2 report the mineral composition analysis of the Amherstberg at a depth of 3037.5 feet (926m). The Amherstberg sample contained major calcite and dolomite, and minor quartz and clay. Trace amounts of feldspar, pyrite, and anhydrite are present. XRD identified higher percentages of magnesium phases than reported by EDS experiments. While the results indicate the composition of the specific sample within the study, the overall composition of the Amherstberg formation is a complex undertaking considering the heterogenous nature of the entire formation. Table 2 values are consistent with the values discovered from SEM-EDS experiments.

Table 2) Mineral composition analysis of the Amherstberg sample at 3037.5 feet (926m).

Mineral Identified	Composition
Quartz	Minor (5%)
Calcite	Major (40%)
Dolomite	Major (44%)
Feldspar	Trace (4%)
Pyrite	Trace (1%)
Clay	Minor (7%)
Anhydrite	Minor (5%)

Major: > 25%, Minor: 5-25%, Trace: <5%
*error of mineral composition percentage is not known

ICP-OES

Table 3) Concentration of the cations/anions in the brine before and after exposure to limestone sample and CO_2

Cation/Anion	Before (mg/L)	After (mg/L)	Change (%)
Ca	71939.921	76109.921	5.797%
K	9918.000	10490.000	5.767%
Mg	10109.791	10449.791	3.363%
Na	22112.155	22932.155	3.708%
S	255.300	261.400	2.389%
Sr	2250.769	2357.769	4.754%
Cl	195970.437	209703.741	7.008%
Br	2987.753	2647.868	-11.376%

The concentration of cations and anions in the original brine, as well as in the brine after wet exposure were determined by ICP-OES and ion chromatography, and the results are reported in Table 3 for the Amherstberg sample. The measured changes include cations and anions that were reported well above lowermost detection limits to ensure experimental certainty.

Small changes in ionic compositions are observed for most of the ions within the brine. However more noticeable concentration changes are observed within calcium and chlorine ions. There is a decrease in calcium concentration within the brine, 3.401% while there is an observed increase of 6.466% of Cl^- anions. These findings reinforce calcium precipitation reactions noted in Figure 14. However, the increase of chlorine ions is unclear although it may indicate the reworking or breakdown of feldspar or clay minerals.

IMAGE ANALYSIS OF SURFICIAL POROSITY

200- and 5,000-times magnification SEM images were selected for this study. 200 times imagery could represent a large area with varying surficial geochemistry while also still being able to observe pore spaces without zooming in on the image. 5,000-times magnification imagery was selected for an enhanced look at pore shape and size. View Appendix B and C for images.

Results at the 200x magnification scale (Figures 19, 21, 23A) show that prior to any exposure the site surface porosities varied from 1.7% to 12%, with an average value of 5.626%. After dry exposure, porosities varied from 2.3% to 6.0%. It is to be noted that sites 3 and 4 trended similarly during these steps, while after dry exposure sites 1 and 5 produced similar porosity values after the wet reaction. Wet exposure porosity values ranged from 5.7% to 12.2% with an average porosity of 7.9%. The porosity estimates of the dry samples fit within the measured values of the experimentally determined porosity by Sminchak et al., 2009. Sminchak et al., 2009 recorded 7 porosity measurements using porosimeter along 59 meters (194 feet) of Amherstberg core plugs where porosities ranged from 1.5% to over 20% with an average porosity around 7% (Figure 18).

Sites 1 and 5 both contained regions where noticeable mesopores closed in regions but opened within others. Site 4, which experienced the largest overall porosity change contained the most limestone and dolostone matrix material and experienced the increase of meso- and macroporosity. In dry reactions such as the one in this experiment, porosity increases in this scale of porosity can be attributed to the plucking of dense minerals and reworking of other loose surface materials. The decrease in porosity at site 3

is most likely due to a localized precipitation of large (0.01-0.25mm) salt (NaCl, KCl) minerals within the surface.

Results at the 5,000x magnification scale (Figures 20, 22, 23B) show that prior to any exposure the sites had a wide range of porosity values, ranging from 14.4% to 20.6% with an average value of 11.7%. After dry exposure, porosities varied from 3.9% to 19.2%. with an average value of 8.5%. Wet exposure porosity values ranged from 11.2% to 27.8% with an average porosity of 17.5%. These porosity values range high compared to experimental values and must be used as a comparison tool between imaged site locations. When the SEM captures images at high resolutions, it is typically for

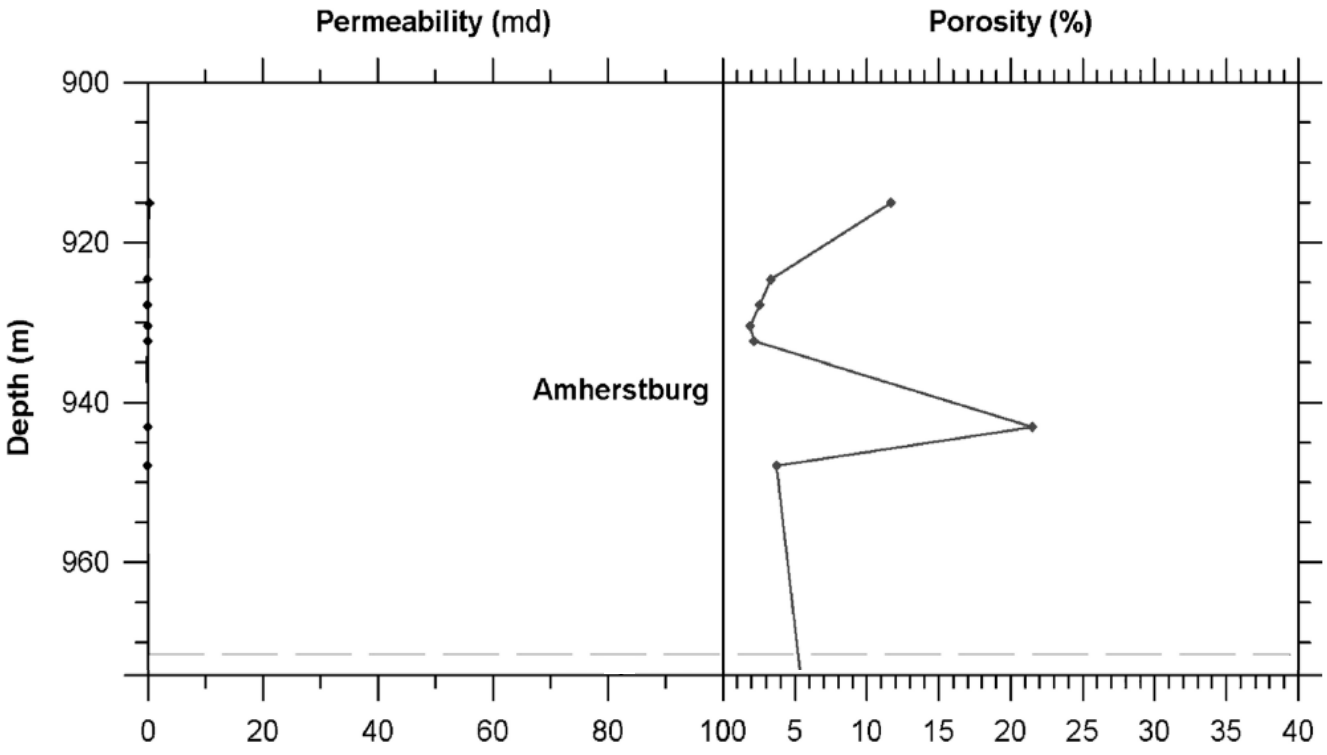

Figure 18) Permeability and Porosity measurements from State Charlton #4-30 well. Measurements were taken from the same core studied in this research. Porosity values range from 1.5% to over 20% and change with depth in the subsurface. This figure is modified from Sminchak et al., 2009.

inspection of features of interest and will display features at proportions not always representative of the actual bulk sample.

200x Magnification - 926 m (3,307.5 feet)			
	No Exposure	Dry Exposure	Wet Exposure
Site 1	12.828%	2.301%	8.208%
Site 2	5.611%	0.235%	4.546%
Site 3	1.725%	6.039%	5.732%
Site 4	1.740%	5.769%	12.210%
Site 5	6.224%	2.876%	8.961%

Figure 19) Porosity values from image analysis experiments. The values represent the porosities from 5 different sites within the Amherstberg sample and were measured prior to, and after exposure to CO_2 (Dry Exposure) and CO_2-saturated brine (Wet-Exposure).

5,000x Magnification – 926m (3,037.5 feet)			
	No Exposure	Dry Exposure	Wet Exposure
Site 1	12.410%	3.921%	11.240%
Site 2	7.949%	3.901%	N/A
Site 3	13.534%	8.913%	18.778%
Site 4	4.410%	6.825%	27.806%
Site 5	20.626%	19.219%	12.451%

Figure 20) Porosity values from image analysis experiments. The values represent the porosities from 5 different sites within the Amherstberg sample and were measured prior to, and after exposure to CO_2 (Dry Exposure) and CO_2-saturated brine (Wet-Exposure).

Sites 1 and 3 porosity trends paralleled each other before and after both exposure reactions. Both sites decreased in porosity surface area during the dry exposure reactions and increased in porosity after exposure to CO_2 and brine. Site 1 at 5,000x had a prominent pyrite framboid in the center, but the lower left portion of the image contained a calcium-rich region that encountered dissolution after the wet exposure reaction (Figure 16D). Site 3 was observed to precipitate $CaCO_3$ minerals over much of the sample surface but maintained mesoporosity within the mineral matting (Figure 17). Site 4 experienced increasing porosity trends at both scales (Figures 21, 22). At this location, the EDS data revealed a primarily calcitic surface prior to any exposure. However, prior to wet exposure, the site calcium values decreased in respect to magnesium-rich minerals and enlargement of pores. Site 5 was the only site to experience a porosity decrease at the 5,000x scale. This is likely attributed to the reworking of the matrix materials at this site. Pre- to dry-exposure images reveal a slight opening of pore spaces and surface etching, but dry- to wet-exposure images show the re-orientation of minerals within the sample.

The movement of minerals may be caused by pore filling precipitation activities or from the swelling or reworking of clay minerals.

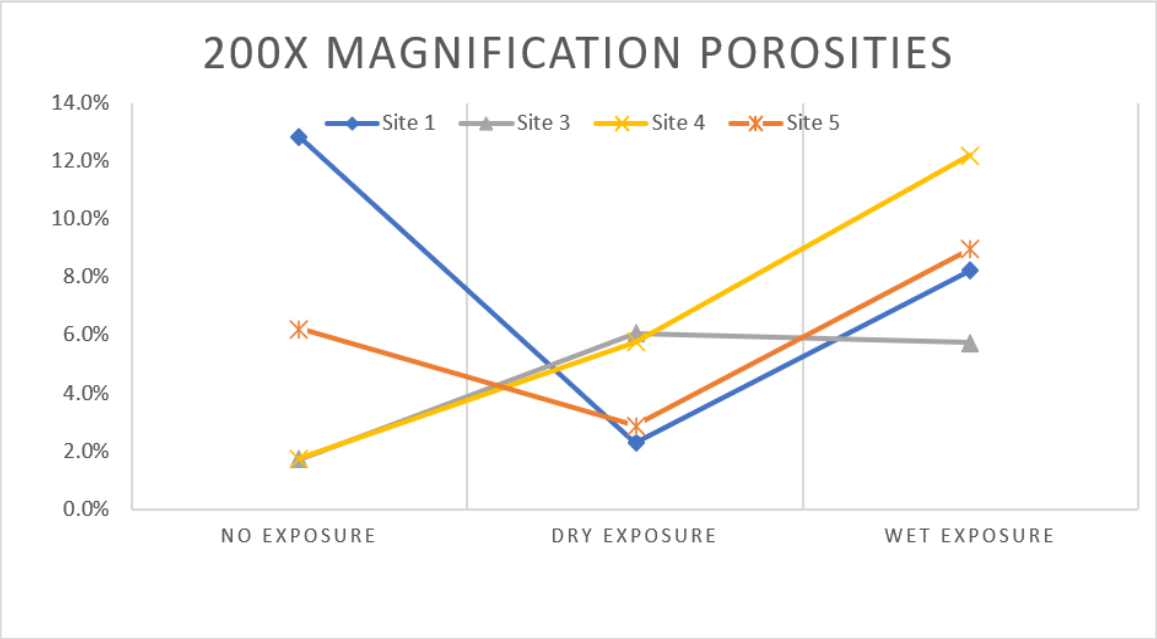

Figure 21) Porosity values calculated via image analysis. Results from Sites 1, 3, 4, and 5 from feature relocated, 200 times magnified Amherstberg SEM images are included.

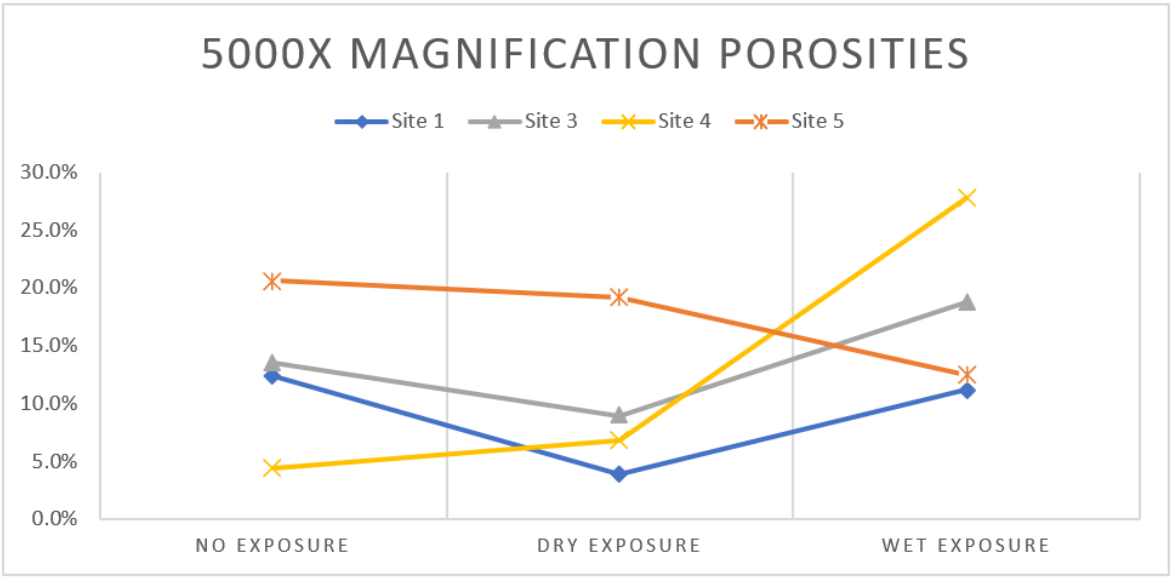

Figure 22) Porosity values calculated via image analysis. Results from Sites 1, 3, 4, and 5 from feature relocated, 5,000 times magnified Amherstberg SEM images are included in Figure 23.

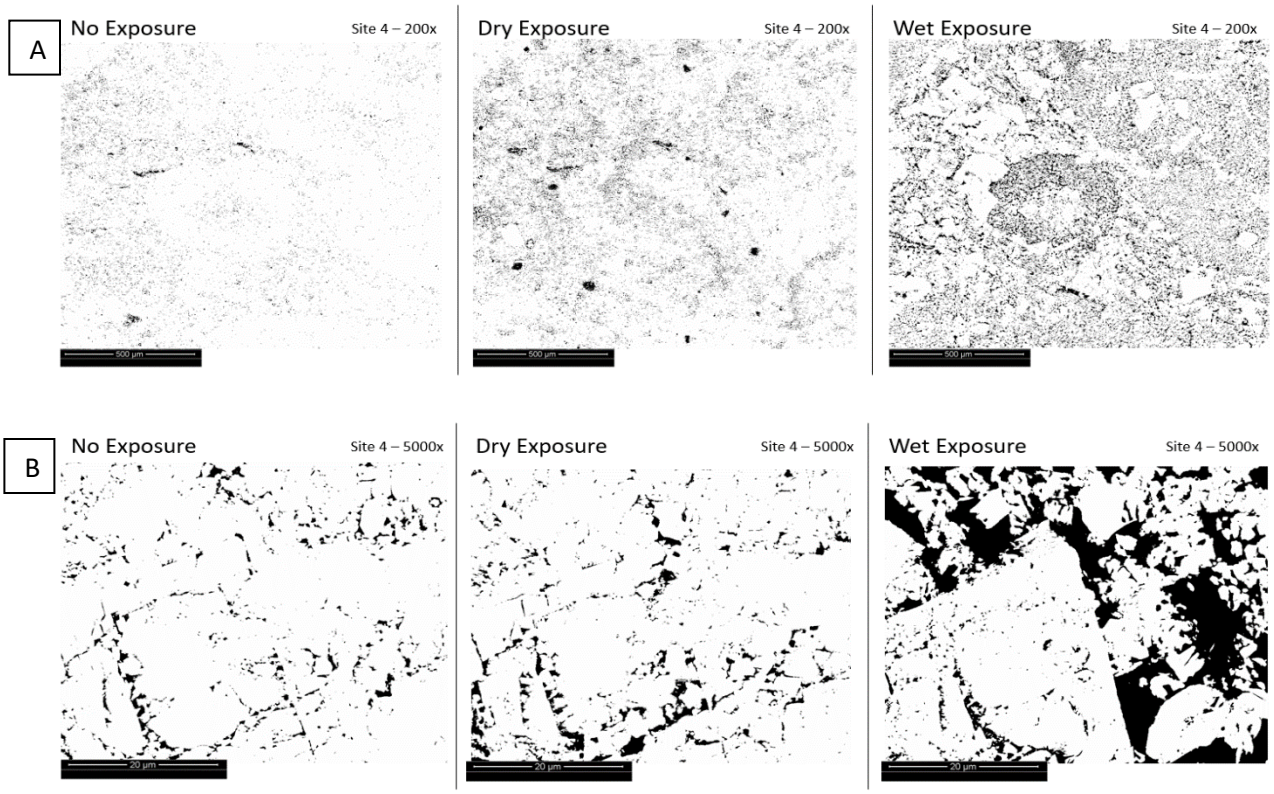

Figures 23A, 23B) Binary image comparisons for Site 4 of the Amherstberg limestone. A) Binary images at 200- times magnification. B) Binary images at 5,000- times magnification. The binary images are derived from SEM grayscale images which underwent image analysis to determine relative porosity. Images compare porosity (black pixels) within their matrices (white pixels) before and after exposure reaction testing.

CHAPTER V

DISCUSSION AND CONCLUSION

The observations and experimental results show that extensive reservoir characterization is necessary to understand and predict the impact of CO_2 injection on carbonates as top seals for carbon dioxide storage reservoirs. Geochemical experimentation and analyses returned varied results that do not clearly define the sealing abilities of the Amherstberg limestone.

The Amherstberg limestone possessed lithologic properties as mentioned in literature descriptions; dolomitic, cherty, minor shale and fossiliferous (Gardner, 1974). EDS and XRD data revealed that the samples contained between 30% and 40% (by weight) calcium and calcite phases, 44% (by weight) dolomite.

Reactions to CO_2 alone revealed slight geomorphic surface changes to the Amherstberg. Changes to the mineralogy likely did not occur due to poor reactivity with dry CO_2 and no aqueous phase to assist the adherence and interaction of brine to the sample surface. However, dry CO_2 does influence the evolution of porosity within the sample.

CO_2 does react with calcium-rich phases in the presence of water. Sanguinito et al. (2018) and Goodman et al. (2019) identified CO_2-brine reactions localizing on calcite matrices of carbonate-rich Utica shale after undergoing a similar set of CO_2 sequestration reactions. Calcite regions of the Utica shale were highly affected whereas more resistant minerals such as quartz and magnesium-rich grains were unaffected/unreacted. These findings have been consistent with the majority of experiments regarding carbon storage within sedimentary reservoirs (Johnson et al., 2001; Mehnert et al., 2014; Sanguinito et al., 2017; Shi et al., 2019, etc.). The Amherstberg experimental results continued to show similar results where pyrite and dolomite appeared largely unaffected.

Visual-based surface porosity estimates ranging between 1.7% and 12.8% indicate that the Amherstberg limestone reactions are affected by its heterogeneous nature. SEM images show regions of dissolution and precipitation leading to the increase in size of mesopores at the surface of the samples. Images also tend to show that calcium-dense regions are the most likely to dissolve within the matrix whereas magnesium-dense minerals were more likely withstand CO_2-saturated brine exposure. This suggests that regions of the Amherstberg with higher ratios of dolomitic lithology may better withstand brine containing dissolved CO_2. Increase of pores could potentially enhance permeability within the formation leading to the eventual upward migration of carbon dioxide through the cap rock. Alternatively, the expansion of pores may also create extra surface area for carbonate mineralization and provide additional CO_2 mineral trapping opportunity. Goodman et al., 2019 argues that microporosity within the carbonate-rich Utica shale will close after interacting with CO_2-saturated brine at reservoir conditions. Tutolo et al., 2015 determined that permeability within carbonate- and feldspar-rich sandstones decreased by

nearly a third after exposure to CO_2-saturated brine and that secondary mineralization preferred to precipitate on pitted mineral surfaces. Scholle, 1979 identified the complex nature of porosity prediction within shallow-water carbonates such as the Amherstberg because of the inclusion of unstable minerals like aragonite and anhydrite. Scholle argues that small differences in burial and uplift water chemistry may produce drastically different trends of porosity preservation, and pore fluids tend to alter susceptible minerals within carbonates during burial. Overall, a more dynamic long-term experiment with multiphase flow-through tests and computerized tomography would provide better insight on the permeability of the Amherstberg by imaging the internal pore-size distribution and pore throat evolution, further aiding in the identification of geochemical changes that could serve to a carbonate cap rock's benefit or detriment.

Salt precipitation on and within the sample surface is likely to lead to larger scale formation damage. On the surface, salt-wedging is an erosional/weathering process where the precipitation of salt from solution due to environmental changes surrounding a rock specimen widens pre-existing gaps and fractures leading to the creation of more surface area of the rock. In the subsurface, excess mineral precipitation and widening of fractures within pores and grains may cause fluid migration pathways or even induce micro-seismicity by means of mechanical weakening at the reservoir scale. Both Shi et al., 2019 and Dávila et al., 2020 identified dissolution and precipitation of salts from CO_2-saturated brine injections as a mechanism for the decrease of mechanical strength in the Mt Simon sandstone. Salt precipitation and dissolution was also observed in the analyses of this thesis. Because of the compositional differences, including pore networks, between sandstones, shales, and carbonates, it is not necessarily certain that this phenomenon

occurs within all reservoir types, but additional work should be performed to determine if salt precipitation affects carbonates or even shales to a lesser degree.

In summary, the interactions of CO_2 and synthesized brine with Amherstberg samples were investigated with feature relocation SEM-EDS, XRD, ICP-OES, and surface pore estimation analysis techniques at 31.5C and CO_2 pressure of 13.8MPa for 14 days. Carbonate dissolution and precipitation reactions were predominantly observed in SEM imagery and ICP-OES data. Dry CO_2 reactions produced minor surficial changes at select sites but significant surficial damage occurred at all five sites when the Amherstberg interacted with CO_2-saturated brine. The changes in carbonate chemistry resulted in etching and pitting of the samples as well as evolution of mesoporosity observed with both SEM and porosity estimation. These alterations in the Amherstberg have the potential to modify flow pathways in carbonate formations that may negatively affect long term integrity of carbon storage.

The heterogeneity of the limestone in terms of mineralogy, brine content, and pore scale variability produces conflicting results. On one hand, mineral precipitation may provide positive effects on the sealing capabilities of the Amherstberg when mineralization occurs on and within pores. Observations of the limestone indicated that pores appear to close at the surface providing additional impermeability as a seal. The swelling of clay minerals also may provide similar assurances to the impermeability of the Amherstberg. On the other hand, negative effects of mineral dissolution and surface alteration of the Amherstberg may provide migration pathways for CO_2 to penetrate through the rock, decreasing overall sealing ability. Ultimately, more research is needed to understand the internal pore networks of the Amherstberg and how it may vary with

depth. Porosity and permeability are key parameters to controlling flow in the subsurface, and the alteration of pore networks may affect transport and flow properties of the limestone. If the in-situ formation brine penetrates the Amherstberg deeply and affects the internal pore network and mineralogy as observed on the surface, then the Amherstberg may not provide assurance needed from a CO_2 reservoir cap rock. Thus, porosimetry and permeability experiments performed before and after exposure reactions would complement the results of this study. Overall, the results of this research intend to act as an important step to identifying how carbonate cap rocks may serve as a reservoir seal.

The quality of carbon storage permanence is one of the most critical factors affecting CCUS reservoir exploration in the Michigan Basin to safeguard continued economic growth and security throughout the Midwestern United States. The effectiveness of carbon dioxide storage cap rocks, to successfully seal the reservoir, is perhaps the most important factor for long-term storage.

REFERENCES

Bachu, S., 2000, Sequestration of CO_2 in Geological Media: Criteria And Approach For Site Selection In Response To Climate Change: Energy Conversion and Management, v. 41, no. 9, p. 953-970. https://doi.org/10.1016/S0196-8904(99)00149-1

Barnes, D. A., W. B. Harrison, and A. Wahr, 2009, Assessment of Regional Geological Carbon Sequestration Potential in Upper Silurian to Middle Devonian Strata of the Michigan Basin: AAPG Studies in Geology, v. 59, p. 99–123, doi:10.1306/13171236St593379.

Bohnhoff, M., M. D. Zoback, L. Chiaramonte, J. L. Gerst, and N. Gupta, 2010, Seismic Detection of CO2 Leakage Along Monitoring Wellbores: International Journal of Greenhouse Gas Control, v. 4, no. 4, p. 687–697, doi:10.1016/j.ijggc.2010.01.009.

Bowen, B. B., R. I. Ochoa, N. D. Wilkens, J. Brophy, T. R. Lovell, N. Fischietto, C. R. Medina, and J. A. Rupp, 2011, Depositional and Diagenetic Variability within the Cambrian Mount Simon Sandstone: Implications for Carbon Dioxide Sequestration: 2Environmental Geosciences, v. 18, no. 2, p. 69–89, doi:10.1306/eg.07271010012.

Dávila, G., L. Dalton, D. M. Crandall, C. Garing, C. J. Werth, and J. L. Druhan, 2020, Reactive alteration of a Mt. Simon Sandstone due to CO2-rich brine displacement: Geochimica et Cosmochimica Acta, v. 271, p. 227–247, doi:10.1016/j.gca.2019.12.015.

Davis, S. J., G. P. Peters, and K. Caldeira, 2011, The Supply Chain of CO2 Emissions: Proceedings of the National Academy of Sciences of the United States of America, v. 108, no. 45, p. 18554–18559, doi:10.1073/pnas.1107409108.

Fang, Y., B. Baojun, T. Dazhen, S. Dunn-Norman, and D. Wronkiewicz, 2010, Characteristics of CO2 Sequestration in Saline Aquifers: Petroleum Science, v. 7, no. 1, p. 83–92, doi:10.1007/s12182-010-0010-3.

George W. Pirtle, 2003, Michigan Structural Basin and Its Relationship to Surrounding Areas: AAPG Bulletin, v. 16, no. 2, p. 145–152, doi:10.1306/3d932a4e-16b1-11d7-8645000102c1865d.

Goodman, A., S. Sanguinito, B. Kutchko, S. Natesakhawat, P. Cvetic, and A. J. Allen, 2020, Shale pore alteration: Potential implications for hydrocarbon extraction and CO2 storage: Fuel, v. 265, no. October 2019, p. 116930, doi:10.1016/j.fuel.2019.116930.

Goodman, A., S. Sanguinito, M. Tkach, S. Natesakhawat, B. Kutchko, J. Fazio, and P. Cvetic, 2019, Investigating the role of water on CO2-Utica Shale interactions for carbon storage and shale gas extraction activities – Evidence for pore scale alterations: Fuel, v. 242, no. September 2018, p. 744–755, doi:10.1016/j.fuel.2019.01.091.

Harrison, W. B., G. M. Grammer, and D. A. Barnes, 2009, Reservoir characteristics of the Bass Islands dolomite in Otsego County, Michigan: Results for a Saline Reservoir, CO2 Sequestration Demonstration: Environmental Geosciences, v. 16, no. 3, p. 139–151, doi:10.1306/eg.05080909011.

Howell, P. D., and B. A. Van Der Pluijm, 1990, Early history of the Michigan Basin: subsidence and Appalachian tectonics: Geology, v. 18, no. 12, p. 1195–1198, doi:10.1130/0091-7613(1990)018<1195:EHOTMB>2.3.CO;2.

Johnson, J. W., J. J. Nitao, C. I. Steefel, and K. G. Knauss, 2001, Reactive transport modeling of geologic CO2 sequestration in saline aquifers: the influence of intra-aquifer shales and the relative effectiveness of structural, solubility, and mineral trapping during prograde and retrograde sequestration: First National Conference on Carbon Sequestration, p. 60.

Kutchko, B. G. et al., 2013, Computed Tomography and Statistical Analysis of Bubble Size Distributions in Atmospheric-Generated Foamed Cement: USDOE Technical Report Series, no. August, p. 28.

Kutchko, B., S. Sanguinito, S. Natesakhawat, P. Cvetic, J. T. Culp, and A. Goodman, 2020, Quantifying pore scale and matrix interactions of SCCO2 with the Marcellus shale: Fuel, v. 266, no. May 2019, p. 116928, doi:10.1016/j.fuel.2019.116928.

Lu, P., Q. Fu, W. E. Seyfried, A. Hereford, and C. Zhu, 2011, Navajo Sandstone-brine-CO2 interaction: Implications for geological carbon sequestration: Environmental Earth Sciences, v. 62, no. 1, p. 101–118, doi:10.1007/s12665-010-0501-y.

Matter, J. M. et al., 2011, The CarbFix Pilot Project - Storing carbon dioxide in basalt: Energy Procedia, v. 4, p. 5579–5585, doi:10.1016/j.egypro.2011.02.546.

Mehnert, E., J. Damico, S. Frailey, H. Leetaru, R. Okwen, B. Storsved, and A. Valocchi, 2014, Basin-scale modeling for CO2 sequestration in the basal sandstone reservoir of the Illinois Basin-improving the geologic model: Energy Procedia, v. 63, p. 2949–2960, doi:10.1016/j.egypro.2014.11.317.

Newcombe, R. B., 1932, Structure and Accumulation in the Michigan "Basin" and Its Relation to the Cincinnati Arch: Part IV. Relations of Petroleum Accumulation to Structure: 531–555 p.

Quinlan, G., 1990, Models of Subsidence Mechanisms in Intracratonic Basins, and Their Applicability to North American Examples: Canadian Society of Petroleum Geologists, v. 12, no. 1987, p. 463–48.

Raupach, M. R., G. Marland, P. Ciais, C. Le Quéré, J. G. Canadell, G. Klepper, and C. B. Field, 2007, Global and regional drivers of accelerating CO2 emissions: Proceedings of the National Academy of Sciences of the United States of America, v. 104, no. 24, p. 10288–10293, doi:10.1073/pnas.0700609104.

Rodwan, J. C., 1986, Stratigraphic and Sedimentologic Analysis of the Middle Devonian Filer Sandstone (Michigan Basin): Western Michigan Basin, 109 p.

Saeedi, A., R. Rezaee, and B. Evans, 2012, Experimental study of the effect of variation in in-situ stress on capillary residual trapping during CO 2 geo-sequestration in sandstone reservoirs: Geofluids, v. 12, no. 3, p. 228–235, doi:10.1111/j.1468-8123.2012.00364.x.

Sanguinito, S., A. L. Goodman, B. G. Kutchko, M. Tkach, S. Natesakhawat, D. Crandall, J. Fazio, and I. Fukai, 2017, Characterizing the Geochemistry of the CO<inf>2</inf>-Fluid-Shale Interface using In-Situ Infrared Spectroscopy and Feature Relocation Scanning Electron Microscopy, *in* 34th Annual International Pittsburgh Coal Conference: Coal - Energy, Environment and Sustainable Development, PCC 2017.

Sanguinito, S., A. Goodman, M. Tkach, B. Kutchko, J. Culp, S. Natesakhawat, J. Fazio, I. Fukai, and D. Crandall, 2018, Quantifying dry supercritical CO2-induced changes of the Utica Shale: Fuel, v. 226, doi:10.1016/j.fuel.2018.03.156.

Scholle, P. A., 1979, Porosity Prediction in Shallow vs . Deepwater Limestones, *in* Journal of Petroleum Science and Engineering: p. 2236–2242.

Shi, Z., L. Sun, I. Haljasmaa, W. Harbert, S. Sanguinito, M. Tkach, A. Goodman, T. T. Tsotsis, and K. Jessen, 2019, Impact of Brine/CO2 exposure on the transport and mechanical properties of the Mt Simon sandstone: Journal of Petroleum Science and Engineering, v. 177, no. May 2018, p. 295–305, doi:10.1016/j.petrol.2019.01.112.

Sloss, L. L., 1962, Stratigraphic Models in Exploration: Journal of Sedimentary Petrology, v. 32, no. 3, p. 415–422.

Sloss, L. L., 1982, The Michigan Basin: University of Missouri at Rolla, v. 1982b, no. 3, p. 25–29.

Sminchak, J., N. Gupta, and J. Gerst, 2009, Well Test Results and Reservoir Performance for a Carbon Dioxide Injection Test in the Bass Islands Dolomite in the Michigan Basin: Environmental Geosciences, v. 16, no. 3, p. 153–162, doi:10.1306/eg.04080909001.

Stanford, B. V., 1967, Devonian of Ontario and Michigan: Canadian Society of Petroleum Geologists, v. 1, p. 973–999.

Tutolo, B. M., A. J. Luhmann, X. Z. Kong, M. O. Saar, and W. E. Seyfried, 2015, CO<inf>2</inf> sequestration in feldspar-rich sandstone: Coupled evolution of fluid chemistry, mineral reaction rates, and hydrogeochemical properties: Geochimica et Cosmochimica Acta, v. 160, p. 132–154, doi:10.1016/j.gca.2015.04.002.

U.S. Geological Survey, 2013, National Assessment of Geologic Carbon Dioxide Storage Resources — Results: U.S. Geological Survey Circular 1386: 41 p.

US Department of Energy, and NETL, 2015, The US 2012 Carbon Utilization and Storage Atlas: 130 p.

Wigand, M., J. W. Carey, H. Schütt, E. Spangenberg, and J. Erzinger, 2008, Geochemical effects of CO2 sequestration in sandstones under simulated in situ conditions of deep saline aquifers: Applied Geochemistry, v. 23, no. 9, p. 2735–2745, doi:10.1016/j.apgeochem.2008.06.006.

Wood, J. R., and W. B. Harrison, 2002, Advanced Characterization of Fractured Reservoirs in Carbonate Rocks: The Michigan Basin: 1–54 p.

Zhou, J., S. Xie, Y. Jiang, X. Xian, Q. Liu, Z. Lu, and Q. Lyu, 2018, Influence of Supercritical CO2 Exposure on CH4 and CO2 Adsorption Behaviors of Shale: Implications for CO2 Sequestration: Energy and Fuels, v. 32, no. 5, p. 6073–6089, doi:10.1021/acs.energyfuels.8b00551.

APPENDICES

APPENDIX A

SEM Montage Image of Sample with Site Locations

Approximately 3,000 BSED SEM images of the sample surface, taken by the author at NETL-Pittsburgh, using FEI Quanta 600 Scanning Electron Microscope.

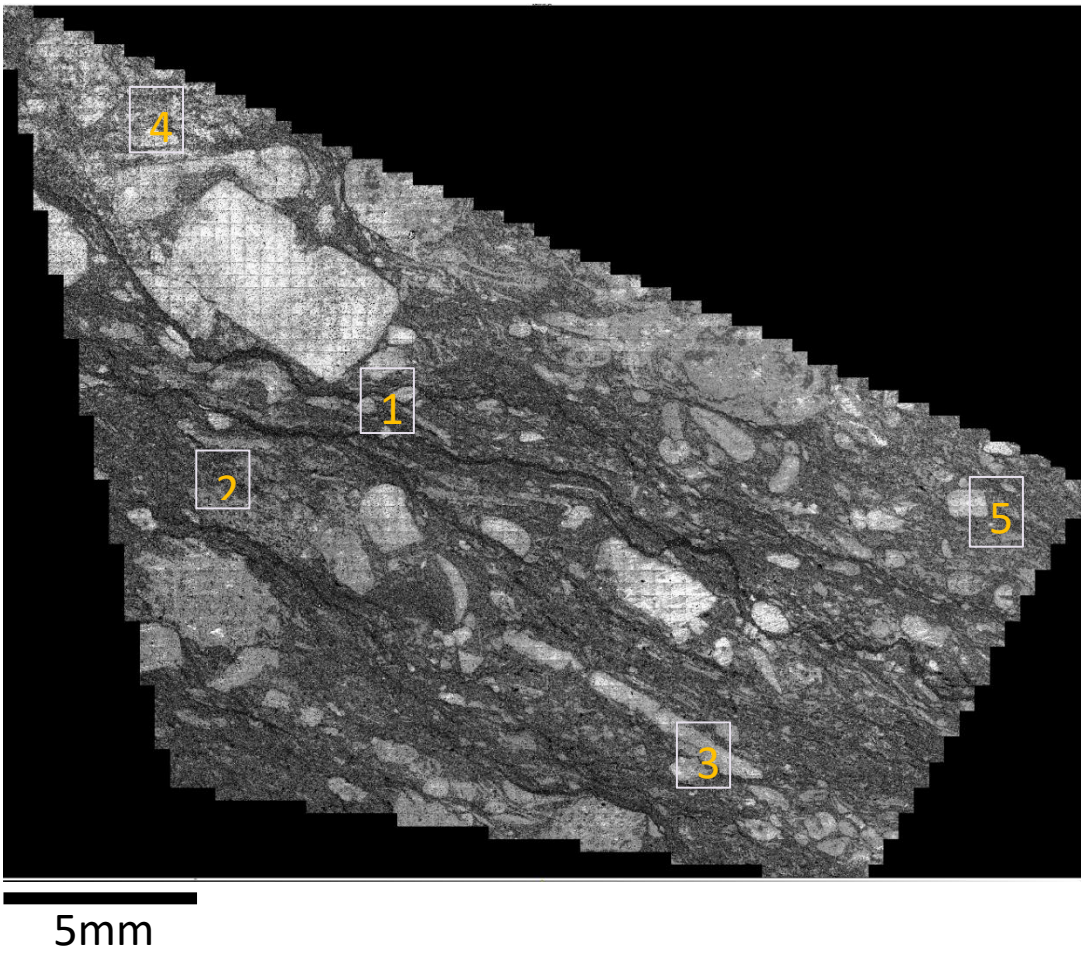

APPENDIX B

Site 1 SEM – BSED Images, Non-Exposed 100x-5000x

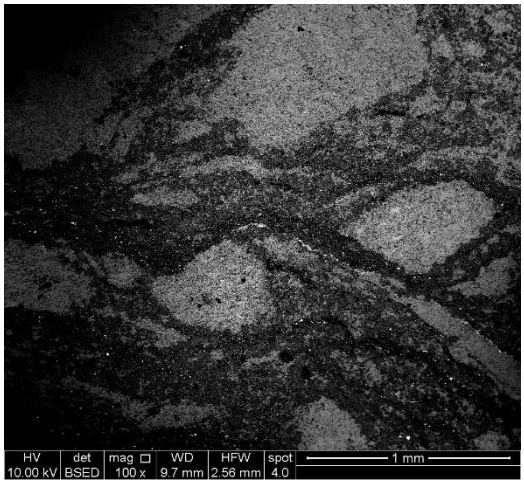

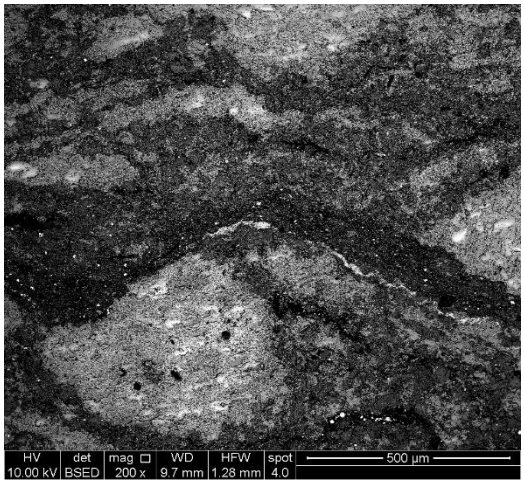

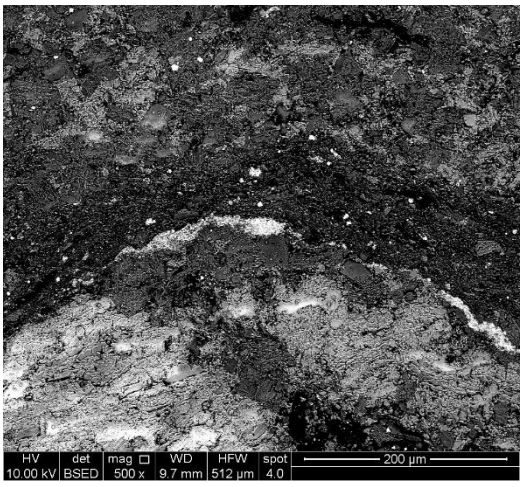

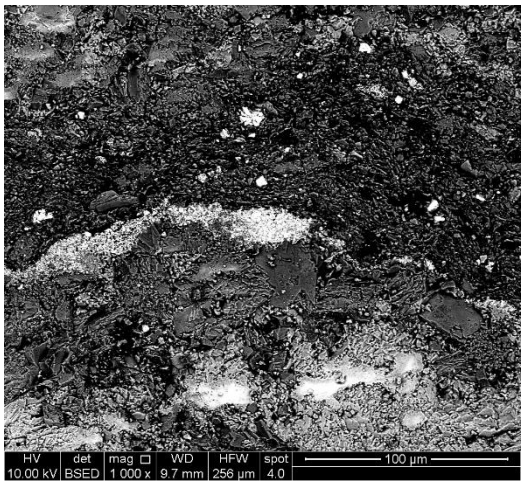

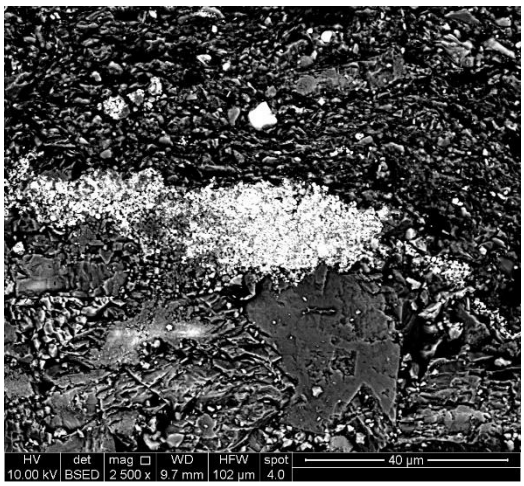

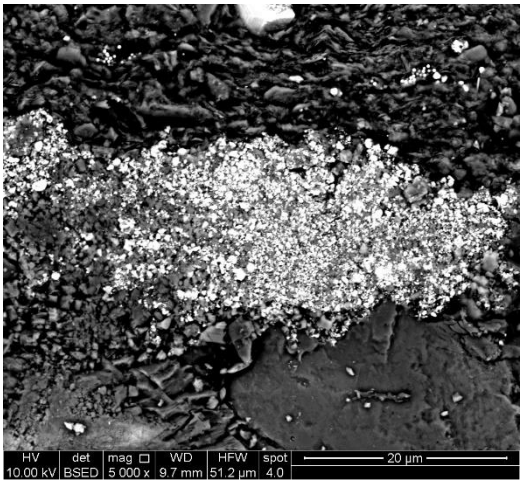

Site 1 SEM – BSED Images, Dry-Exposed 100x-5000x

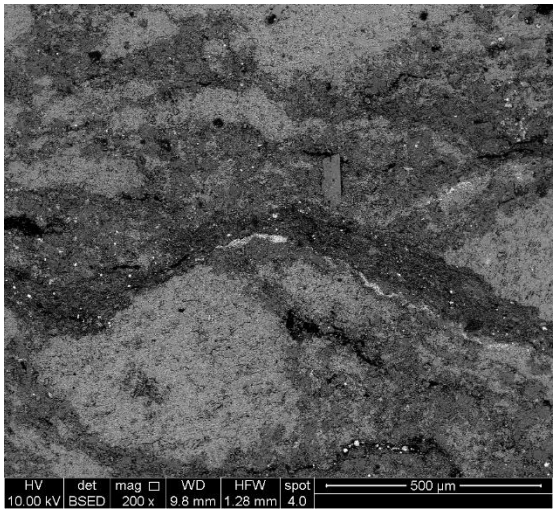

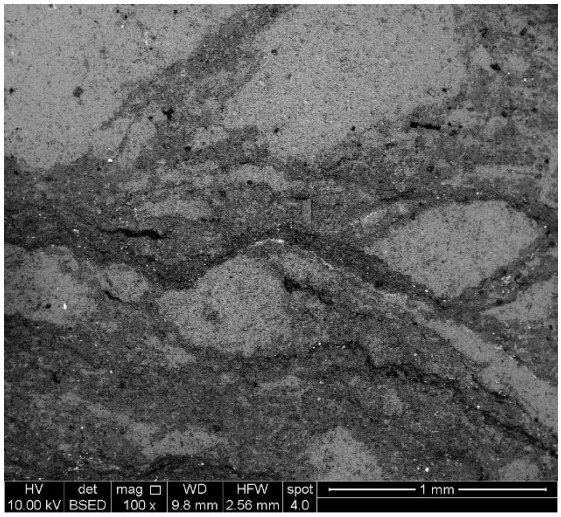

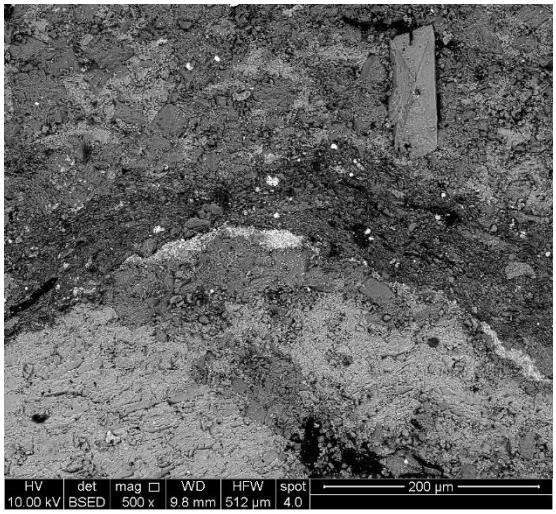

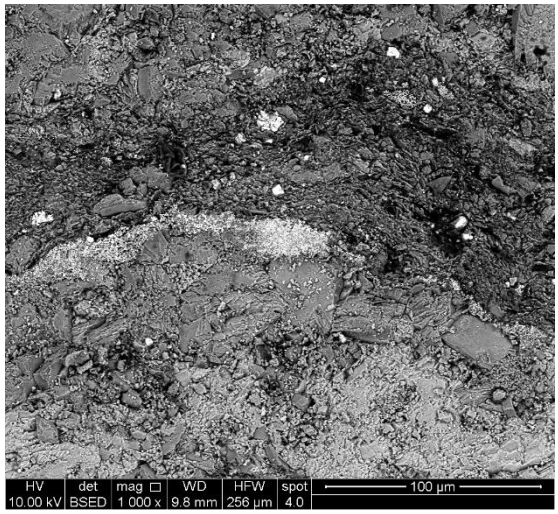

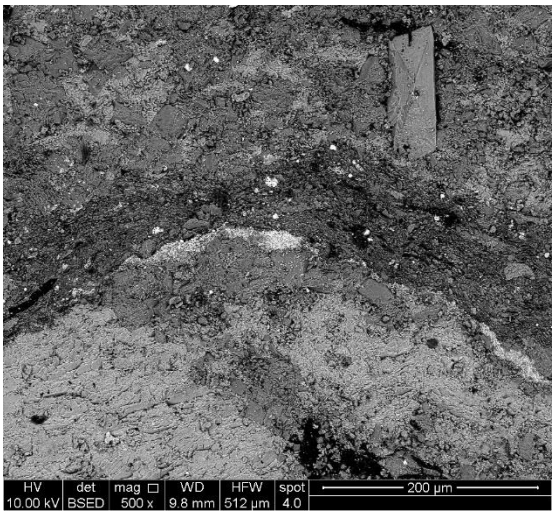

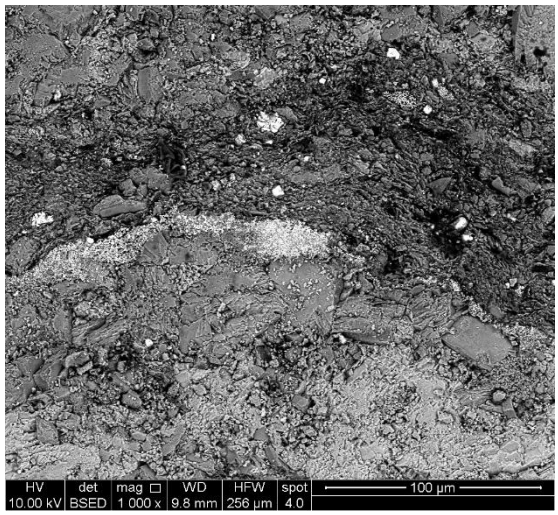

Site 1 SEM – BSED Images, Wet-Exposed 100x-5000x

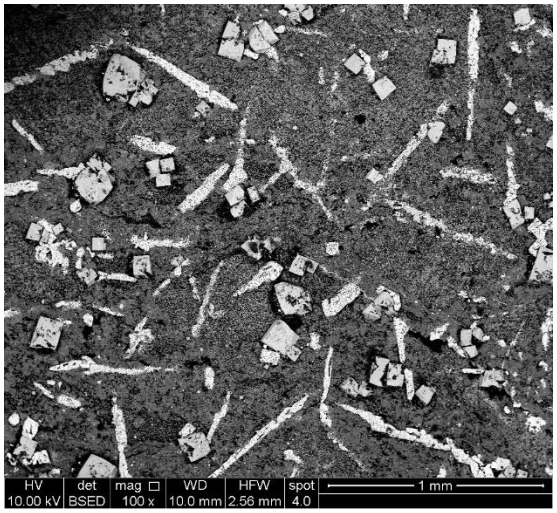

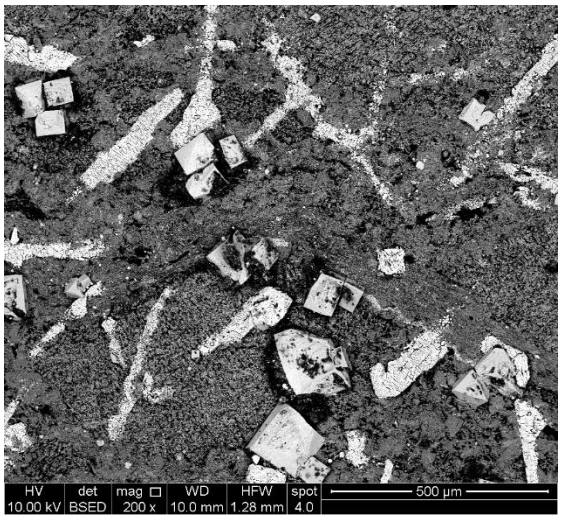

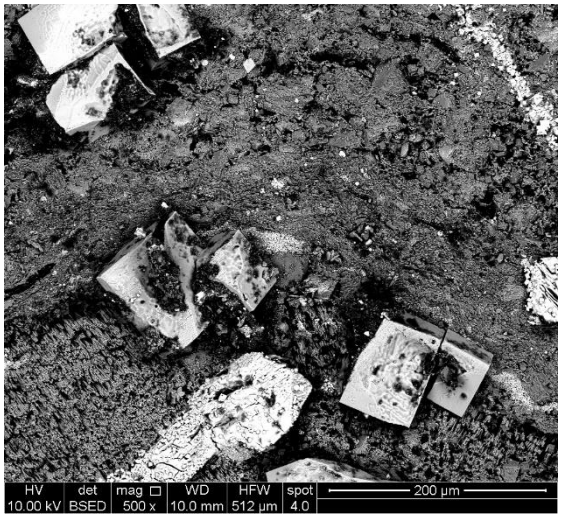

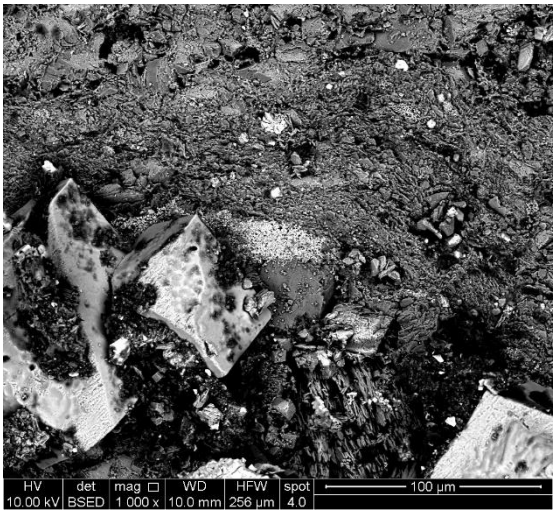

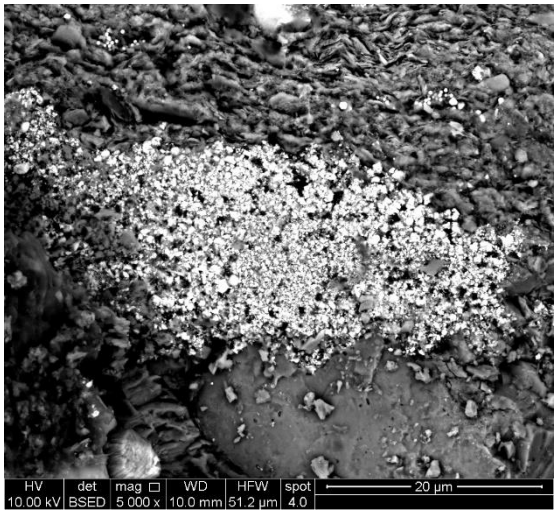

Site 2 SEM – BSED Images, Non-Exposed 100x-5000x

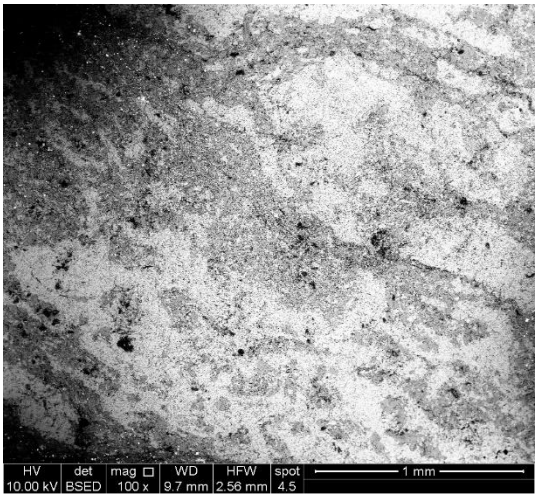

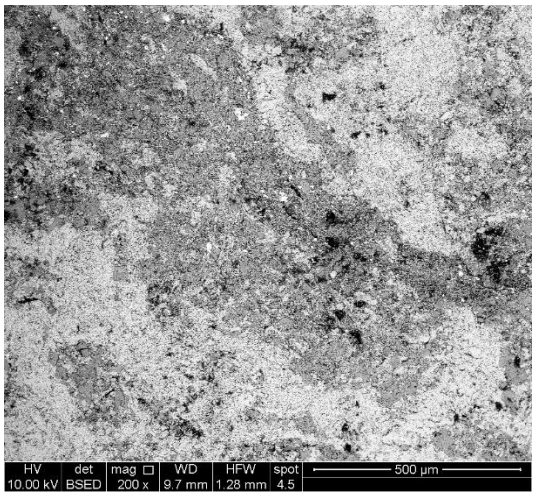

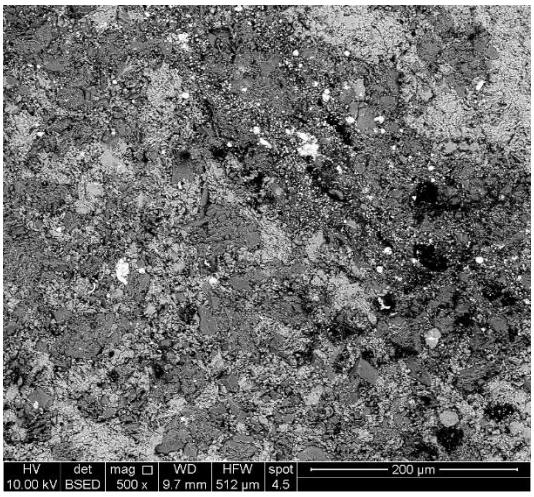

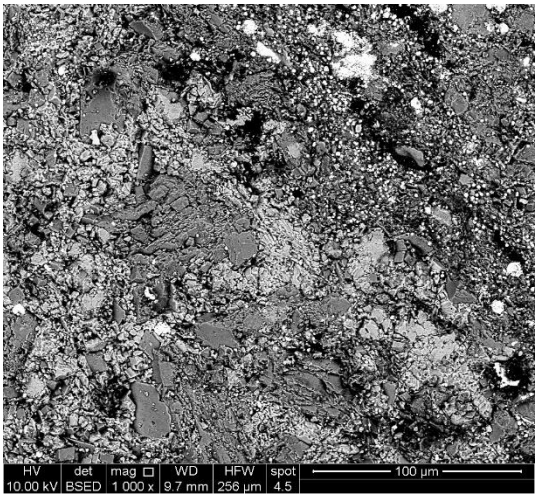

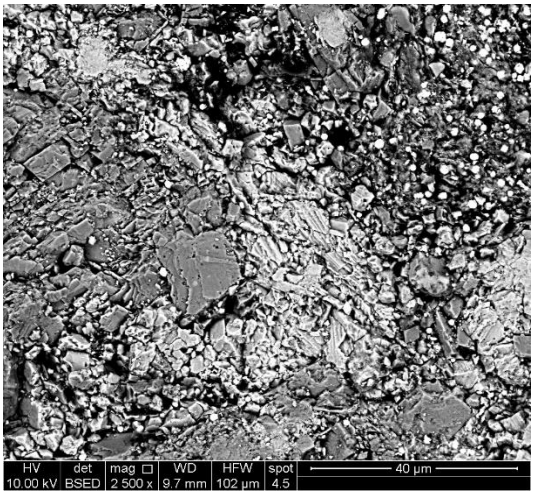

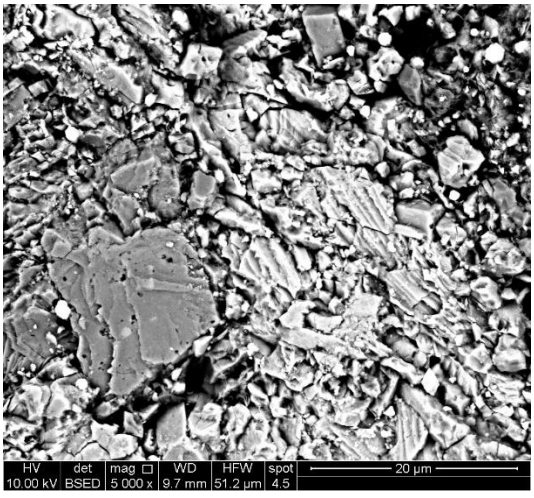

Site 2 SEM – BSED Images, Dry-Exposed 100x-5000x

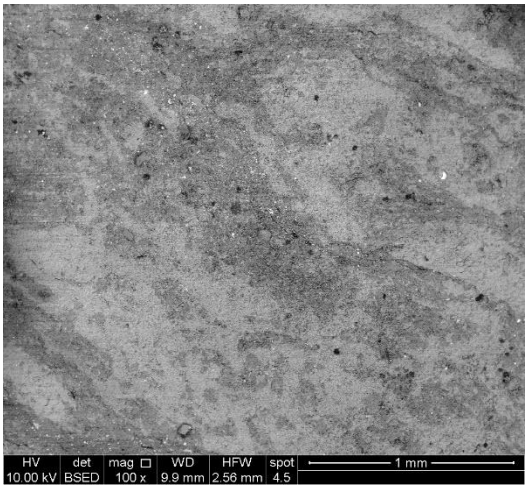

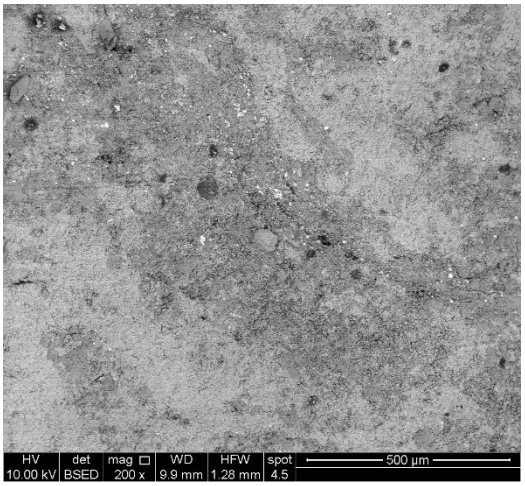

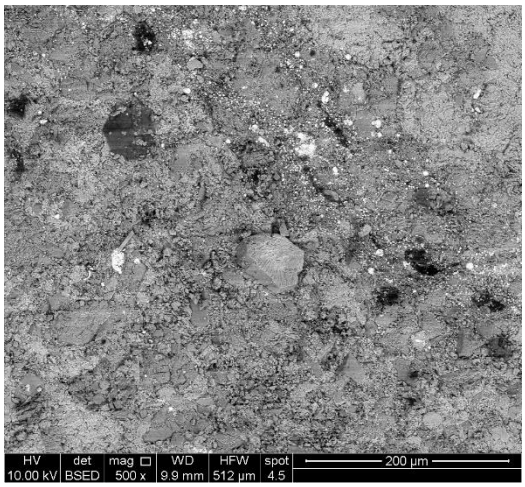

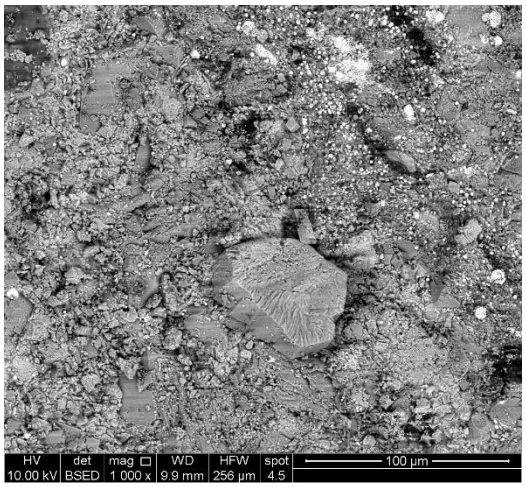

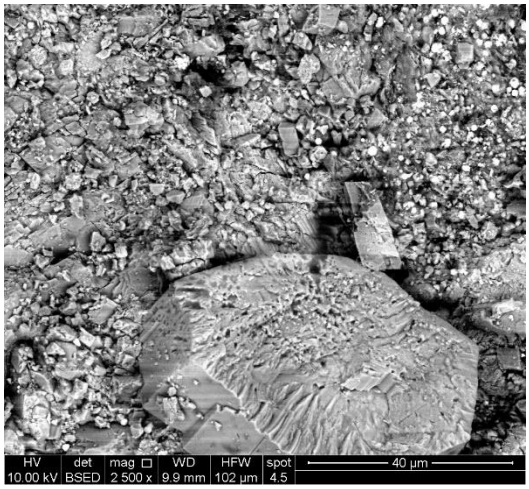

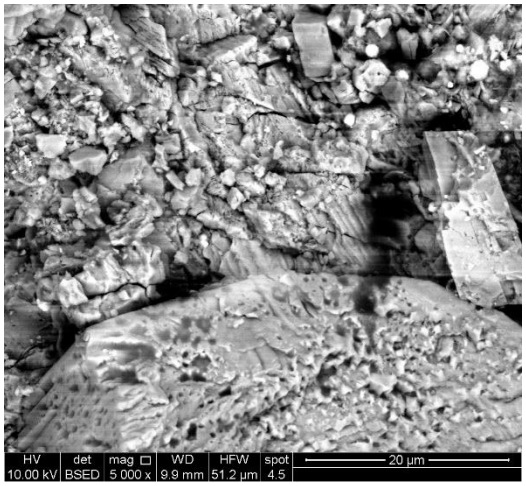

Site 2 SEM – BSED Images, Wet-Exposed 100x-5000x

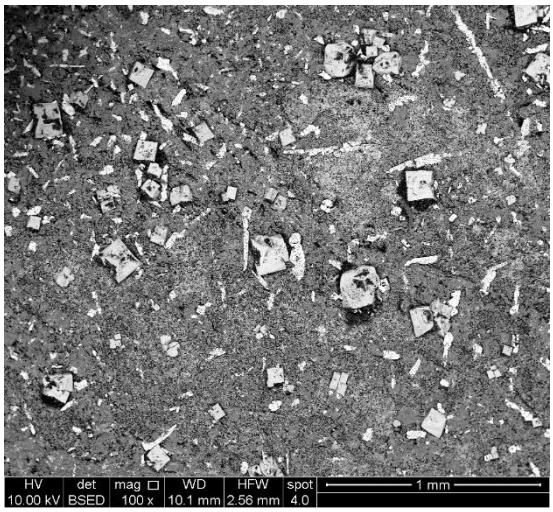

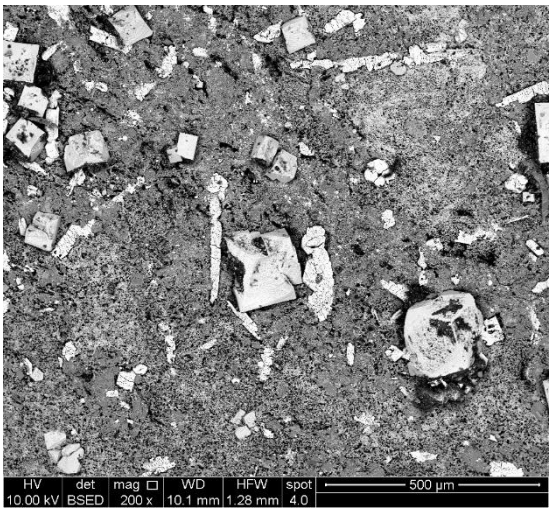

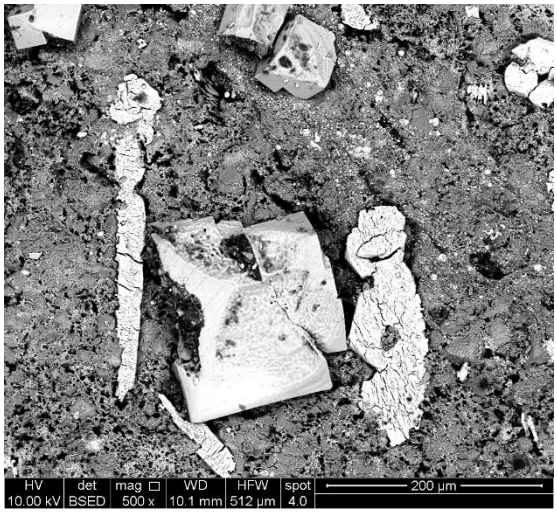

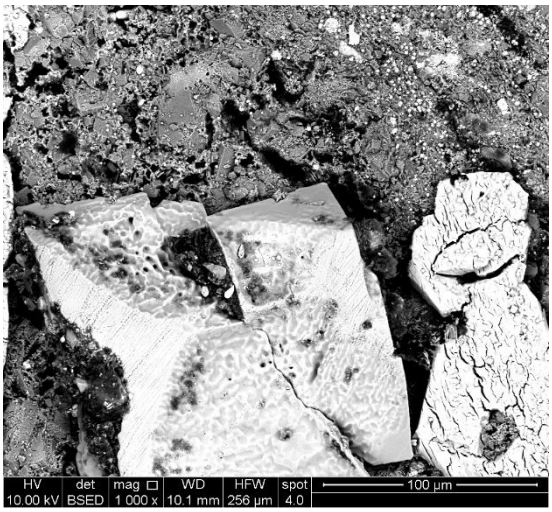

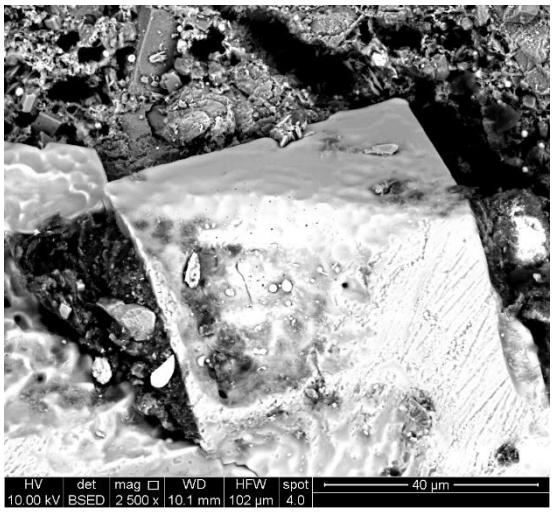

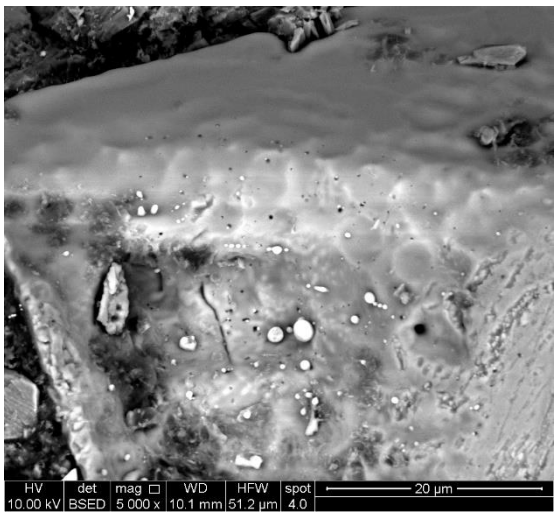

Site 3 SEM – BSED Images, Non-Exposed 100x-5000x

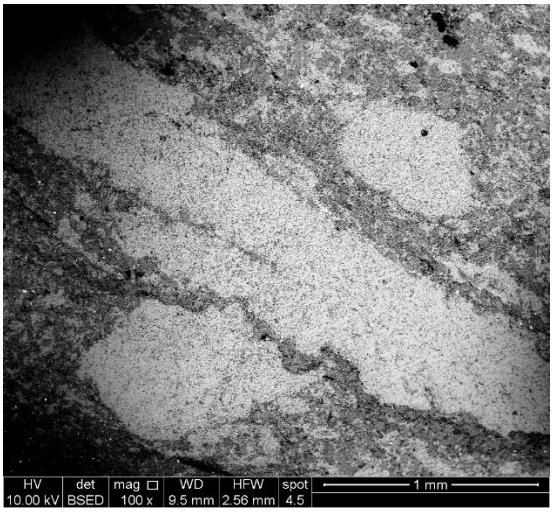

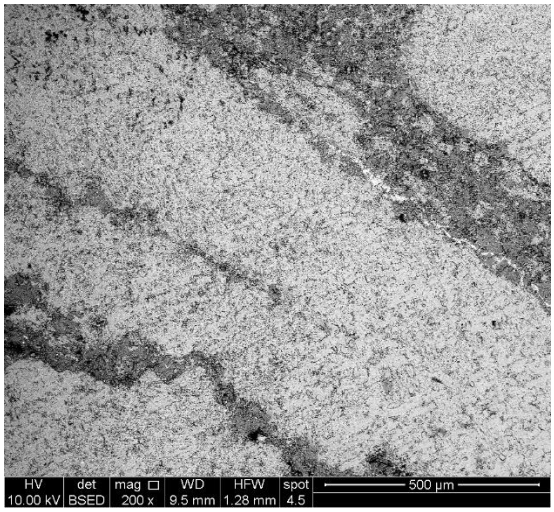

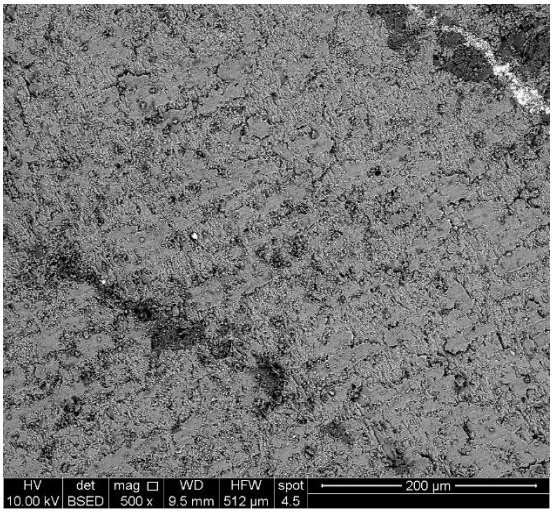

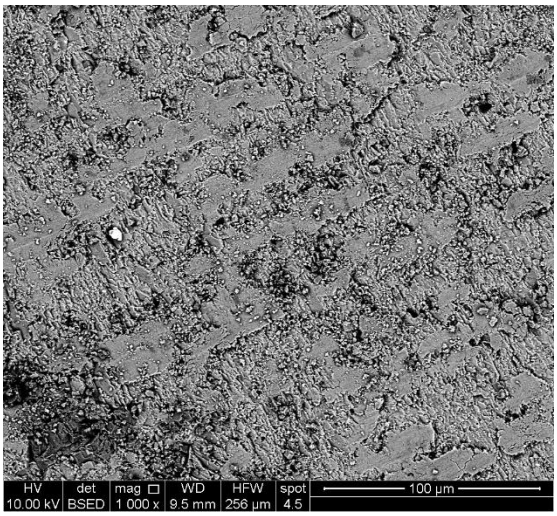

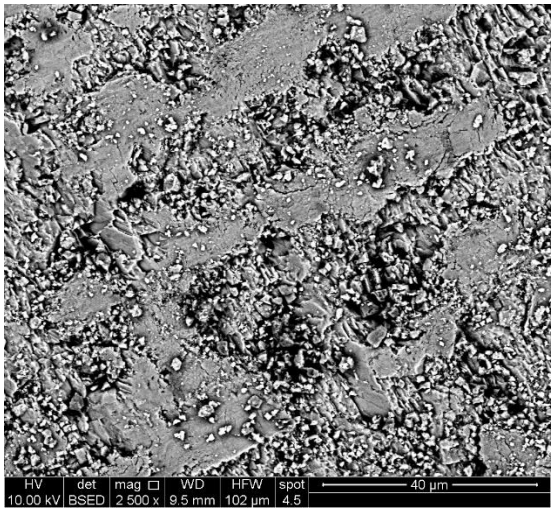

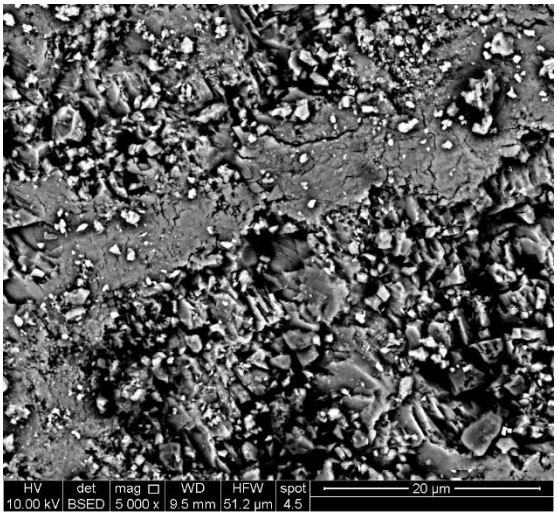

Site 3 SEM – BSED Images, Dry-Exposed 100x-5000x

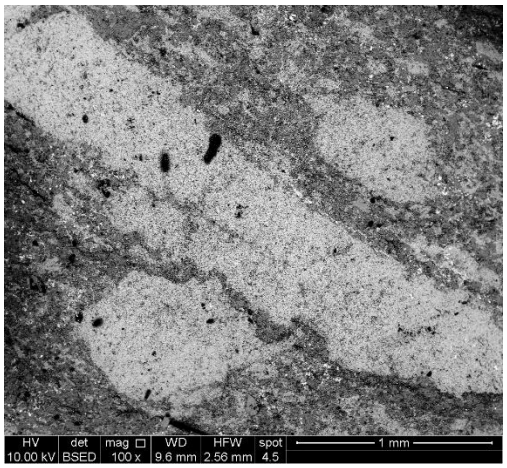

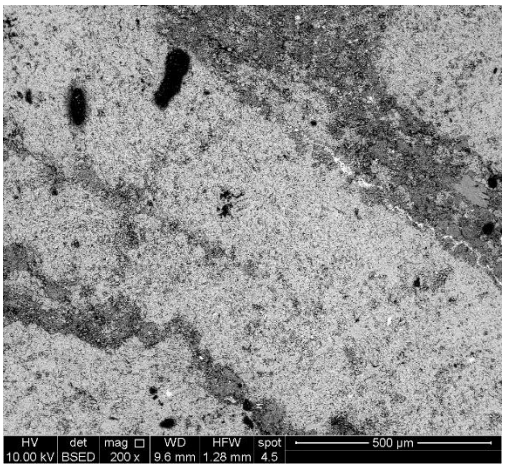

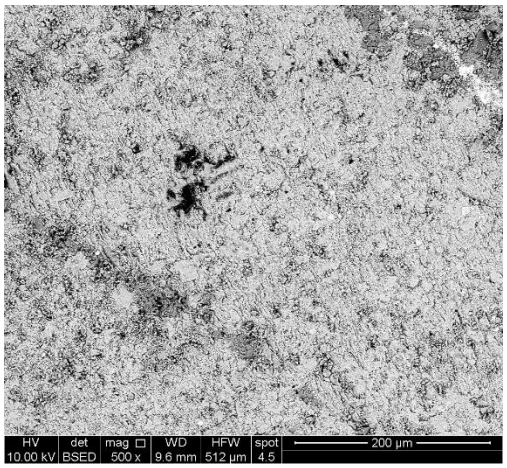

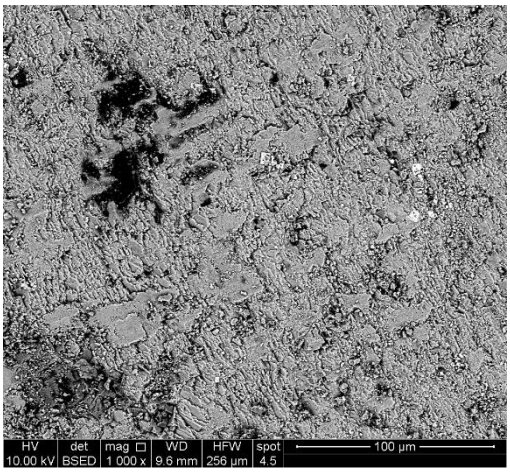

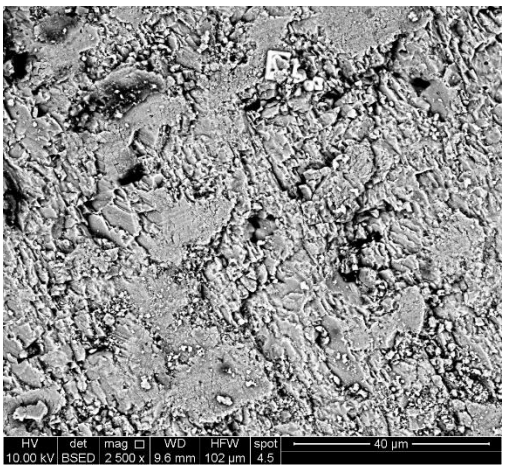

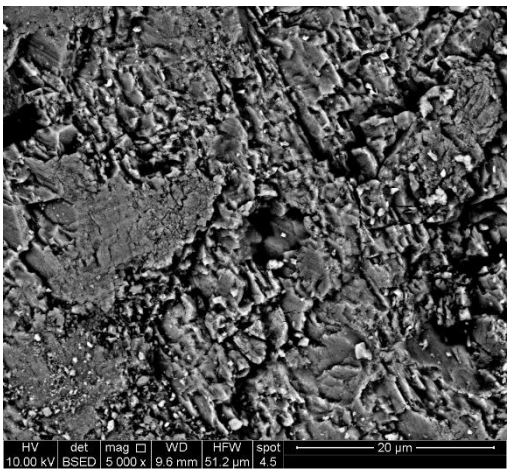

Site 3 SEM – BSED Images, Wet-Exposed 100x-5000x

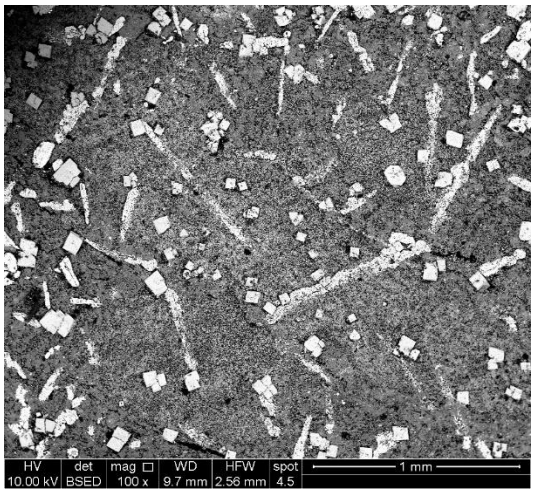

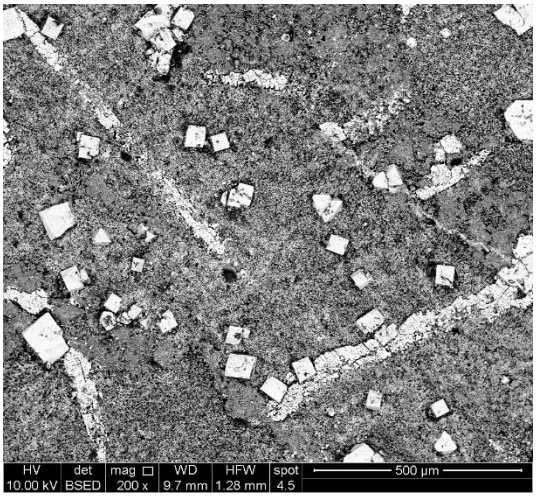

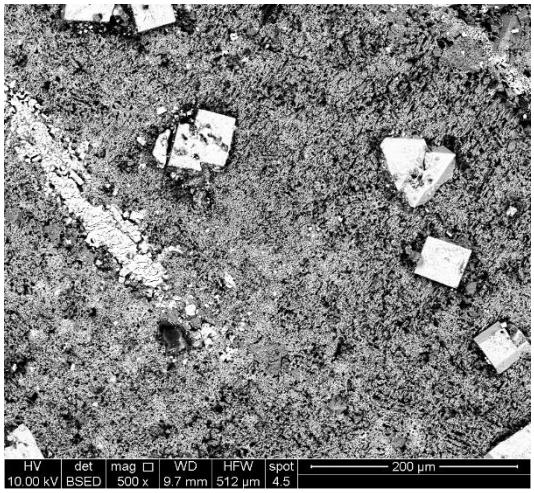

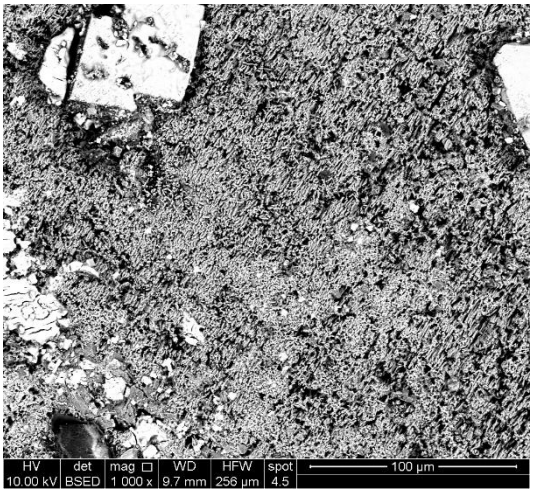

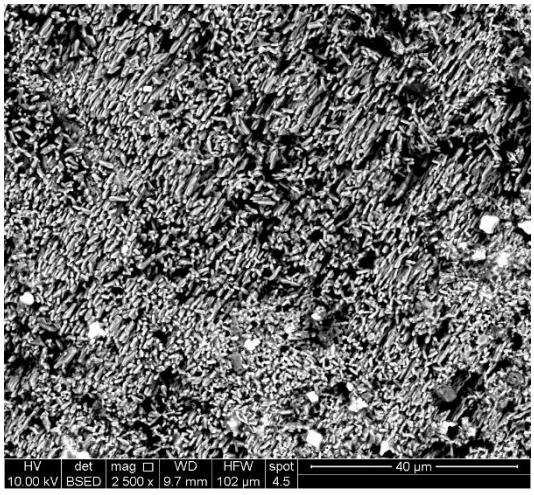

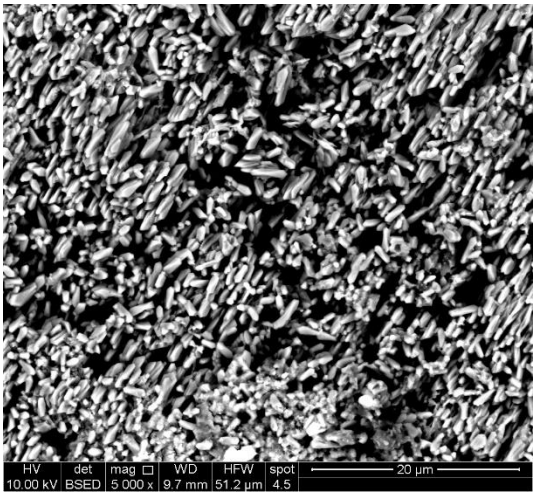

Site 4 SEM – BSED Images, Non-Exposed 100x-5000x

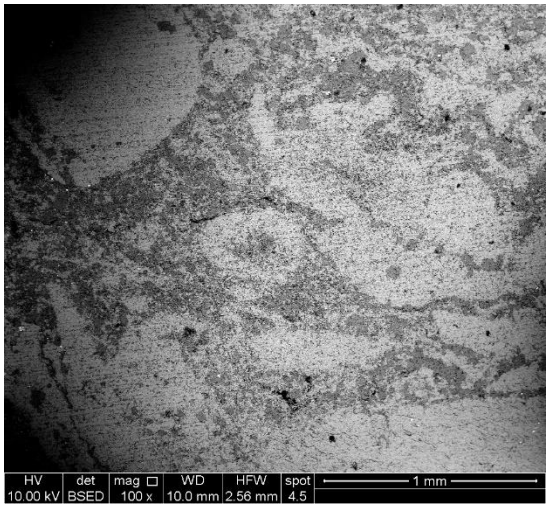

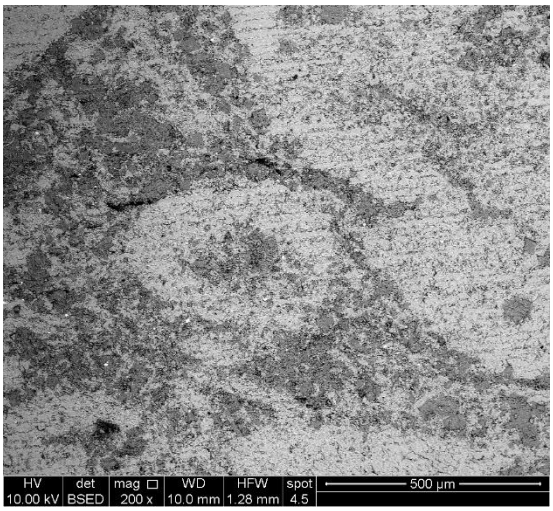

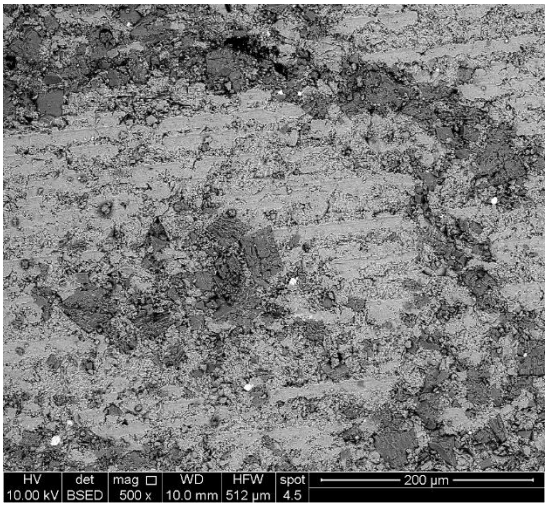

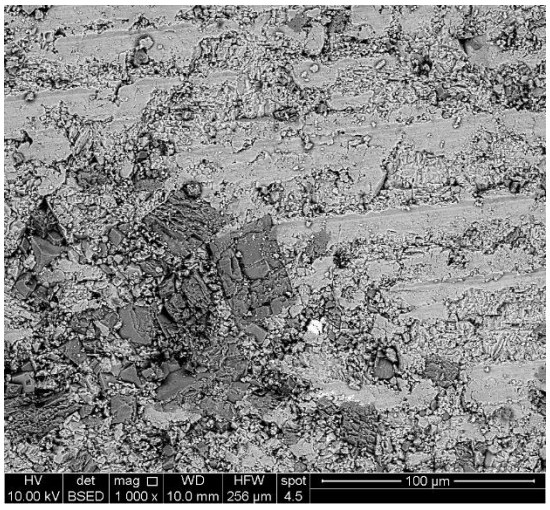

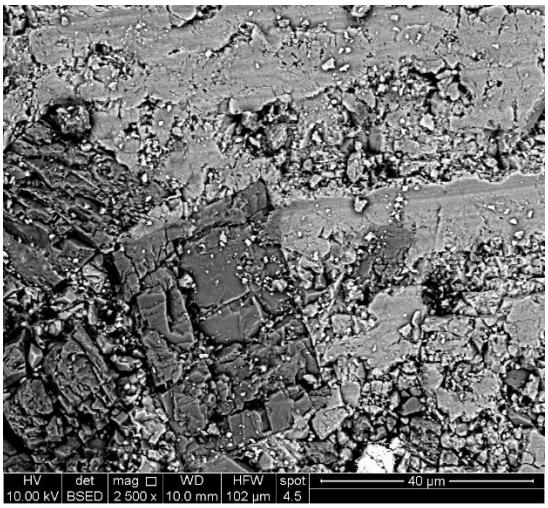

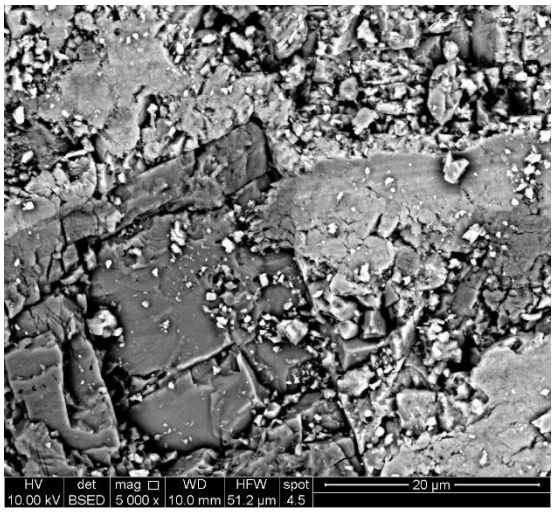

Site 4 SEM – BSED Images, Dry-Exposed 100x-5000x

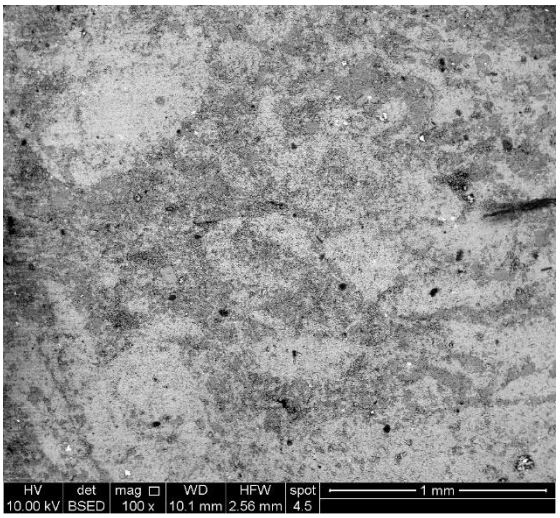

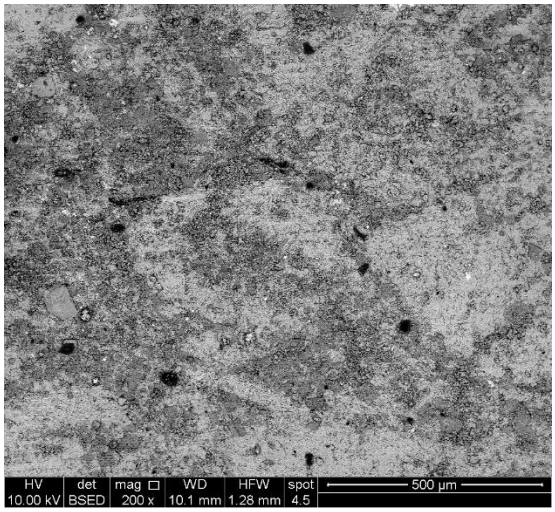

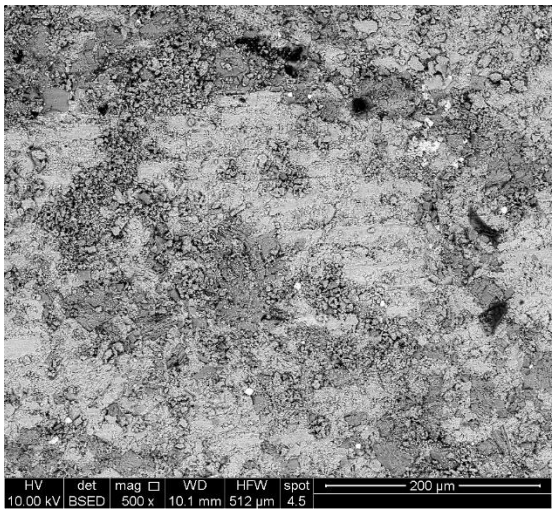

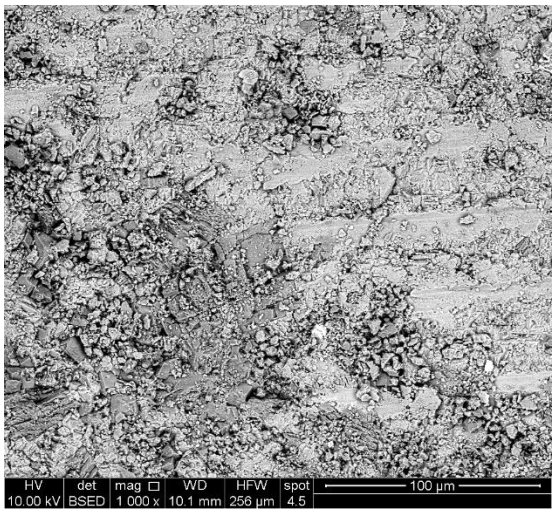

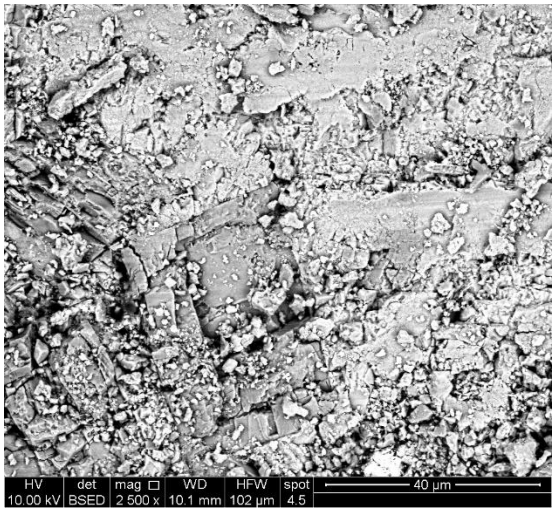

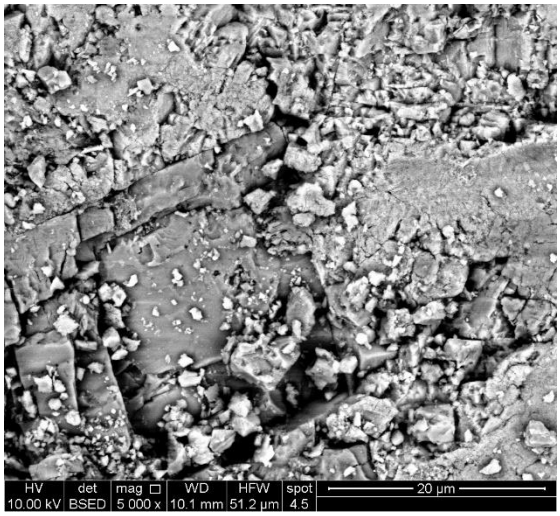

Site 4 SEM – BSED Images, Wet-Exposed 100x-5000x

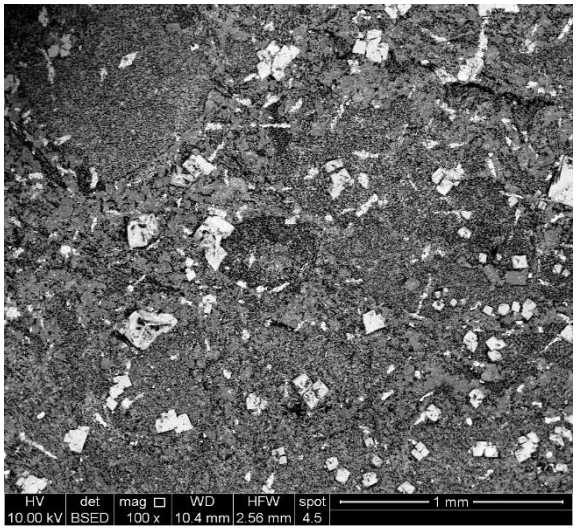

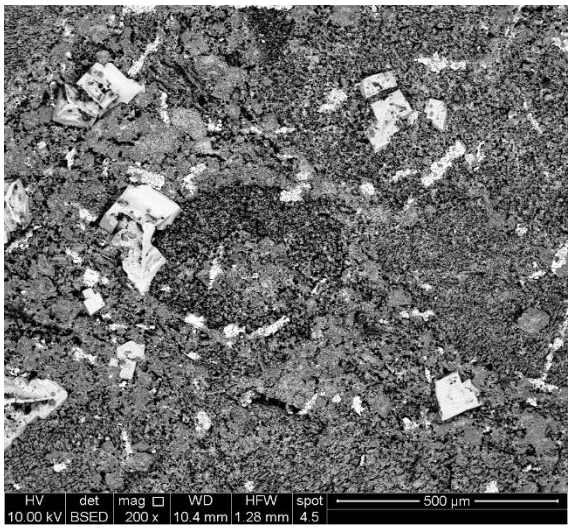

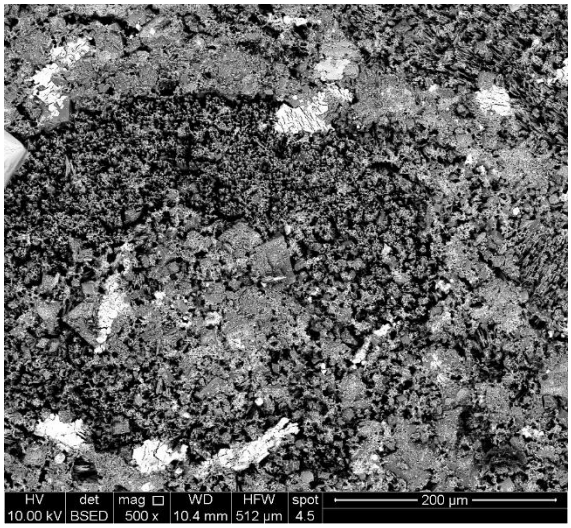

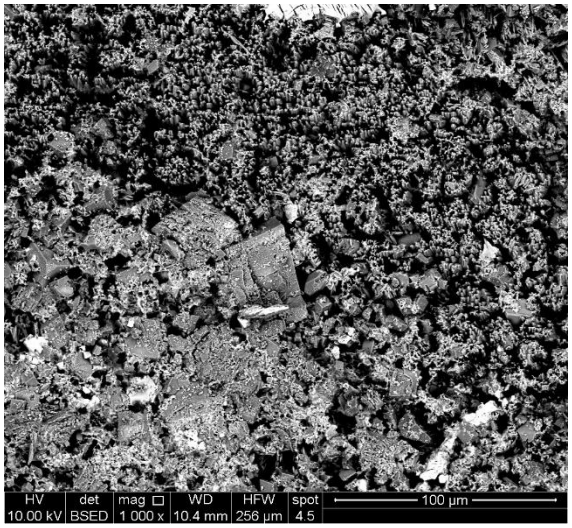

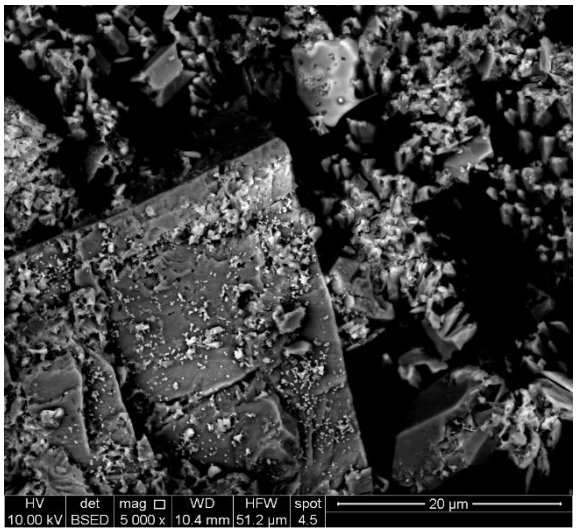

Site 5 SEM – BSED Images, Non-Exposed 100x-5000x

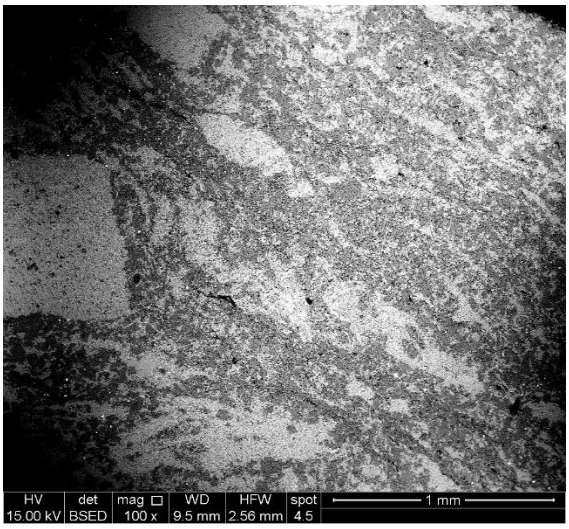

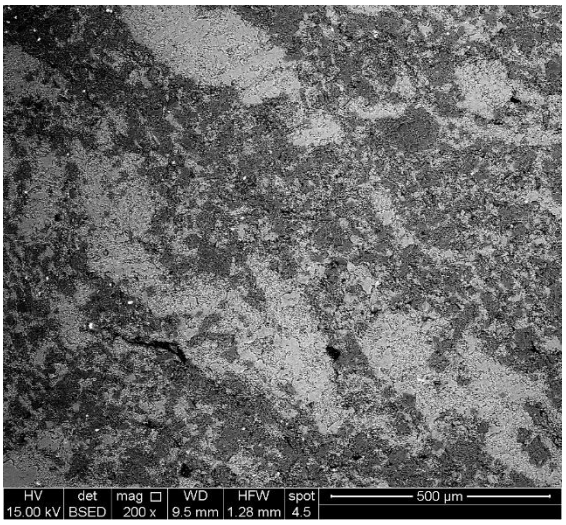

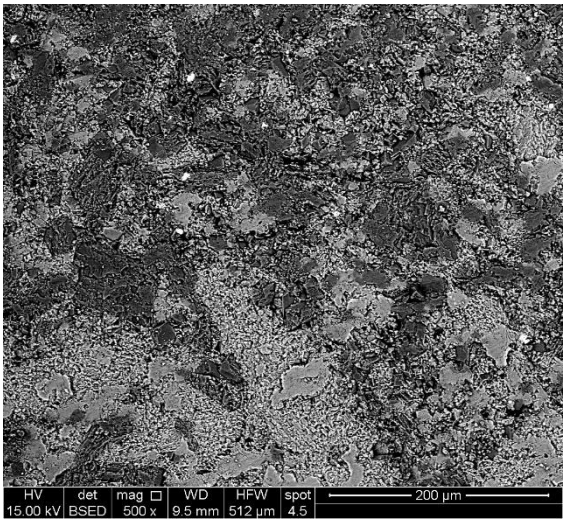

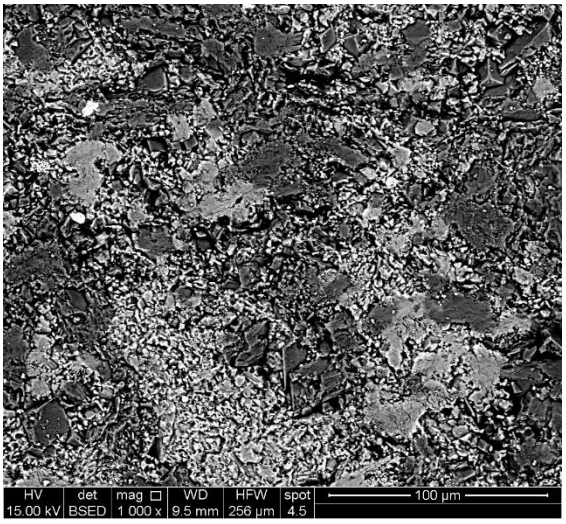

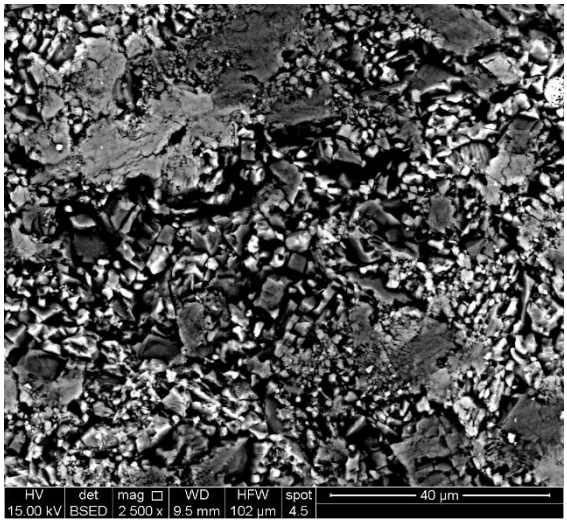

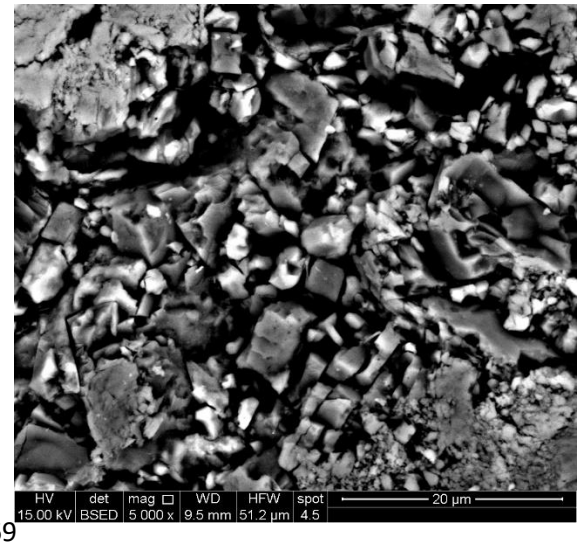

Site 5 SEM – BSED Images, Dry-Exposed 100x-5000x

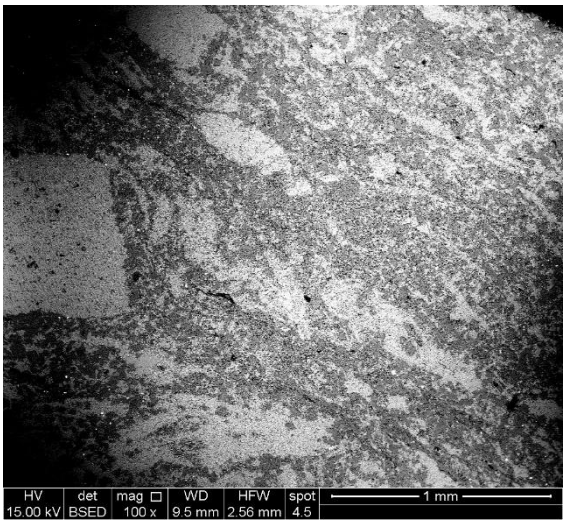

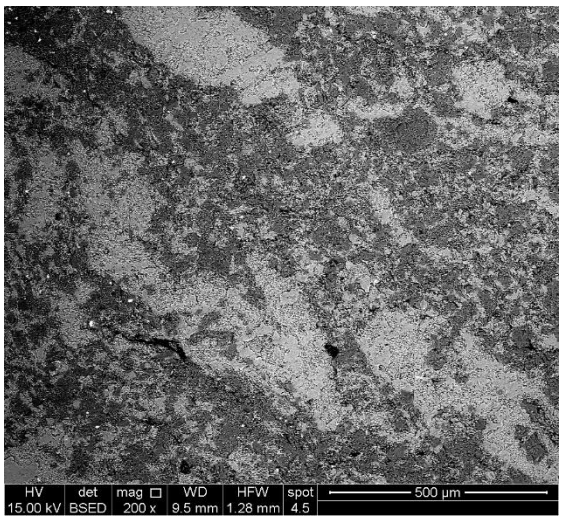

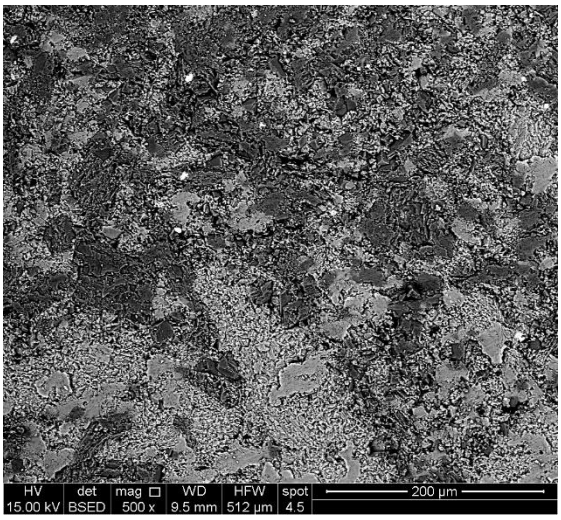

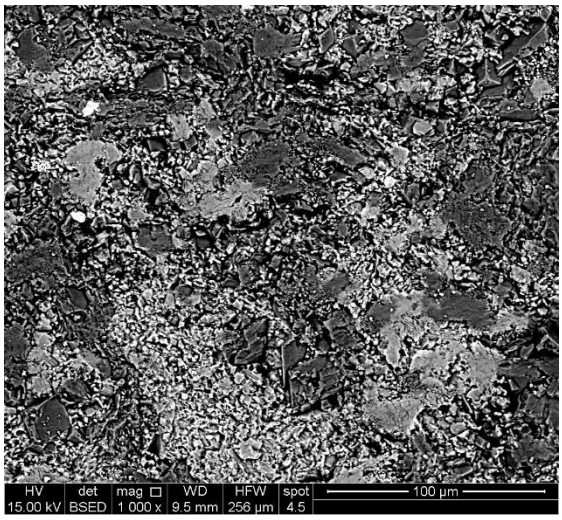

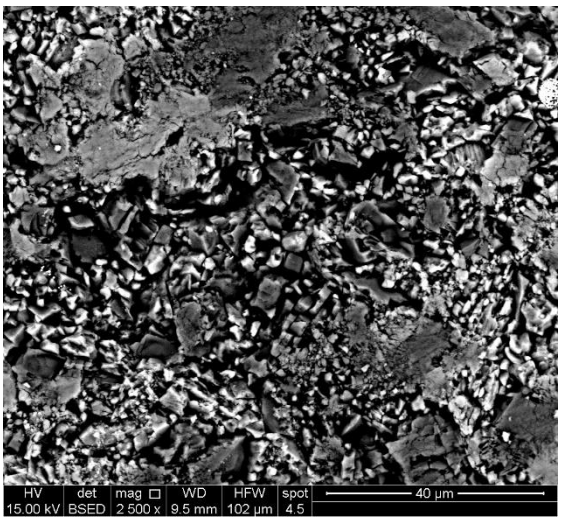

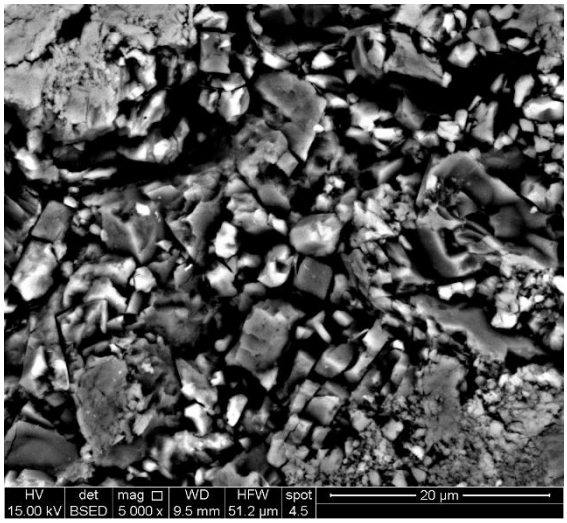

Site 5 SEM – BSED Images, Wet-Exposed 100x-5000x

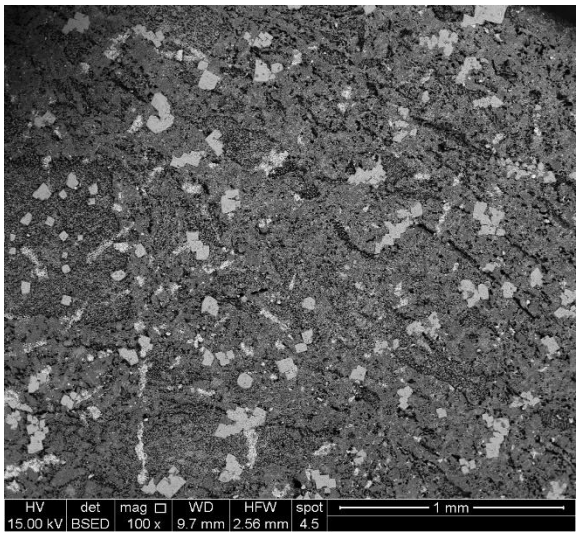

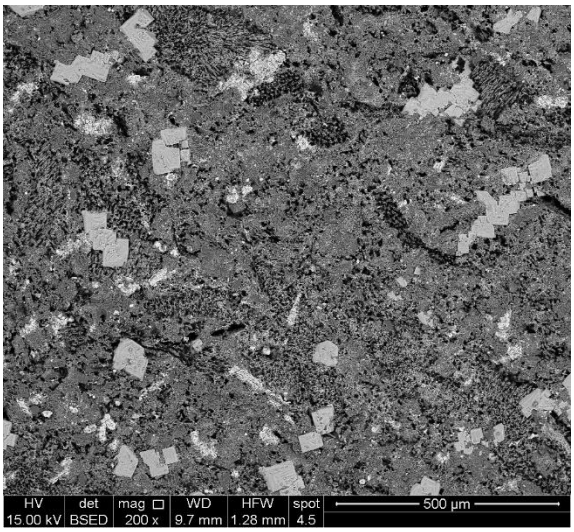

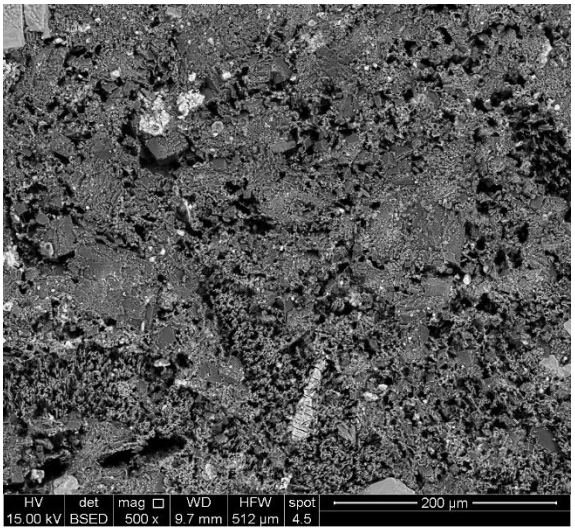

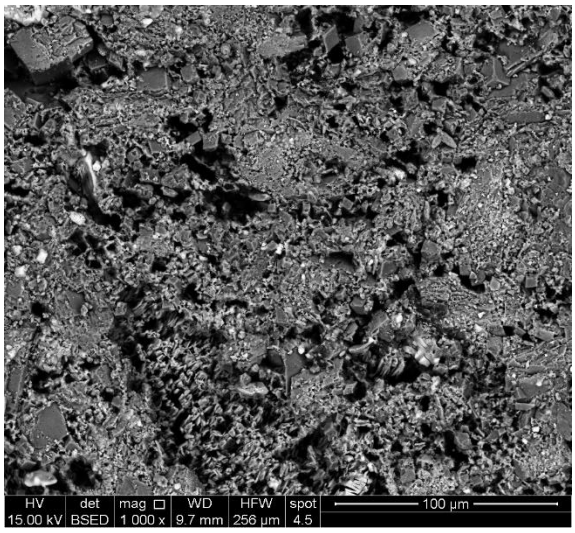

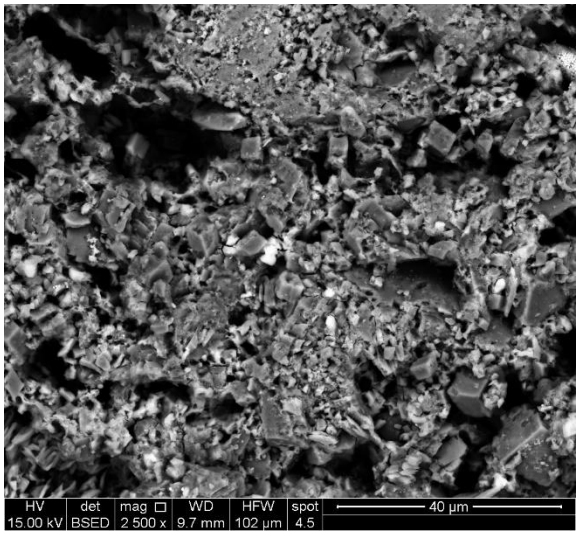

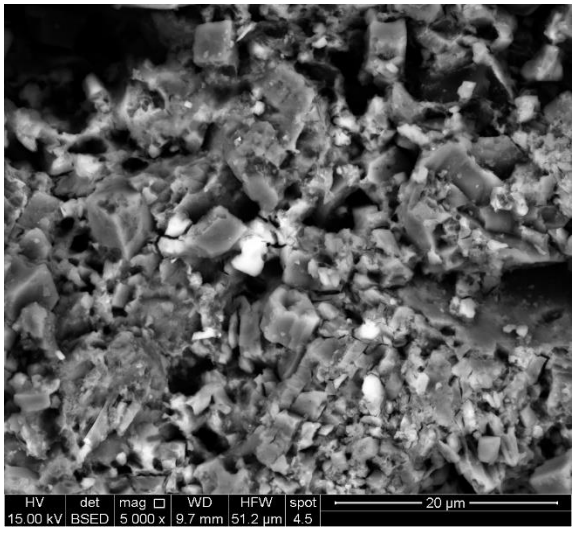

APPENDIX C

Binary Images vs. SEM – BSED Images, Site 1 and Site 4, and Site 5, 200x magnification

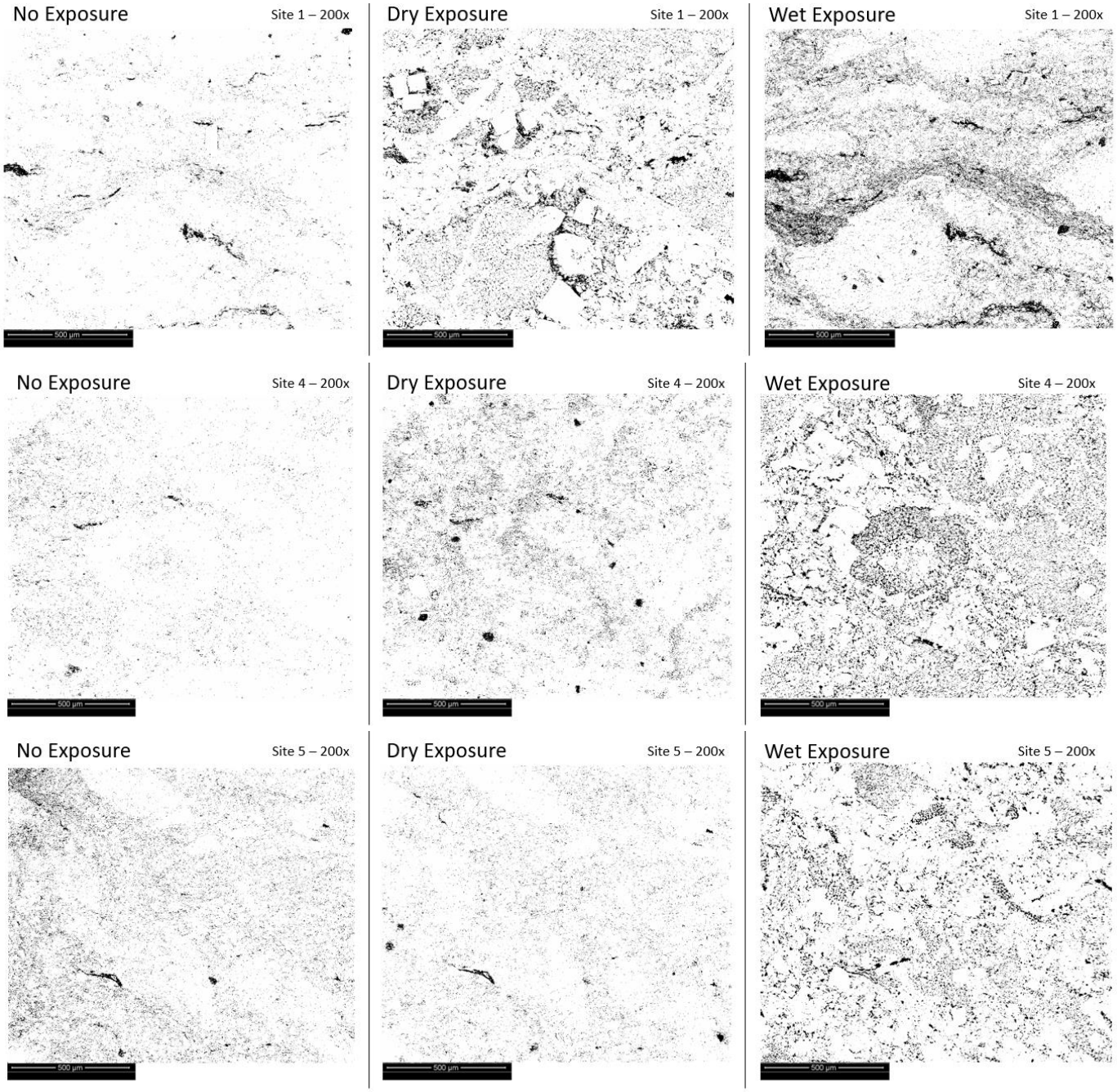

Binary Images vs. SEM – BSED Images, Site 4, and Site 5, 5000x magnification

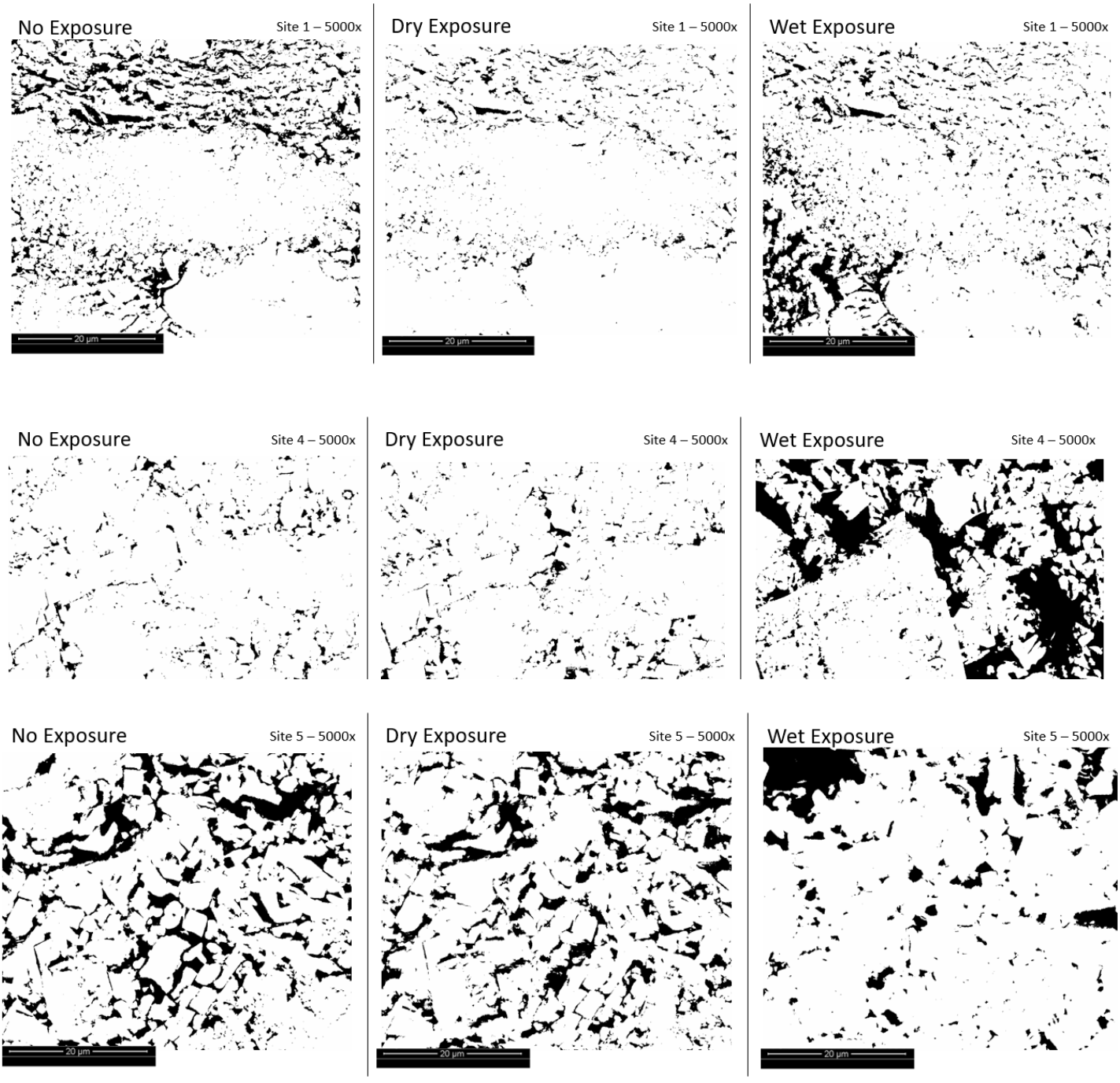

VITA

Mary Kathryn Tkach

Candidate for the Degree of

Master of Science

Thesis: CARBONATE CAPROCK SEALING CAPABILITIES: CCUS APPLICATIONS IN THE MICHIGAN BASIN

Major Field: Geology

Biographical:

Education:

Completed the requirements for the Master of Science in Geology at Oklahoma State University, Stillwater, Oklahoma in December, 2020.

Completed the requirements for the Bachelor of Science in Geology at University of Pittsburgh, Pittsburgh, Pennsylvania in 2016.

Experience:

T3 Global Strategies, Bridgeville, PA 2020
Geospatial and CAD Technician

National Energy Technology Laboratory, South Park, PA 2014-2018
Mickey Leland Energy Fellow
ORISE Research Fellow

Professional Memberships:

American Association of Petroleum Geologists
Society of Petroleum Engineers
Pittsburgh Geological Society
Tulsa Geological Society
Girl Scouts of the United States of America